High-Index Contrast Silicon Rich Silicon Nitride Optical Waveguides and Devices

Philipp, Hugh Taylor

Publication date:
2004

Document Version
Publisher's PDF, also known as Version of record

High-Index Contrast Silicon Rich Silicon Nitride Optical Waveguides and Devices

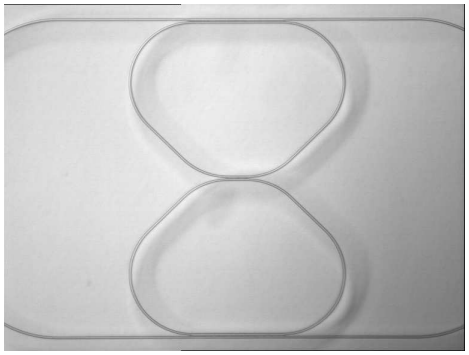

Hugh T. Philipp

Ph.D. Thesis. July 2004
Research Center COM
Technical University of Denmark

High-Index Contrast Silicon Rich Silicon Nitride Optical Waveguides and Devices

Ph.D Thesis

Hugh T. Philipp

July 2004

Research Center COM
Technical University of Denmark

Supervisors: Karsten Rottwitt, Professor, ILC Group Leader
Jørn H. Povlsen, Associate Professor

Acknowledgments

I have greatly enjoyed my time in Denmark at the Technical University of Denmark (DTU) and the chance to work with such a technically gifted group of people. I believe it has contributed greatly to my personal and intellectual growth. I hope I will be able to continue the professional and personal relationships I have established here.

The first person I would like to acknowledge is my wife Christine. Without her kind understanding and patience, I would not be here. When I suggested that I quit my job at Goddard Space Flight Center and that we pack up our things and move to Denmark, she agreed. For this I must thank her.

The second person I would like to thank, is the person who invited me to COM in the first place and was my initial adviser, Jörg Hübner. He has been a valuable technical resource, and fair minded friend to me. I only regret that circumstances dictated that we did not work more closely throughout my Ph.D.

I would also like to thank Winnie Svendsen for picking up the role as my Ph.D. adviser when Jörg left to pursue opportunities in California. She contributed greatly to refining and channeling my energies into productive activities.

My present adviser, Karsten Rottwitt, deserves significant credit and thanks for his continued support of my project and ability to listen to my conjectures without balking. He has provided me not only with resources to continue my work, but has opened up new avenues to pursue and I think my work would have greatly suffered without his enthusiasm and council.

It is impossible to make a comprehensive list of people that deserve thanks, so I beg anyone I exclude not to take offense. A non-comprehensive list of people deserving thanks includes: Karin Andersen, whose processing work and materials research have made my project possible; Peter C. Nielsen, who worked with Karin on the initial material development of silicon rich silicon nitride at COM; Haiyan Ou, who has been a good friend, an honorable colleague and a valuable resource of cleanroom know-how; Mikael Svalgaard, whose expertise in UV-writing and eye for detail has been greatly appreciated; Christian Mikkelsen, who generally raises the level of any technical discussion; Hans-Jurgen Deryll whose grating expertise has brought recent successes; Kjartan Færch, whose technical expertise and humor has been highly beneficial; and Anders Bjarklev, for understanding and level-headed leadership.

I would also like to thank my parents, my brother, Roland Gouel, Dino Jardina, A. Erik Vogt, J. Gordon Arbuckle, and Bruce Hamilton for various formative influences, inspirations and friendships.

Publication List

Journal Papers

H.T. Philipp, K.N. Andersen, W. Svendsen, and H. Ou. *Amorphous silicon rich silicon nitride waveguides for high-density integrated optics.* Electronics Letters, vol. 40, issue 7, pp. 419- 421 (2004).

H.T. Philipp, K.N. Andersen, W. Svendsen, and M. Svalgaard. *High-density high-index contrast integrated optics: Developments and applications at COM.* DOPS-Nyt-1 (2004).

H.T. Philipp, W. Svendsen, K.N. Andersen, J. Hübner and J. Hedegaard Povlsen. *Measurement of optical nonlinearity in silicon rich nitride waveguide ring resonators.* Electronics Letters, vol. 39, issue 16, pp. 1184-1185 (2003).

Conference Contributions

H.T. Philipp, K.N. Andersen, W. Svendsen, and H. Ou. *Low-loss silicon rich silicon nitride waveguides for high-density integrated optics.* IPR, paper JWB28, San Francisco, CA (2004).

K.N. Andersen, W.E. Svendsen, R.K. Sandberg, H.T. Philipp and J. Hübner. *Silicon rich nitride micro-resonators.* ECIO, paper A2.2, Prague, Czech Republic (2003).

W.E. Svendsen, H.T. Philipp, M. Svalgaard, H. Mertens and K.N. Andersen. *High index ring resonator coupled to UV-written waveguide.* ECOC 2002, paper 4.2.4, Copenhagen, Denmark (2002).

Contents

Chapter 1

Introduction

The idea of using dielectric waveguides for the processing of optical signals in integrated circuits is not new. Serious technical discussion of integrated optical circuits has been around since the 1960's, and perhaps earlier. Several landmark articles were published in the Bell System Technical Journal by Miller and Marcatilli in 1969 [1–3]. They included some important fundamentals – estimates on bending loss, directional couplers, and mention of ring resonators. These are the building blocks of integrated optics and in fact are applicable to other waveguiding systems – for instance, in the microwave region where the use of similar devices predates their use in integrated optics. The potential of integrated optics, however, has not been fully realized. The field experienced growth and increased research interest with the "communications bubble" of the late 1990's, but there is no standard platform and it is unclear what technologies, if any, will ultimately dominate. Planar germanium doped waveguides, using materials similar to those used to make optical fibers, represent one of the most popular integrated optical platforms [4], but they generally do not have properties which are conducive to a high level of integration. There are also relatively new ideas and technologies that take advantage of non-conventional light guiding methods, such as photonic bandgap based devices, that have received a lot of attention, but have yet to prove themselves commercially viable for integrated circuits.

The goal often cited by advocates of integrated optical devices is in-

creasing the amount of processing done in the optical regime. This is desirable because the transition to the electronic regime costs time [5], and though electronic detectors and emitters are constantly making impressive progress, it is thought that they will reach a fundamental frequency response limit that might be best addressed by switching to the optical regime [6]. Complex optical processing generally requires a wide variety of flexible filtering functions that can be efficiently packed in a small area. These needs are not well addressed by "standard" germanium doped waveguides because a large bending radius ($\approx 2\,mm - 1\,cm$ depending on the refractive index [1] contrast) is required [7] to maintain low loss. As a result, the devices tend to be fairly large for an integrated technology. More than this, many devices that can be implemented can also be made with fibers. Fibers have the additional advantages of low propagation loss; low insertion loss when coupled to other fibers; and low birefringence. Fibers have also proved to be an effective medium for UV-written gratings [8], which allows for the construction of complex filters, and erbium doped fiber lasers [9]. Integrated optics must offer something more, such as a high level of integration and more complex functionality.

The reason for the large size of integrated optical devices is not a fundamental limitation of optical waveguide technology. It is because the first integrated optical platforms were modeled after standard optical fiber, and this means that they adopted properties that were developed for the efficient transmission of signal over long distances and not for high-density optical processing. Several criteria were important in the development of standard fiber optic networks. A couple of them are:

1. Low loss. This has typically been reduced to about $0.2dB/km$ for standard optical fiber [10].

2. Low group velocity dispersion. This is required to keep the spreading of optical pulses over long transmission distances manageable [10].

Both of these criteria are addressed using relatively low-index contrast ($\Delta n \approx 0.01$) waveguides with weakly guided modes. The demands of integrated optics are, however, fundamentally different. Though loss

[1] The optical refractive index will be referred to as the "index".

is still a concern, requirements for loss of less than $1\,dB/km$ would be ludicrous since the length of integrated optical components tend to be on the order of centimeters (or less) [2]. The total insertion loss of a device should be manageable, but the size and function of the device should also be considered. Group velocity dispersion, should be manageable, but, again, the transmission distances of integrated optical circuits tend to be on the order of centimeters. This means that a much higher level of dispersion should be acceptable for integrated optical circuits, and this is particularly true if dispersion compensating filters can be monolithically incorporated.

So, some technical demands that led to choosing a low-index contrast platform are significantly relaxed for integrated optical devices. Other demands have, however, become more critical. For a smaller bending radius, and thus a higher packing density, the immediate solution is an increase of index contrast, though it must be noted that other approaches such as trenches utilizing total internal reflection have also been proposed [11,12]. An extreme increase in index contrast can be used to make photonic bandgap structures, or more morphologically classical planar waveguide devices with a high-index rectangular core and smooth sidewalls. The general concept can be applied to a number of different platforms, including, but not limited to, semiconductors, polymers and different types of glass [4].

In addition to increasing the packing density of photonic devices, there is another fundamental reason sharper bends are desirable when making integrated optical devices. Ring resonators, which can be viewed as a fundamental optical filtering component [13], can be made much more useful, flexible, and applicable to modern optical processing demands when the radius of curvature is decreased. The reason for this is that the free spectral range (the distance between adjacent resonances) is inversely proportional to the distance around the ring. Ring resonators are technically attractive devices because they can be compact; they are ideally non-reflective; and they provide channel selecting and dispersion compensating filter functions [13].

[2] The propagation losses for germanium doped planar silica waveguides are, in fact, significantly higher than optical fiber because of processing differences.

The solution for making high-density integrated optics would seem simple. Increase the index contrast and higher integration is possible, but there are details that make this difficult. The size of the core necessary for single mode operation is much smaller. This leads to tighter manufacturing tolerances. Many of these tolerances don't simply scale with core size because waveguide properties become more sensitive to geometric variations of the waveguide cross-sections. A typical waveguide requires that the effective index[3] of the propagating mode be between the refractive index of the core and the refractive index of the cladding. This means that without consideration of waveguide dimensions, a high-index contrast waveguide can have a wider range effective indexes than a low-index contrast waveguide simply by virtue of the materials (and their refractive indexes) used to define the waveguide. The particular, discrete, effective index associated with a guided mode is determined by the geometry of the waveguide. The variations of the effective index of a guided mode as a function of perturbations to waveguide geometry are therefore directly related to the index contrast.

Loss in high-index contrast waveguides is also greater for a given sidewall roughness (increasing with the cube of the index contrast [14]), and the efficiency of coupling to standard optical fiber is a problem because of modal mismatch between the fundamental guided modes.

This thesis concentrates on high-index contrast waveguides made with an amorphous silicon rich silicon nitride (an amorphous form of silicon nitride with a high proportion of silicon) core material and silica cladding. The fabrication techniques closely follow those used to make silica on silicon waveguides that use germanium doping to define (by increasing the refractive index) the core region. This fabrication technique was chosen because of its availability at COM and the belief that a glass based platform offered opportunities to improve the coupling of standard optical fiber to high-index contrast devices.

The chapters of the thesis follow a compartmentalized view of the

[3] the effective index is defined for a guided mode propagating in the z-direction as $n_{eff} = \beta\lambda/2\pi$ where β is the propagation constant of the mode given in the general expression for the electromagnetic field components $f(x, y, x, t) = A(x, y)exp(i\omega t - i\beta z)$. λ is the wavelength of the light in a vacuum.

research, but it should be noted that some of the delineations are artificial. Chapter two starts with a summary of the material properties and fabrication techniques. This is a wide and interesting field, and there has been lots of work done on the material development at COM - some of it predating my arrival. It is an essential consideration that determines the limits of the technology because it ultimately decides what subset of the theoretically possible devices are actually realizable at any given time.

The third chapter addresses high-index contrast waveguiding. Much of the chapter deals with explaining the expected properties of high-index waveguides. If I were coming to the Research Center COM today to continue this research, this chapter would provide essential information about the magnitude of effects related to polarization and dispersion. The later parts of this chapter deal with some experimental results such as propagation loss and curvature loss. These will offer a view of the current limits of the devices made. One of the more interesting results is related to low coupling loss to optical fiber when a certain waveguide geometry is used.

The fourth chapter covers ring resonators and optical filters. Being one of the major advantages of a high-index platform, ring resonators are given a lot of focus. The basic model of the ring resonator is presented. The way it is presented follows my understanding and addresses specifics I believe are helpful for a continued research effort. The chapter continues with some useful alternate formulations on ring resonators like the coupling of modes in time - following B.E. Little's formulation [15]. Then experimental results are presented with emphasis on those that I believe are indicative of the potential of this platform - including ring resonators, add-drop filters and a double-ring filter.

The fifth chapter covers some results obtained using a photosensitive germanium doped-layer used in combination with high-index contrast waveguides. The full potential of this has yet to be realized, but at least two interesting possibilities were explored. The first is the fabrication of monolithic hybrid devices using both high-index contrast waveguides and directly UV-written waveguides. This utilizes some special capabilities developed at COM for direct UV writing and is an attempt to reduce losses experienced when coupling to standard optical fiber. The second

is UV writing gratings for high-index contrast waveguides using a phase mask.

The sixth chapter covers some work on non-linearities. The emphasis is on a set of measurements taken to measure the D.C. Kerr effect [16] in high-index waveguides by tracking resonance shifts of ring resonators as a function of an applied electric field. This is a particularly useful and interesting part of the research because the high confinement of the optical mode in high-index contrast waveguides leads to stronger electric fields for a given signal power when compared to fiber. Strong electric fields allow nonlinear properties to be more readily exploited to make active optical devices. One example of this is an optically bistable ring resonator that, in addition to the high confinement of high-index contrast waveguides, can use a high quality (Q) factor to increase the power density.

The seventh chapter is a conclusion. It represents a conclusion to my Ph.D. studies, but I don't think it is a definitive conclusion of the work because there are many more avenues to explore. As such, there is indication of research I believe is a natural progression of the work already done.

Chapter 2

Silicon Rich Silicon Nitride

In this thesis amorphous silicon rich silicon nitride (Si_xN_y) films, also referred to as silicon rich nitride (SRN), are used to make optical waveguides. This chapter will review some properties of these films, concentrating specifically on optical properties that are important for waveguiding. A basic outline of the device fabrication process will be presented, as well as some important measurements made on the material.

2.1 Integrated Optical Materials

Before proceeding, it should be noted that there have been many material systems and processing techniques proposed for the fabrication of integrated optical devices. Materials proposed include, but are not limited to, silica on silicon [7], silicon on insulator (SOI) [17, 18], lithium niobate [19], indium phosphide [20], silicon oxynitride [21], and various polymers [4,22]. The processing techniques for making waveguides, which requires making structures with different indexes of refraction, include ion exchange [23], cleanroom fabrication, proton bombardment [24], and UV irradiation [25]. Some of these material systems and processing techniques have specific advantages such as high nonlinearities (e.g. lithium niobate and some polymers), or well defined processing techniques (e.g. silicon on insulator).

Amorphous silicon rich nitride was chosen for the waveguiding medium

in this research because it could be fabricated using a platform similar to standard silica on silicon optical waveguides; after proper preparation it displays low optical loss in the communications band around $1550\,nm$; it provides a large refractive index contrast with silica; and it offers the possibility of easy integration with different types of waveguides (e.g. clean room fabricated germanium doped silica waveguides or directly UV-written waveguides, which will be shown in chapter 5).

2.2 Materials

2.2.1 Deposition

All devices made used a 4 inch diameter silicon wafer for a substrate. Since the refractive index of silicon in the communications bands is greater than that of the materials conventionally used for making waveguides, a thermal oxide layer was grown on the wafer to provide a buffer/lower-cladding material for optical waveguides. This is a standard procedure when fabricating silica on silicon waveguides. The thickness of the thermal oxide layer was typically between $10\,\mu m$ and $12\,\mu m$. This thickness is more than adequate to prevent significant signal loss to the silicon substrate ,via substrate leakage, for the well confined guided modes of high-index contrast waveguides [26].

Silicon rich silicon nitride was deposited on the thermal oxide using low pressure chemical vapor deposition (LPCVD). The chemical species used for the formation of the film were dichlorosilane ($SiCl_2H_2$) and ammonia (NH_3). The flow rates of these gases can be controlled to affect the stoichiometry of the film, which has a direct influence on the film's refractive index and the stress. A typical ratio for the gas flows was $3.2 : 1$ (dichlorosilane(sccm):ammonia(sccm)). The deposition rates of the film were approximately $5nm/min$ and the total deposition time for a $0.6\,\mu m$ film was about 2 hours not accounting for time associated with temperature ramping.

After depositing the film, the samples were annealed at $1100°C$ to reduce stress and the number of $N-H$ bonds in the film. The presence of $N-H$ bonds in a film can have deleterious effects on optical

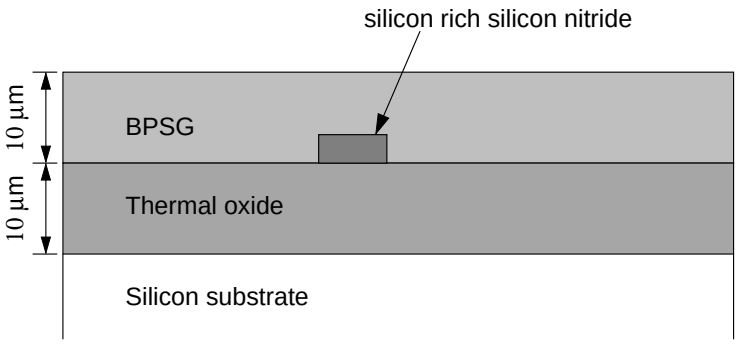

Figure 2.1: Typical cross-sectional configuration of a silicon rich silicon nitride waveguide.

components because the primary absorption of the $N-H$ bonds has a wavelength of $3000\,nm$ and an overtone occurs around $1500\,nm$. The precise location of this harmonic may vary according to molecular structure [26]. Temperatures typically used to break $N-H$ bonds exceed $1100°C$, but crystallization centers have been observed in the silicon rich silicon nitride films that have been annealed above $1100°C$. Random crystallization centers can cause local fluctuations of the refractive index that lead to the scattering of propagating optical modes and are therefore undesirable for optical films. As a result, the films are typically annealed for a longer period of time (4 hours) while maintaining the temperature at $1100°C$ [27] or below. This solution seems to have the desired effect (see section later in this chapter) of reducing optical signal loss associated with $N-H$ bonds. This is briefly reviewed in section 2.4.

The stresses of these films were measured by observing deformation of wafers after processing for films deposited directly on the silicon substrate and applying Stoney's equation [27]. These stresses varied between $50\,MPa$ (tensile) and $250\,MPa$ (compressive). Stresses that are lower than or equal to $10\,MPa$ have been measured in deposited silicon rich silicon nitride films [27].

Films with a thickness of $\approx 0.5\,\mu m$ have been measured to have a thickness uniformity of less than $6.9\,\%$ for a batch of 12 wafers and $1.7\,\%$

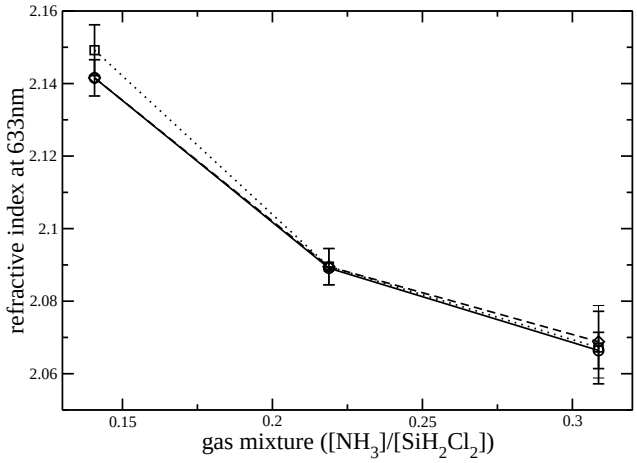

Figure 2.2: The refractive index of LPCVD deposited silicon rich silicon nitride films as a function gas mixture $[NH_3](sccm)/[SiH_2Cl_2](sccm)$. The measurements of the refractive index were performed with a prism coupler after annealing [29].

for a single wafer with a tendency to have a slightly thicker film toward the edge of the wafer. The optical refractive index of the film was measured to vary between 2.06 and 2.16 at $633\,nm$ (see figure 2.2). A much wider range than this has been observed elsewhere [28] with more extreme changes in stoichiometry. The uniformity of the film's refractive index was measured to be $\approx 0.3\,\%$ for a film with a nominal refractive index of 2.09 at $633\,nm$ (this translates to a refractive index of 2.06 at $1500nm$) [27].

LPCVD is available for the deposition of thin films (up to $\approx 1.5\,\mu m$ of silicon rich silicon nitride may be deposited) and has several advantages over other deposition technologies such as plasma enhanced chemical vapor deposition (PECVD). First, it is a batch process. In the ovens at COM, there can be well over 15 wafers deposited at once with good uniformity. Secondly, the films show low stress after deposition when compared with PECVD deposited films.

2.3 Waveguide Fabrication

Waveguide-based structures were designed for a high-index contrast waveguides. Layout files were generated from the designs. With the layout file and tolerance specifications, a mask was ordered from and manufactured by CompuGraphics [1]. Contact UV lithography was used to transfer the waveguide structures to a photo-resist film. The photo-resist film used was AZ5214E (Shipley), the approximate thickness of this film was $1.5\,\mu m$.

Reactive ion etching (RIE) was used to etch the waveguides into the silicon rich silicon nitride film. A layer of borophosphosilicate glass (BPSG) was deposited as a top cladding. This layer is designed to flow easily during annealing to ensure good, uniform coverage of waveguides. The mixture of phosphorus and boron was adjusted to match the refractive index of the deposited and annealed film to that of the thermal oxide (SiO_2) layer. Good control over the sidewall angle was observed, with some sidewalls having an angle of 89° (i.e. nearly perpendicular to the substrate). The angles of the sidewalls were observed with a scanning electron microscope (SEM) immediately after etching, with no top cladding [29].

2.3.1 Linewidth Reduction

A waveguide is defined on a photolithographic mask with a certain width. After processing the actual waveguide has a width that is typically less than the structure on the photolithographic mask. The difference between the widths of the waveguide as defined on the mask and the actual waveguide width is the linewidth reduction. It is an idealized number that assumes a rectangular waveguide cross-section, but since there is good control of the sidewall angle, it is considered here to be a adequate indicator of processing performance.

The linewidth reduction of different samples of silicon rich silicon nitride waveguides has been measured to be between $0.2\,\mu m$ and $0.7\,\mu m$.

[1] *Compugraphics International Ltd.*, Glenrothes, Fife,KY7 4NT, Scotland

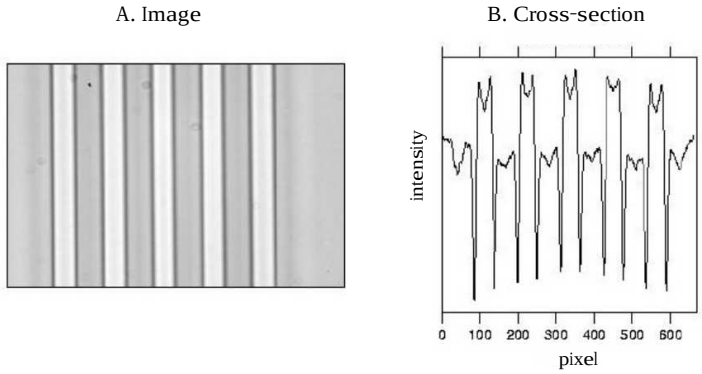

Figure 2.3: A: image of a $8\,\mu m$ period test structure. B: cross-section of he image used to determine scaling and linewidth reduction.

The wide range of linewidth reductions reflects the sensitivity of the processing. The best linewidth reductions were between $0.2\,\mu m$ and $0.3\,\mu m$.

The linewidth reduction was measured with two basic techniques. The first techniques used a scanning electron microscope (SEM) to image waveguide cross-sections immediately after etching. Samples measured were not processed further and the measurements reflected linewidth reductions that were typical for a batch of wafers. The second technique for the measurement of the linewidth reduction used optical microscopy of test structures after the fabrication of the device was complete. With this technique, test structures that have a known periodicity were imaged under an optical microscope to calibrate the scaling/magnification of captured images (i.e. the size of the pixel at a certain magnification). After calibration, the widths of waveguides were measured and compared to the width of the waveguides designated on the photolithographic mask. Though this technique is conceptually simple, the definition of what optical signature corresponds to the waveguide width is tricky. Linewidth reduction measured with optical microscopy is therefore an imperfect indicator. It should, however, be noted that the results obtained generally

Figure 2.4: Test structures showing a varying gap (on mask) between waveguides. Labels of the gap width are given above the waveguides.

agreed with figure obtained from SEM pictures. A sample of test structure pictures is shown in figure 2.3, along with a cross-sectional slice.

Measurements of linewidth reduction are complicated by structures that are not isolated waveguides and a single number for the linewidth reduction may be misleading in certain cases. One of the the most important structures in integrated optics that may be non-uniformly affected and misrepresented by a quoting a single linewidth reduction figure is the directional coupler. Gaps between waveguides may suffer from a number of anomalies that lead to a closing of the gap or top cladding irregularities in the coupling region. Figure 2.4 shows a test structure fabricated to test the limits of processing and clearly shows a $0.4\mu m$ gap (as designed on the mask) between two relatively wide waveguides being a the limit of the processing with this wafer. The minimum possible gap is a convenient and useful figure, but can be misleading because waveguides of different widths can display different minimum gaps.

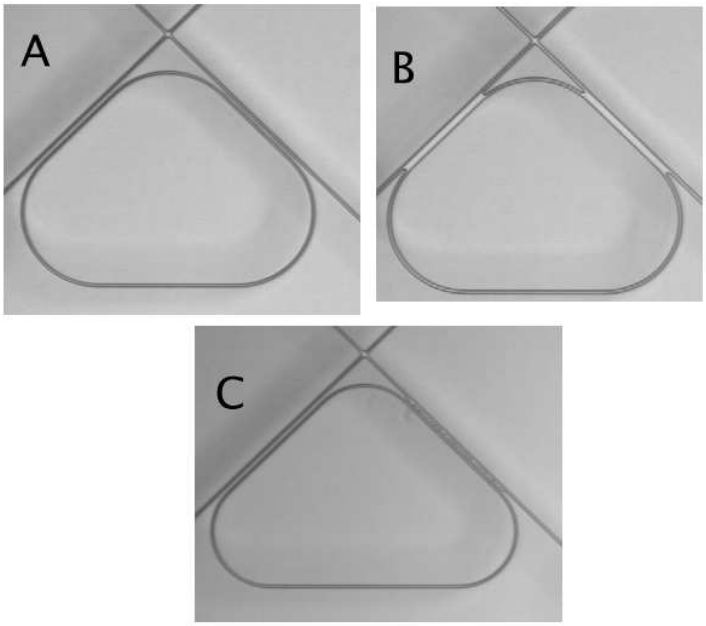

Figure 2.5: A: clean coupling region: $1\,\mu m$ wide waveguide with a $0.6\,\mu m$ (on mask) gap between the inner edges of the waveguides. B. merged coupling region: $1.2\,\mu m$ wide waveguides with a $0.4\,\mu m$ (on mask) gap between the inner edges of the waveguide. C. irregular coupling region (right hand side): $1\,\mu m$ wide waveguide with a $0.6\,\mu m$ (on mask) gap between the inner edges of the waveguides. The picture in C was taken from a different location on the same wafer as A.

Figure 2.5 show waveguides coupled to ring structures and some of the problems that can occur. The first image (A) in figure 2.5 shows two coupling regions of an optical resonator. Both coupling regions in this case show good separation between the waveguides. The second image (B) in figure 2.5 shows a situation in which the gaps of both couplers are completely closed. The waveguides have merged during processing. The third image (C) in figure 2.5 shows an optical resonator in which the couplers have been non-uniformly affected. One coupler structure, to the left, shows good separation between waveguides. The other coupler, to the right, has defects in the coupling region. This is a good indication of processing anisotropy since these couplers are close in proximity, and lie at a 90° angle with respect to one another.

As a practical matter, these limits were viewed as a design constraint. Variations in the linewidth reduction between different processing runs were dealt with by making several structures designed to yield similar devices assuming different linewidth reductions. This is not always simple because to exploit the benefits of high-index contrast structures, particularly large free spectral range ring resonators, the coupling lengths should be short. This generally requires sub-micron coupling gaps.

Anisotropy, such as shown in figure 2.5 (C), presents a particular problem for the fabrication of useful optical filters because the performance of devices often relies on the relationship between coupling ratios.

2.4 N-H Absorption

Optical attenuation is another important characteristic of optical waveguides and needs to be addressed in any material system used to make waveguides. There are several possible origins for attenuation, and as previously stated, $N-H$ bonds have a harmonic that can cause absorption in communications band around $1500\,nm$. Annealing the sample should reduce the number of $N-H$ bonds and thus the attenuation of optical signal. To test this hypothesis, the attenuation of a thin film of silicon rich silicon nitride was measured using a pair of prism couplers [30] shown in figure 2.6. Light was coupled into a guided slab mode of a silicon rich silicon nitride film using a prism. Another prism was used to

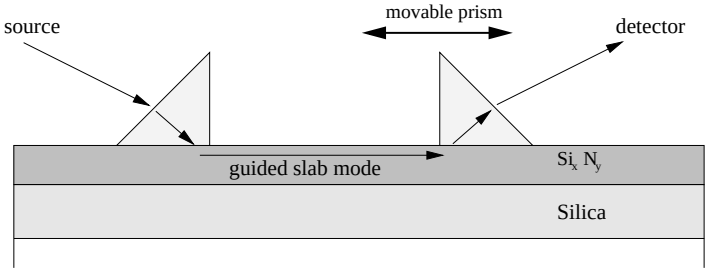

Figure 2.6: A diagram of the dual prism coupler set-up. The prism coupler to the right of the figure was translated across the surface of the wafer. [26]

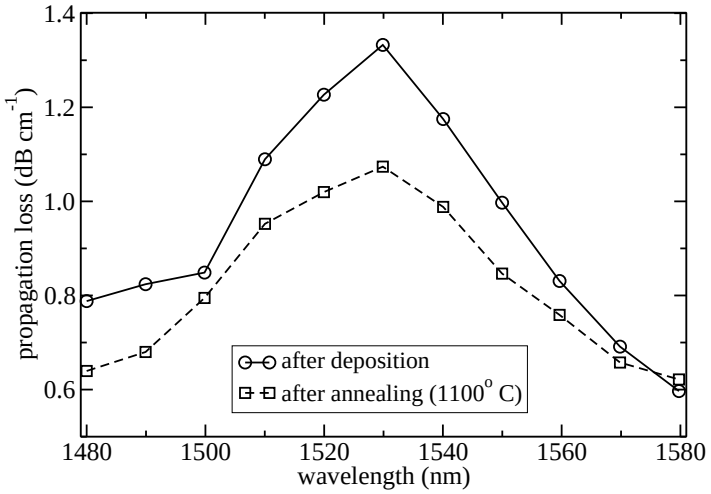

Figure 2.7: A graph of the propagation loss in a silicon rich silicon nitride film as measured with the dual prism coupler set-up in figure 2.6 [26].

couple light out of the same guided mode as the separation between the prisms was varied by translating the out-coupling prism across the surface of the wafer. The signal collected was measured as a function of the distance between the prisms. A figure for the optical propagation loss of the guided mode in the film was derived from this data. The results of the measurement are shown in figure 2.7 as a function of wavelength.

The results show that annealing reduces the attenuation in the wavelengths around $1500\,nm$. The location of a noticeable absorption peak (around $1530\,nm$) and its reduction with annealing is a good indication that $N-H$ bonds are responsible for the attenuation and that they are reduced with annealing.

2.5 Other Material Properties

Other measurements on the materials have recently been made by Karin N. Andersen. Rutherford back scattering measurements indicate that the relative proportions of silicon and nitrogen in the Si_xN_y film are between $y/x = 0.8$ and $y/x = 1.1$, depending on the mixture of gases used during deposition. X-ray diffraction measurements also confirm that the film is amorphous for annealing temperatures below $1100^\circ\,C$ and noticeable crystallization for samples annealed at $1140^\circ\,C$.

2.6 Conclusion

The combination of low stress, adjustable refractive index, low optical loss and reasonably good lithographic behavior makes the use of amorphous silicon rich silicon nitride for optical waveguiding attractive and promising. By far, the biggest disadvantage is variation in lithography and the difficulties this presents with design parameters such as coupling gaps. Some groups have used multi-layer techniques and planarizing to make ring resonators in multi-layer structures [31]. In this case the gaps are controlled by a film thickness. Other groups have recently used e-beam lithography to define structures and have demonstrated great control over fine features [32]. This allows for extremely small coupling gaps (e.g. $60\,nm$). These techniques were not used. Instead, wider coupling

gaps and longer coupling lengths were used in an attempt to make single layer devices. This has a disadvantage of increasing the length of resonator (decreasing the free spectral range), but also avoids problems with multi-layer alignment and follows techniques that might be useful for relatively high throughput commercial production of devices.

Chapter 3

High Index Contrast Waveguiding

The waveguides and waveguide based devices studied during this project have a core made of amorphous silicon rich silicon nitride (Si_xN_y) and a cladding of silica (SiO_2). The optical refractive index of amorphous silicon rich silicon nitride is adjustable and depends on the mixture of gasses used during deposition [27]. The refractive index of the core material was typically chosen to be 2.06 at a wavelength of $1.55\,\mu m$. The refractive index of the cladding was that of pure silica, 1.44 at a wavelength of $1.55\,\mu m$, though there are some notable exceptions that will be discussed later in the chapter on UV-engineered hybrid devices.

Given this as a basis for an optical waveguiding system, the question that needs to be answered is , "what can be done with it?" Some general answers to this question are given – first in a fundamental way, starting off with Maxwell's equations and noting some waveguiding properties that might be surprising to those accustomed to lower-index contrast waveguides and the weak guidance approximation [33]. Then some specifics of amorphous silicon rich silicon nitride waveguides are explored - including some predictions of performance and expected difficulties.

The chapter ends with discussion of some experimental results that indicate the usefulness of silicon rich silicon nitride waveguides for high-density integrated optics.

3.1 Wave Equation

The behavior of high-index contrast optical waveguides follow directly from classical electromagnetism, and Maxwell's equations are given here in *mks* units for completeness and reference. It has been assumed that the structures under consideration are made of dielectric materials and that there are no free charges present.

$$\boldsymbol{\nabla} \cdot \boldsymbol{D} = 0 \tag{3.1}$$

$$\boldsymbol{\nabla} \cdot \boldsymbol{B} = 0 \tag{3.2}$$

$$\boldsymbol{\nabla} \times \boldsymbol{H} = \frac{\partial}{\partial t}\boldsymbol{D} \tag{3.3}$$

$$\boldsymbol{\nabla} \times \boldsymbol{E} = -\frac{\partial}{\partial t}\boldsymbol{B} \tag{3.4}$$

Where $\boldsymbol{D}$ is the electric displacement field, $\boldsymbol{E}$ is the electrics field, $\boldsymbol{B}$ is the magnetic flux density, and $\boldsymbol{H}$ is the magnetic field. The vectorial quantities ($\boldsymbol{E}$, $\boldsymbol{D}$, $\boldsymbol{H}$, and $\boldsymbol{B}$) are not independent and are related to one another through the constitutive relations. For a linear, isotropic media, these relations are given by: $\boldsymbol{D} = \epsilon\boldsymbol{E}$ and $\boldsymbol{B} = \mu\boldsymbol{H}$, where ϵ is the scalar[1] bulk permittivity and μ is the scalar bulk permeability. The permittivity may be defined as $\epsilon = \epsilon_r\epsilon_o$ where ϵ_o is the permittivity of free space and ϵ_r is the relative permittivity. Likewise, the permeability may be defined as $\mu = \mu_r\mu_o$, but when not dealing with magnetic materials the relative permeability is unity, so that $\mu = \mu_o$.

For idealized, passive waveguides it is assumed that the permittivity is a function of spatial coordinates, but not a function of time. Taking the curl of the Faraday equation 3.4 and applying these assumptions, the following equation is obtained:

$$\boldsymbol{\nabla}^2\boldsymbol{E} - \mu\epsilon\frac{\partial^2}{\partial t^2}\boldsymbol{E} = \boldsymbol{\nabla}(\boldsymbol{\nabla} \cdot \boldsymbol{E}) \tag{3.5}$$

This can be reduced further with the application of some vector identities to the form (see Appendix A) [33, 34]:

[1] The permitivitty is generally a tensor, but is recued to a scalar in an isotropic medium.

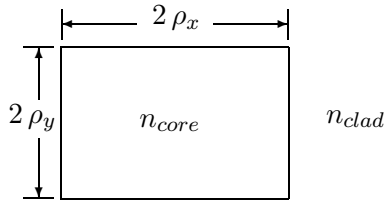

Figure 3.1: simple waveguide cross-section

$$\boldsymbol{\nabla}^2\boldsymbol{E} - \mu\epsilon\frac{\partial^2}{\partial t^2}\boldsymbol{E} = -2\boldsymbol{\nabla}(\boldsymbol{\nabla} ln(n)\cdot\boldsymbol{E}) \tag{3.6}$$

where n is the refractive index and is defined as $n = \sqrt{\epsilon_r}$.

The left hand side of equation 3.6 has arguments associated with the wave equation and the right hand side of equation 3.6 is a consequence of the refractive index being a function of the spatial variables. In optical waveguides with a low-index contrast, it is assumed that the term on the right hand side will be approximately zero since the variation in the index is small. This is the weak guidance approximation [33]. For high-index contrast waveguides this term is typically not negligible across the total waveguide cross-section. For an idealized model of a waveguide that assumes the core is defined by step-like functions of the refractive index, the continuous representation is also problematic since the idealized refractive index is discontinuous at the boundary. This makes the gradient of the index (or the natural log of the index) undefined along that boundary.

Equation 3.6 is reduced to a more familiar form by assuming that the refractive index is a constant and that the electric field, $\boldsymbol{E}$, can be written in the form $\boldsymbol{E}(\boldsymbol{r},t) = \boldsymbol{E}(\boldsymbol{r})e^{i\omega t}$, where ω is the angular frequency and $\boldsymbol{r}$

is a vector defining the spatial coordinates. This is done without loss of generality because a general solution can be found for each of the areas of constant refractive index, and boundary conditions can be applied later. Furthermore, the time response can be recovered by an inverse Fourier transform [35]. Equation 3.6 can then be expressed as the Helmholtz equation:

$$\boldsymbol{\nabla}^2\boldsymbol{E} + \mu\epsilon\omega^2\boldsymbol{E} = 0 \tag{3.7}$$

Making the substitutions : $\omega = \frac{2\pi c}{\lambda}$ and $\mu\epsilon = \frac{n^2}{c^2}$, where λ is the vacuum wavelength, and c is the speed of light in a vacuum, the following equation is obtained:

$$\boldsymbol{\nabla}^2\boldsymbol{E} + \frac{4\pi^2 n^2}{\lambda^2}\boldsymbol{E} = 0 \tag{3.8}$$

In defining the waveguide structure, the z-axis is taken to be the optical axis, and, as such, the direction a guided mode propagates along the waveguide. Accordingly, the x and y coordinates are transverse with respect to the direction of propagation, and the Laplacian operator can be divided into a transverse term and a propagation term. This separation can be designated in mathematical notation as [33]: $\boldsymbol{\nabla}^2 = \boldsymbol{\nabla}_t^2 + \frac{\partial^2}{\partial z^2}$, where $\boldsymbol{\nabla}_t^2 = \frac{\partial^2}{\partial x^2} + \frac{\partial^2}{\partial y^2}$. Substituting this representation of the Laplacian, equation 3.8 becomes:

$$\boldsymbol{\nabla}_t^2\boldsymbol{E} + k_o^2 n^2\boldsymbol{E} = \beta^2\boldsymbol{E} \tag{3.9}$$

Where β represents the propagation constant that is defined by assuming the $\boldsymbol{E}(\boldsymbol{r}) = \boldsymbol{E}(x,y)e^{-i\beta z}$, and k_o is the magnitude of the vacuum wave vector, defined as $k_o = \frac{2\pi}{\lambda}$. Equation 3.9 is an eigenvalue equation, where β^2 is the eigenvalue, and $\boldsymbol{E}(x,y)$ is the eigenfunction. A term that will be useful later, the effective index (n_{eff}), can be defined as $n_{eff} = \frac{\beta}{k_o}$.

Equation 3.9 is a vector equation and represents 3 scalar equations. A similar equation can be derived for $\boldsymbol{H}$. For a waveguide with a rectangular cross-section, there is no known analytical solution satisfying the general solution of the equations and the boundary conditions. Approximations (e.g. the Marcatili approximation [2]) and numerical techniques

(e.g. finite difference [36], and Wave Matching Method [37]) are generally used to find a solution. At least two relevant, and not independent, pieces information can be gleaned from the solutions obtained numerically or by approximation. The first is the effective index, which is the equivalent of the eigenvalue, for any given mode. The second is a detailed mode profile, consisting of the various vectorial components of the electromagnetic field. This can be used for calculations dealing with projections (e.g. coupling form one mode to another at the interface of two waveguides) and evanescent coupling (e.g. that which happens when waveguides in close proximity start exchange power).

For any given waveguide, there are a set of discrete effective indexes that correspond to bound, propagating modes. This set may have a size of zero if the waveguide is ill-defined, but if consideration is restricted to those waveguides having a cross-sectional geometry shown in figure 3.1, i.e. a rectangular core region surrounded by a homogeneous cladding layer; refractive indexes, n_{core} and n_{clad}, which are real; and a core material that has a higher refractive index than the cladding ($n_{core} > n_{clad}$), then there will be guided modes. The limit as the area of the core goes to zero will correspond to a plane wave propagating along the z-axis in the cladding material and this amounts to the fundamental mode having expanded in an infinite extent.

A fundamental result of the boundary conditions is that guided modes must have an effective index between the refractive indexes of the cladding and core materials. This seemingly simple property has many implications for high-index contrast waveguides. Compared to relatively low-index contrast waveguides, high-index contrast waveguides have a wider range of possible effective indexes associated with guided modes. The actual discrete value of the effective index for any particular mode being determined by the waveguide geometry (which determines the boundary conditions). This translates directly into a higher variation of waveguide properties as the waveguide dimensions change. Furthermore, polarization effects are also accentuated by the high index contrast so that small asymmetries can lead to large birefringence and polarization mode dispersion.

3.2 Modes

When using waveguides for the transmission of information, group velocity dispersion can degrade the signal and it is therefore important to understand its basis in the properties of propagating modes. Dispersion has several origins, including material dispersion, modal dispersion, polarization mode dispersion, and geometrically induced (or waveguide) dispersion. The last three of these are influenced by waveguide geometry and, in the case of high-index contrast waveguides, waveguide geometry is often the dominant contributing factor. For this reason, some general properties of propagation of modes are addressed and the magnitude of some effects calculated with special emphasis on the geometric effects.

3.2.1 Single Mode

If polarization effects are momentarily ignored, the question of eliminating modal dispersion is a question of keeping the waveguide core small enough so that only the fundamental mode is a bound solution to the eigenvalue equation seen in the last section (equation 3.9). In other words, only one eigenvalue that corresponds to just one propagation constant (or effective index) is desired.

For a first approximation of single mode criteria, the definition of the V-parameter (or waveguide parameter) for waveguide with a rectangular cross-section is recalled [33]:

$$V = \frac{2\pi}{\lambda}\rho n_{core}\sqrt{2\Delta} = \frac{2\pi}{\lambda}\rho\sqrt{n_{core}^2 - n_{clad}^2} \tag{3.10}$$

where Δ is the relative index difference and is defined as $\Delta = \frac{n_{core}^2 - n_{clad}^2}{2n_{core}^2}$; and $\rho = \sqrt{\rho_x \rho_y}$ where ρ_x and ρ_y are the half widths of the waveguide shown in figure 3.1. This parameter is roughly analogous to the V-parameter (normalized frequency) of fibers [10] and can be used to provide an estimate of the dimensions of a square waveguide that correspond to the cut-off of the first anti-symmetric mode (i.e. a single mode criterion). If we consider the a silicon rich silicon nitride core ($n_{core} = 2.06$ at $\lambda = 1550\,nm$) with a silica cladding ($n_{clad} = 1.44$ at $\lambda = 1550\,nm$) and follow suggestions for $V = 2.131$ [33], then $2\rho = 0.7\,\mu m$.

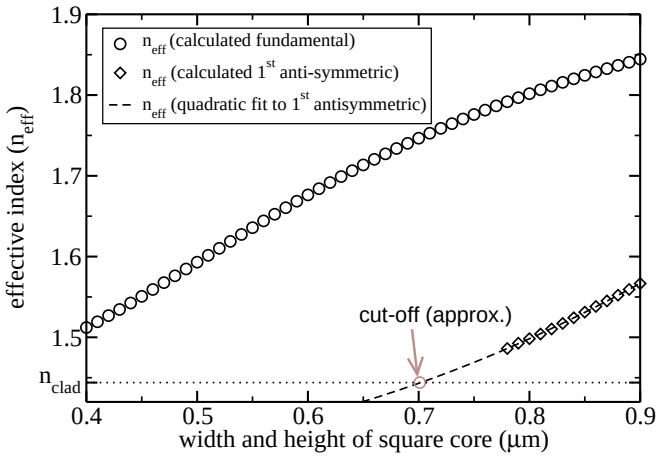

Figure 3.2: Shows the approximate cut-off of the first anti-symmetric mode of a silicon rich silicon nitride waveguide with a core having a square cross-section. This defines the single mode criteria for high-index contrast (amorphous silicon rich silicon nitride) waveguides.

The V-parameter offer an approximation of the single mode condition but it is generally only valid for waveguides that are nearly symmetric, and direct calculation of the cut-off can be quite difficult since, as previously mentioned, there are no analytical solutions. Numerical techniques are notoriously poor at calculating cut-off conditions since modes near cut-off are not well confined and many numerical techniques rely on a finite calculation window and/or search for extrema in some figure of merit that is difficult to distinguish for values that correspond to a situation in which the effective index approaches the boundaries of what is physically meaningful.

Two methods have been commonly used to calculate modal properties for this project: the finite difference method using BBV Olympios Software and the Wave Matching Method (WMM) [37]. The single mode criteria can be approximated with numerical techniques by extrapolation of the effective index associated with the the first antisymmetric mode as a function of waveguide dimensions and finding the intersection of this with the cladding index. This is shown in figure 3.2. For square core waveguides, this is generally in good agreement with the approximation using the V-parameter.

3.2.2 Polarization: Birefringence

Gauss' equation (equation 3.1), Faraday's equation (equation 3.4) and the constitutive relations describe an electric field, $\boldsymbol{E}$, that must obey certain boundary conditions. These boundary conditions lead to a discontinuity in the component of the electric field that is perpendicular to an interface between two materials with different refractive indexes. The component of the electric field that is parallel to the interface is, however, continuous. Simply stated, the boundary conditions are:

$$n_1^2 E_{1\perp} = n_2^2 E_{2\perp} \tag{3.11}$$

$$E_{1\parallel} = E_{2\parallel} \tag{3.12}$$

where $E_{1\perp}$, and $E_{2\perp}$ are the electric field components on either side of a boundary that are perpendicular to that boundary; $E_{1\parallel}$ and $E_{2\parallel}$

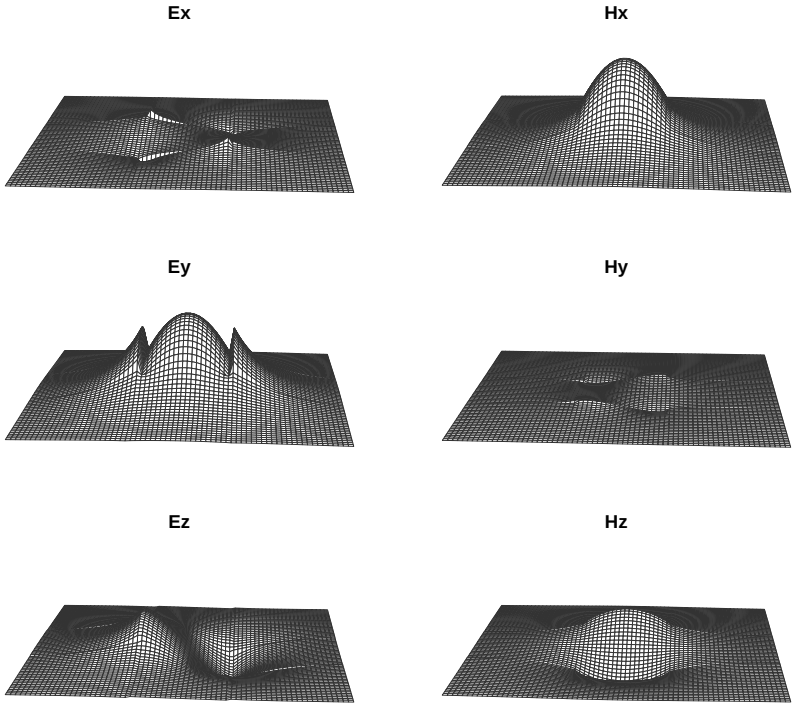

Figure 3.3: Magnitude of field components for a $0.6\,\mu m \times 0.6\,\mu m$ silicon rich silicon nitride waveguide. The mode corresponds to the (quasi-)TE polarization.

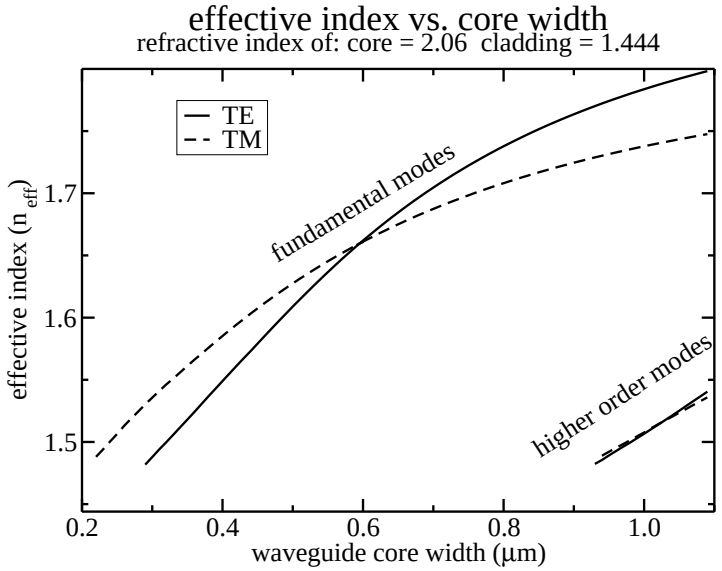

Figure 3.4: The calculated effective index of $0.6\,\mu m$ silicon rich silicon nitride waveguides as a function of waveguide width. Note the geometrically induced birefringence for waveguides not having a symmetric core.

are the parallel components of the electric field; and n_1 and n_2 are the refractive indexes on either side of the boundary. Under the assumptions of the model being used (no free charges and a constant permeability), all components of $\boldsymbol{H}$ are continuous.

For high-index silicon rich silicon nitride waveguides that normally have a core with an index of $n_{core} = 2.06$ at $1550\,nm$ and are clad with silica that has an index of $n_{clad} = 1.44$ at $1550\,nm$ this means that the E-field is discontinuous at the boundary by approximately a factor of 2 (i.e. $E_{clad\perp} \approx 2E_{core\perp}$). Figure 3.3 shows the field components of a mode guided in a $0.6\,\mu m \times 0.6\,\mu m$ waveguide. The magnitude of the electric field in the y direction, E_y clearly displays the discontinuity.

This discontinuity has consequences for coupling between waveguides (e.g. a directional coupler) which relies on the overlap of the evanescent fields, and, perhaps more importantly, it has consequences on the

propagation constant of the mode. Generally speaking, a waveguide will have different propagation constants for different polarizations simply by virtue of the morphology of the waveguide (neglecting material effects). The only case this is not true, by definition, is when there is a degeneracy in propagation constants. For simple waveguide geometries (e.g. shown in figure 3.1) this is the result of symmetry with respect to a 90° rotation. In other words, the propagation constants (effective indexes) of different polarization is the same if the waveguide has a square core and a homogeneous cladding. When the geometry does not display this symmetry, the propagation constants (effective indexes) diverge as shown in figure 3.4, where the effective indexes of a $0.6\,\mu m$ thick waveguide is shown as a function of waveguide width. Notice in figure 3.4 the effective indexes of the two different polarizations cross when the width of the waveguide is $0.6\,\mu m$ (e.g. the waveguide is symmetric).

For useful photonic devices, the situation is more complicated and cannot be solved by simply using square waveguides. Useful devices generally require more than simple straight waveguides. The cross-sections of structures like directional couplers do not display symmetry with a 90° rotation and bent waveguides can induce polarization effects [38].

When considering simple straight waveguides, the geometric effects on birefringence must be quantified in a way that allows a meaningful analysis of the impact of cross-sectional geometry on mode propagation. There are three quantities of interest that indicate how well the propagation properties of the modes are known. These three quantities are the variation of the effective index associated with the two polarizations (TE and TM) as a function of waveguide dimension, and the difference in the effective indexes (i.e. birefringence) as a function of waveguide dimension. If we define the birefringence as $\Delta n = (n_{TEeff} - n_{TMeff})$, then the errors associated with these quantities are:

$$\sigma^2_{n_{TEeff}} = \left(\frac{\partial n_{TEeff}}{\partial w}\right)^2 \sigma^2_w \tag{3.13}$$

$$\sigma^2_{n_{TMeff}} = \left(\frac{\partial n_{TMeff}}{\partial w}\right)^2 \sigma^2_w \tag{3.14}$$

$$\sigma_{\Delta n}^2 = \left(\frac{\partial n_{TEeff}}{\partial w} - \frac{\partial n_{TMeff}}{\partial w}\right)^2 \sigma_w^2 \tag{3.15}$$

where w is the waveguide width, n_{TEeff} is the effective index of the TE polarization and n_{TMeff} is the effective index of the TM polarization. Values for partial derivative when $n_{TMeff} = n_{TEeff}$, which corresponds to a waveguide with a square core, can be obtained for the situation shown in figure 3.4 and are:

$$\frac{\partial n_{TEeff}}{\partial w} \approx 0.5\,\mu m^{-1} \quad \frac{\partial n_{TMeff}}{\partial w} \approx 0.3\,\mu m^{-1} \quad \frac{\partial \Delta n}{\partial w} \approx 0.2\,\mu m^{-1} \tag{3.16}$$

Some sample calculations using these values yield a need for extremely tight tolerances. For instance, if birefringence less than 10^{-2} (i.e. $|\Delta n| < 10^{-2}$) is desired, the total error associated with the width of a waveguide with a nominally square cross-sectional core should be less than roughly $0.05\,\mu m$ or $50\,nm$, assuming that the origin of the birefringence is purely from the geometry of the waveguide. Errors in the absolute thickness of the film can also affect these values as well as processing variations that may contribute more than simple linewidth reduction to the waveguide index profile. Variations in processing that lead to trapezoidal core shapes or diffusion at the boundaries defining the waveguide can also be expected to have potentially significant effects.

It is interesting to note that the variation of waveguide properties continues to increase as the index contrast increases. For SOI technology, the extreme index contrast causes an amplified dependence on waveguide dimensions. A $0.3\,\mu m \times 0.3\,\mu m$ silicon waveguide clad in silica, as has been used by some groups [39], has the following variations in effective index and birefringence with waveguide geometry:

$$\frac{\partial n_{TEeff}}{\partial w} \approx 4.5\,\mu m^{-1} \quad \frac{\partial n_{TMeff}}{\partial w} \approx 1.8\,\mu m^{-1} \quad \frac{\partial \Delta n}{\partial w} \approx 2.7\,\mu m^{-1} \tag{3.17}$$

This means the required processing tolerances are about an order of magnitude higher for SOI technology.

The sensitivity of the effective index to waveguide geometry continues to have effects for the group velocity and dispersion.

3.2.3 Polarization: Effective Group Index

The variation of effective index associated with the fundamental mode in high-index contrast waveguides has been explored for some typical waveguide geometries. The results indicate that tight tolerances are required if reasonable control over the propagation properties of light guided in high-index contrast waveguides is desired. The effective index does not just vary as a function of waveguide dimensions, it also varies with the wavelength. Longer wavelengths tend to be less confined and have lower effective indexes. The geometric origins of this variation associated with the waveguide cross-section can be explored by assuming that the refractive index of the materials doesn't change significantly over the wavelength range being considered.

The group velocity of a guided mode, v_g, is given by [36]:

$$v_g = \frac{1}{\frac{\partial \beta}{\partial \omega}} \tag{3.18}$$

where β is the propagation constant and ω is the angular frequency. The angular frequency is related to the wavelength through the expression $\omega = 2\pi\frac{c}{\lambda}$, and the propagation constant is related to the effective index through $\beta = n_{eff}\frac{2\pi}{\lambda}$. The chain rule can be applied and an expression for the group velocity derived.

$$v_g = \frac{c}{n - \lambda\frac{\partial n_{eff}}{\partial \lambda}} \tag{3.19}$$

$$= \frac{c}{n_g} \tag{3.20}$$

where it has been assumed that the effective index is a function of the wavelength, and n_g is the effective group index associated with a mode. The effective group index is a ubiquitous term when dealing with waveguides. When dealing with quantities derived from changes in wavelength, the effective group index is often encountered. One example of this is the free spectral range of Mach-Zehnder interferometers.

Figure 3.5 shows some sample calculations of the effective index a function of wavelength. Two cases are shown, one that corresponds to a

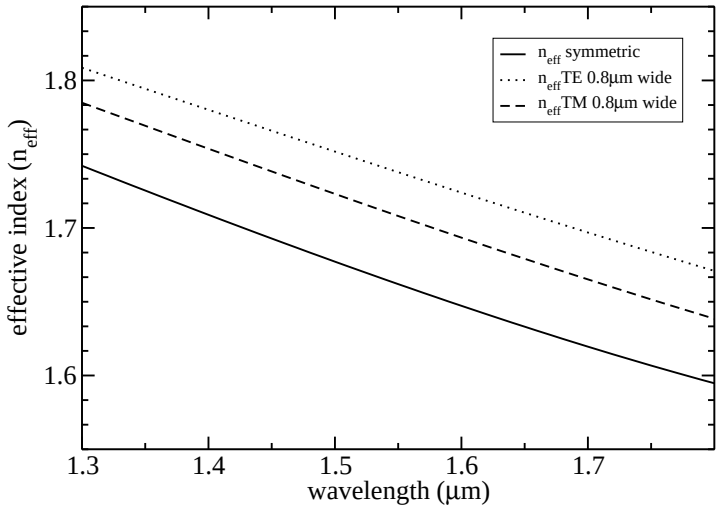

Figure 3.5: the calculated effective index of high-index contrast waveguides, based solely on waveguide geometry, with two different cross-sectional dimensions: $0.6 \times 0.6\,\mu m$, referred to as symmetric; and $0.8 \times 0.6\,\mu m$ referred to by the width, $0.8\,\mu m$. Note that the polarizations are degenerate in the symmetric case.

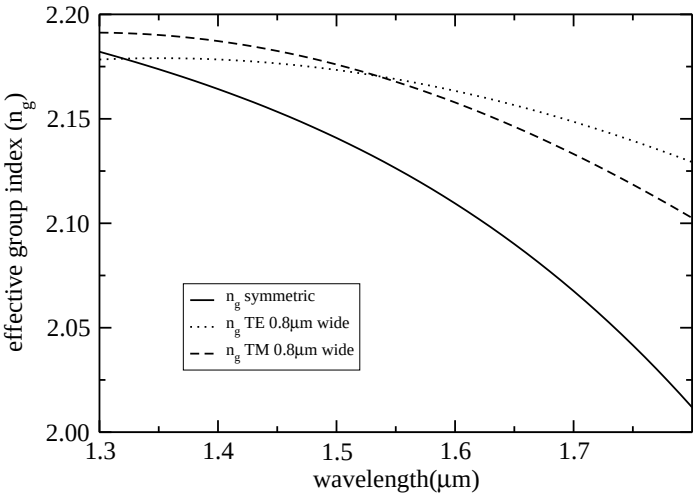

Figure 3.6: the calculated effective group index of high-index contrast waveguides, based solely on waveguide geometry, with two different cross-sectional dimensions: $0.6 \times 0.6\,\mu m$, referred to as symmetric; and $0.8 \times 0.6\,\mu m$ referred to by the width, $0.8\,\mu m$. Note that the polarizations are degenerate in the symmetric case.

waveguide with a square core ($0.6\,\mu m \times 0.6\,\mu m$) and one that corresponds to a waveguide with rectangular core dimensions of $0.6\,\mu m \times 0.8\,\mu m$. In the latter case, the polarization modes are split.

Taking this one step further and calculating the effective group index, the graph in figure 3.6 is obtained. The effective group indexes vary significantly and, interestingly, even a waveguide that is significantly asymmetric and has significance birefringence can have an intersection of the group index at particular wavelength – in this case, at a wavelength of $1.535\,\mu m$.

3.2.4 Waveguide Dispersion

The definition of waveguide dispersion is easily derived by noting that the time, t, it takes for a wavepacket to transverse a distance,L, is given by $t = \frac{Ln_g(\lambda)}{c}$. Differentiating, the following is obtained:

$$\Delta t = \frac{L}{c}\frac{\partial n_g}{\partial \lambda}\Delta\lambda \tag{3.21}$$

$$= -\frac{L\lambda}{c}\frac{\partial^2 n_{eff}}{\partial \lambda^2}\Delta\lambda \tag{3.22}$$

The dispersion is defined as $\mathcal{D} = \frac{\Delta t}{L\Delta\lambda}$ and offers a description of how the differential delay, Δt, over a length of fiber, L, relates to the bandwidth, $\Delta\lambda$. The dispersion parameter explicitly written is given by the following expression:

$$\mathcal{D} = \frac{\Delta t}{L\Delta\lambda} = -\frac{\lambda}{c}\frac{\partial^2 n_{eff}}{\partial \lambda^2} \tag{3.23}$$

A graph of the waveguide dispersion for high-index contrast waveguides is shown in figure 3.7. These values greatly exceed those associated with standard optical fiber [10] and are a good indication of one reason [2] high-index contrast waveguides can present problems when used as a medium for long distance transmission of signal.

[2] another reason is that higher index contrasts lead to higher loss for a given sidewall roughness.

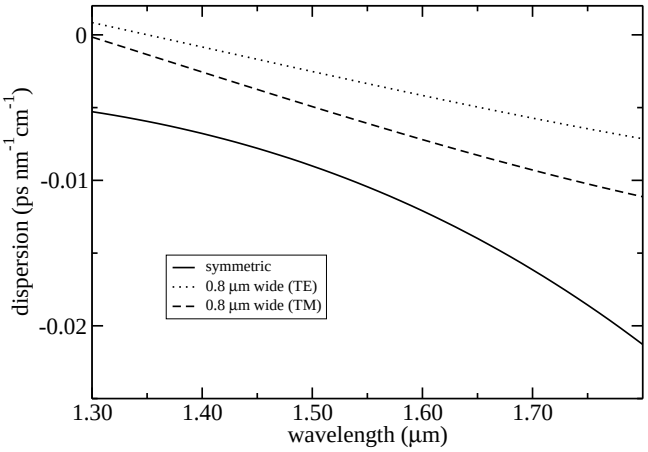

Figure 3.7: the calculated dispersion, $\mathcal{D}$, of high-index contrast waveguides, based solely on waveguide geometry, with two different cross-sectional dimensions: $0.6 \times 0.6\,\mu m$, referred to as symmetric; and $0.8 \times 0.6\,\mu m$ referred to by the width, $0.8\,\mu m$. The dispersion is given in units of $ps\,nm^{-1}cm^{-1}$ instead of the traditional units of $ps\,nm^{-1}km^{-1}$ to better match the dimensions usually associated with integrated optical circuits.

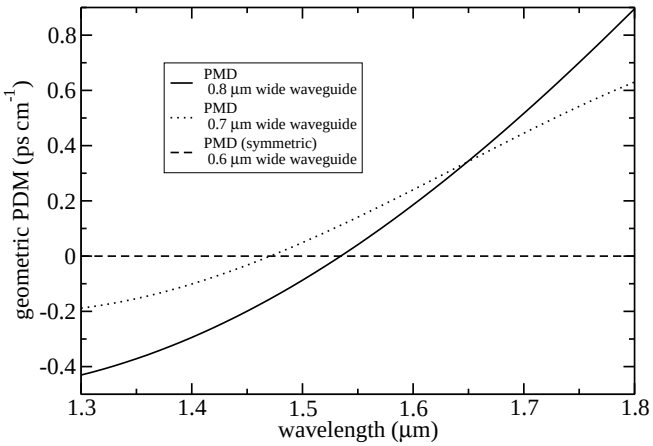

Figure 3.8: the calculated polarization mode dispersion (PMD) for three different waveguide geometries: $0.8\,\mu m \times 0.6\,\mu m$, $0.7\,\mu m \times 0.6\,\mu m$, and $0.6\,\mu m \times 0.6\,\mu m$.

3.2.5 Polarization Mode Dispersion

The different group velocities for the TE and TM polarizations leads to polarization mode dispersion (PMD). Figure 3.6 shows the different group indexes associated with the polarizations as a function of wavelength for two waveguides – one that is symmetric where the group index is degenerate with respect to the polarization; and one that is asymmetric. As was noted, in the asymmetric case there is one wavelength where these curves intersect, and at this point there is no polarization mode dispersion originating from the asymmetry of the waveguide. This is, however, not a broad-band effect and generally speaking the more asymmetric the waveguide becomes, the more polarization mode dispersion there will be.

The PMD for three different waveguide geometries is shown in figure 3.8. When compared to the waveguide dispersion in figure 3.7, PMD is rightly considered a greater problem - though the saving factor is that

high-index contrast devices generally have a functional length of much less than a centimeter.

3.2.6 Modal Confinement

The modal confinement is defined as the fraction of the power in a guided mode traveling along a waveguide that is confined to the core region. It is related to the effective index and for a given core and cladding materials, it is expected that a higher effective index generally translates into a higher modal confinement. The fundamental mode tends to be the most confined just as it tends to have the highest effective index. The fundamental mode's fractional power confinement of a $0.6\,\mu m \times 0.6\,\mu m$ waveguide core of silicon rich silicon nitride clad with glass at a wavelength of $1550\,nm$ is expected to be approximately 0.68 (as calculated with BBV Olympios software).

Related to the modal confinement is the spot size of the propagating field and the optical intensity. When the modes are highly confined in a small core the optical intensity is high. The spot size (beam radius) of a $0.6\,\mu m \times 0.6\,\mu m$ waveguide core of silicon rich silicon nitride clad with glass at a wavelength of $1550\,nm$ is approximately $0.58\,\mu m$ (e^{-2} waist of the power density), when making a Gaussian approximation (reference for Gaussian approximation [33]). This means the optical intensity for $0\,dBm$ is approximately [36]:

$$I = \frac{P}{\pi w^2} = \frac{1\,mW}{\pi(0.58\,\mu m)^2} = 9.4 \times 10^4 \frac{W}{cm^2} \tag{3.24}$$

The intensity is about 80 times that of a typical germanium doped silica waveguide with a spot size of $\approx 5.2\,\mu m$ at $1550\,nm$. This increase in modal confinement for waveguides with small core dimensions (e.g. $0.6\,\mu m \times 0.6\,\mu m$) can be helpful when exploiting non-linear behavior in waveguides and will be discussed further in chapter 6.

3.2.7 Coupling to Standard Optical Fiber

Integrated optical circuits should be able to efficiently couple to standard optical fiber if they are to be deployed in existing optical networks.

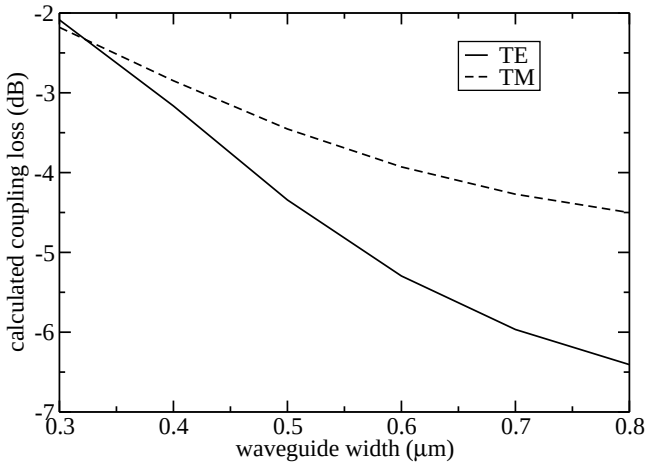

Figure 3.9: calculated coupling loss between fiber with a waist of $3\mu m$ and a $0.33\mu m$ thick high silicon rich silicon nitride waveguide. There is significant variation with waveguide width corresponding to modal expansion of narrow waveguides.

High-index contrast waveguides, with their comparatively small mode size, generally have high losses at the interface to standard optical fiber because of modal mismatch between the waveguides. A standard optical fiber coupled to a $0.6\,\mu m \times 0.6\,\mu m$ silicon rich silicon nitride waveguide will typically have loss in excess of $8\,dB$ at the interface (calculated at $1550\,nm$).

For measurements on high index structures, high-index contrast fibers were used for connecting to devices. The spot size of this fiber was about $3\,\mu m$ (signifying the radius of the spot defined by the point at which the modal power is reduced to e^{-2} of its maximum). This reduced the coupling loss to about $7\,dB$ per interface. Since this does represent a major obstacle to the effective use of high-index components in optical networks, two basic approaches to decreasing the coupling loss were explored. The first was the combination of low-index contrast direct UV-written wave-

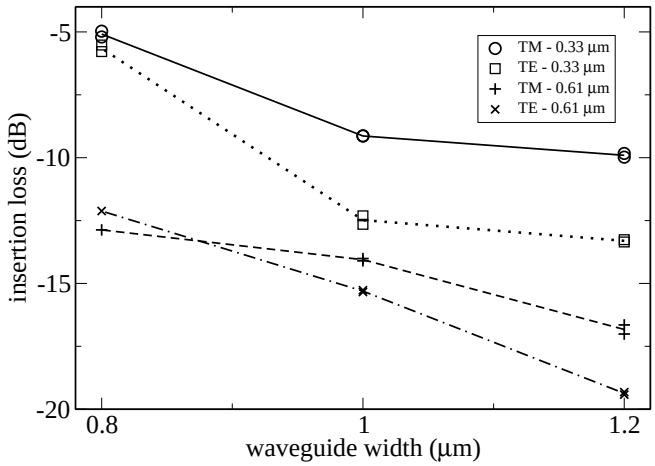

Figure 3.10: measured insertion loss for $0.33\mu m$ and $0.61\mu m$ thick waveguides as a function of waveguide width. The insertion loss has two components - the coupling loss at the two interfaces, and the propagation loss. The fiber used had a beam waist of approximately $3\mu m$. The waveguides were $1.5\,cm$ long.

guides and high-index contrast waveguides on the same chip. This has a number of technical challenges and is the subject of another chapter. The second approach used was to reduce the cross-sectional dimensions of the waveguide. It is well known that reduction of the waveguide core can cause an expansion of the fundamental mode [33]. If the core dimensions are small enough the size of the fundamental mode of the high-index contrast waveguide will approach the dimensions of the mode size of standard optical fiber. The expanded mode size will, however, also tend to diminish the advantages, i.e. small bending radius, of high-index contrast waveguides. So, for practical devices a taper can be used [40].

Figure 3.9 shows the calculated coupling loss between a relatively high-index contrast fiber (having a beam waist of $0.3\,\mu m$) and $0.33\mu m$ thick silicon rich silicon nitride waveguides. The coupling loss is shown as a function of waveguide width. A measurement of the insertion loss of a silicon rich silicon nitride waveguide made from a $0.33\mu m$ thick film is shown in figure 3.10. The measurement is shown as a function of the waveguide width as designed on the photolithographic mask. The linewidth reduction of this sample was measured with an optical microscope to be between $0.3\,\mu m$ and $0.4\,\mu m$. The insertion loss however shows that the effective width of the waveguide more closely matches that associated with a thinner waveguide. The reason for this is not known but could be the result of diffusion, non-rectangular shape of the waveguide, or a linewidth reduction that is not uniform for all waveguides. The important result is that coupling loss is significantly reduced and that these high-index contrast waveguide can have small radii of curvature with low loss as will be discussed in the section on bending loss. This means that devices that take advantage of the low coupling loss and tight bending radii are possible with the given platform.

3.3 Directional Couplers

3.3.1 Modal Approach

Directional couplers are essential building blocks of integrated optical filters, and as such, if the advantages of high-index contrast waveguides

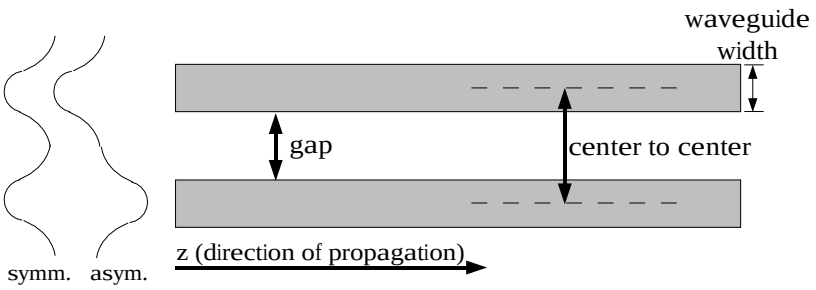

Figure 3.11: A diagram of a directional coupler defining some important dimensions.

are to be realized, then coupling structures need to be analyzed. This is particularly important since waveguide structures that have asymmetric cross sections are inherently birefringent, and the typical cross-section of a directional coupler is asymmetric. A diagram of a coupler is shown in figure 3.11.

Analysis of directional couplers can proceed in two fundamental and related ways. The first is through coupled mode theory [41], the second is to look at the propagation constants of the symmetric and antisymmetric modes (i.e. supermodes). The second method is preferred here, but it should be noted that within the limits of the solution of the coupler structures being nicely approximated by a linear combination of the modal solutions of the individual waveguides, these approaches are equivalent. It is assumed that the couplers have two different modes for a given polarization. These modes are the symmetric and anti-symmetric modes and are roughly represented as a linear combination of the fundamental modes associated with the single, isolated, waveguides. These have propagation constants (related to the eigenvalues) given by β_{sym} and β_{asym} for the symmetric and anti-symmetric modes, respectively. These correspond to symmetric and anti-symmetric state vectors and an expression for the propagation in a coupler is given by:

$$\psi(z) = \frac{A}{\sqrt{2}} \begin{pmatrix} 1 \\ 1 \end{pmatrix} e^{-i\beta_{sym}z} + \frac{B}{\sqrt{2}} \begin{pmatrix} 1 \\ -1 \end{pmatrix} e^{-i\beta_{asym}z} \tag{3.25}$$

where A and B are arbitrary constants that define the amplitudes of the symmetric and antisymmetric modes, and $\psi(z)$ corresponds to the field amplitude associated with the modes. When a guided mode of one waveguide excites the coupler, it's amplitude is projected onto the state vectors and an oscillatory transfer of energy begins between the two waveguides. For instance, consider the input being the vector: $\begin{pmatrix} 1 \\ 0 \end{pmatrix}$. The projection onto the coupler, properly normalized, would yield an expression for $\psi(z)$ given by:

$$\psi(z) = \frac{1}{2} \left(\begin{pmatrix} 1 \\ 1 \end{pmatrix} e^{-i\beta_{sym}z} + \begin{pmatrix} 1 \\ -1 \end{pmatrix} e^{-i\beta_{asym}z} \right) \tag{3.26}$$

considering only the top waveguide (i.e. $\psi_{top} = (1, 0) \cdot \psi(z)$) the expression for the power in the top waveguide becomes:

$$P_{top} = \psi_{top}\psi^*_{top} = \frac{1}{2} + \frac{1}{2}\cos(\Delta\beta\, z) \tag{3.27}$$

where the following substitutions for the propagation constants have been made:

$$\beta_{sym} = \beta + \frac{\Delta\beta}{2} \qquad \beta_{asym} = \beta - \frac{\Delta\beta}{2} \tag{3.28}$$

With this, it is possible to define a coupling length that corresponds to the length of a given directional coupler at which 100% of the power has been transferred out of the initial waveguide and to the coupling waveguide:

$$L_{coup} = \frac{\pi}{\Delta\beta} \tag{3.29}$$

Coupling gap (μm)	β^{TE}_{symm} (μm^{-1})	β^{TE}_{asymm} (μm^{-1})	$L_{coup}TE$ (μm)	β^{TM}_{symm} (μm^{-1})	β^{TM}_{asymm} (μm^{-1})	$L_{coup}TM$ (μm)
1.0	6.7464	6.7282	171.8	6.7442	6.7261	173.7
0.8	6.7564	6.7177	81.0	6.7536	6.7161	83.8
0.6	6.7771	6.6956	38.6	6.7727	6.6943	40.1

Table 3.1: Calculated coupling characteristics between two $0.6\,\mu m \times 0.6\,\mu m$ waveguides as a function of the coupling gap.

3.3.2 High-Index Couplers

With the definitions of the above section, coupling lengths can be derived using a mode solver and solving for symmetric and anti-symmetric modes of the coupler. The difference in the propagation constants (or equivalently the difference in the effective indexes) immediately yields the coupling length via equation 3.29.

Table 3.1 shows some calculated values for the coupling lengths for a coupler made with two $0.6\,\mu m \times 0.6\,\mu m$ waveguides. The separation of the waveguides is defined by the gap, as shown in figure 3.11. The values show a very sensitive dependence on the coupling gap, or equivalently, waveguide separation. The coupling length generally varies by more than a factor of two when the gap is changed by $0.2\,\mu m$. This kind of high sensitivity is expected for high index coupler - and a more instructive approach is to consider the variation of coupling as a function of process parameters. The coupling gap varies with the center to center waveguide separation and the line width reduction (see figure 3.11 for reference). If a uniform linewidth reduction is assumed, the variations in the coupling may also be calculated as a function of linewidth reduction. An example for a two different couplers is shown in figure 3.12.

Several important characteristics can be seen in figure 3.12. First, as the waveguides become asymmetric, the difference in the coupling lengths for the two different polarizations tends to be greater. This is a tendency, but it can also be seen that it is not uniformly accurate. It can also be

seen that a difference in coupling lengths for the polarizations also becomes more noticeable as the square core waveguides are brought closer together. This sort of polarization effect is not surprising since as the waveguides come closer, the propagation constants associated with the symmetric and anti-symmetric modes diverge from the propagations constants associated with a symmetric waveguide. As the difference in propagation constants becomes greater, the asymmetries of the coupler itself induce polarization effects. This means, among other things, that narrow coupling gaps (such as those used in reference [32]) will have virtually no chance of polarization independent coupling and therefore require a polarization splitting strategy.

When the waveguides making the coupler become highly asymmetric, it is also seen that the TM polarization tends to show stronger coupling. This is indicative of the lower confinement (and lower effective index) of the TM modes for "wide" waveguides (i.e. the width of the waveguides greatly exceeding the height). See figure 3.4 for reference. Coincidentally, this lower confinement not only has implications for couplers, but also bending loss.

3.4 Bending Loss

There are two fundamental mechanisms that lead to loss associated with bent waveguides. The first is pure propagation loss that comes from the lossy nature of a mode propagating in a curved waveguide. The second transition loss that occurs when a straight waveguide (or waveguide with a different curvature) is coupled to a bent waveguide [42]. To explain these, the Laplacian operator of the wave equation is transformed into cylindrical coordinates, and a local reference frame is used (this is shown appendix B). The result is that an equation analogous to the original wave equation is obtained with an equivalent index profile given by:

$$n_{eq}^2 = n^2 + 2n_{core}^2 \frac{x}{r_b} \tag{3.30}$$

where n_{eq} is the equivalent index of a curved waveguide, n is the original index profile, $2n_{core}$ is the index of the core material, r_b is the radius

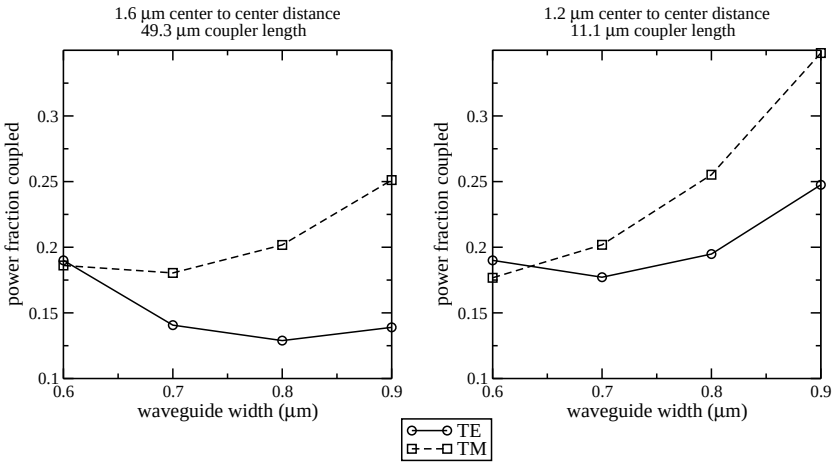

Figure 3.12: Variation in coupling with linewidth reduction. The length of the couplers were chosen to to give a 19% coupling (TE) for waveguides with a $0.6\,\mu m \times 0.6\,\mu m$ square core cross-section. The height of the waveguides are held constant at $0.6\,\mu m$.

of curvature of the waveguide, and x is the local coordinate. When the modal field extends beyond a point at which the equivalent cladding index equals the effective index of the curved waveguide, the solution becomes oscillatory. This corresponds to radiation from a propagating mode which means the mode loses power as it propagates in the waveguide. Beyond radiation, the curvature of the waveguide has also introduced an effective asymmetry to the waveguide profile. Though in the derivation of this equivalent index for a bent waveguide there was an assumption of weak guidance, the asymmetry is still instructive and indicates that polarization effects associated with waveguide curvature are expected. Some basic approximations of waveguide birefringence induced in curved waveguides have been done in reference [38].

There have been many efforts to model the properties of bent waveguides [3, 33, 43, 44]. These generally rely on numerical methods or approximations. For the purposes of this project, a numerical calculation of the expected bending loss was made and is shown in figure 3.13. The

calculations used the effective index method [45] to construct an equivalent slab waveguide structure and reduce the problem to one dimension. The result of the calculations indicate that low loss bending (less than $0.1dB$ for 6 full trips around the ring) for radii less than $25\,\mu m$ can be expected for the thicker ($0.6\,\mu m$) waveguides. Thinner ($0.33\,\mu m$) waveguide of similar widths are, however, expected to be much more lossy, particularly for the TM polarization. This gives a rough approximation of curvature loss, but since many factors can affect optical loss in bent waveguides, direct measurement of waveguide loss is preferable.

The loss of bent waveguides was measured directly by looking at the excess insertion loss associated with 24 right angle bends arranged in a repeating square wave pattern (figure 3.14) when compared to straight waveguides of similar length. Three different cross-sectional waveguide geometries were measured. Two of these had a thickness of $0.6\,\mu m$ and with width (quoted by that defined on the photolithographic mask) of $1.2\,\mu m$ and $1.0\,\mu m$. The third waveguide was $0.33\,\mu m$ thick[3] and had a width (again, quoted by that defined on the photolithographic mask) of $1.2\,\mu m$. The third waveguide geometry is interesting given the decreased insertion loss demonstrated by thin ($0.33\,\mu m$) and narrow waveguides ($0.8\,\mu m$) in section 3.2.7. Waveguide with different geometries (including $0.6\,\mu m \times 0.8\,\mu m$, $0.33\,\mu m \times 1.0\,\mu m$, and $0.33\,\mu m \times 0.8\,\mu m$), showed no discernible transmission with bending radii less than $25\,\mu m$. The measurements were done at a wavelength of $1550\,nm$.

Since the other factors such as sidewall roughness can have significant effects on losses in sharp waveguide bends, it was not expected that measured waveguide performance would match theoretical expectations based on the loss associated with propagating modes in idealized waveguides. In addition, the measurements offered no mechanism to distinguish between propagation loss and transition loss.

What the measurements do give is a conservative estimate of the optical power loss of curved waveguides and quantify its relationship to waveguide geometry. The results of measurements are shown in figure 3.15. First, the TM mode is measured to be more lossy than the TE mode. This

[3] All $0.33\,\mu m$ thick waveguides were fabricated using films supplied by Lambda Crossing.

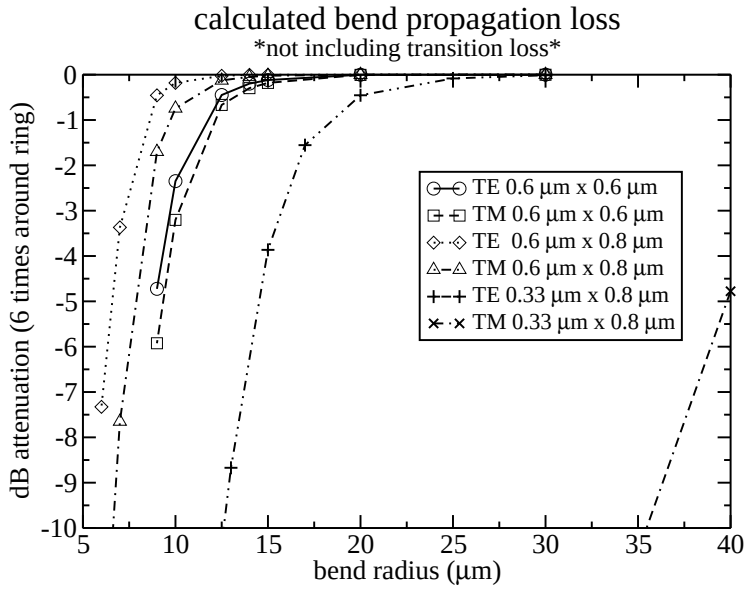

Figure 3.13: Waveguide bending loss for 6 full cycles around a ring of the given radius. The values were calculated using effective index method [46] and a slab bend loss calculation performed with BBV slab software.

is expected given the waveguide geometries measured and the earlier speculations in discussions of high-index contrast the couplers. Beyond this it is also clearly demonstrated that bend loss for the high-index contrast waveguides show low-loss (lower than can be accurately measured with the techniques used) in the sub-25 μm bend radius region. The magnitude of the loss is associated with the waveguide geometry. Wide, thick waveguides - which incidentally tend to have a higher effective index and more confined fundamental mode - demonstrated the lowest loss. Narrower waveguides showed more loss.

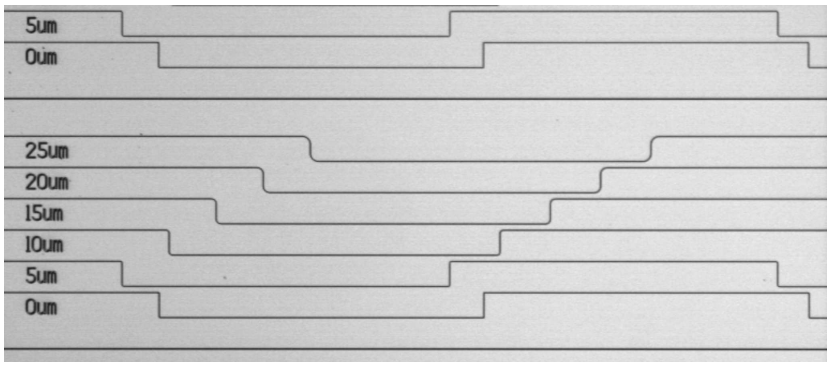

Figure 3.14: waveguides used to measure bending loss. The waveguides are arranged in square wave patterns and the bending radius varies between $0\,\mu m$ (right angles) and $25\,\mu m$.

3.5 Propagation Loss

Section 2.4 presented data that showed that guided slab modes propagating in a film of silicon rich silicon nitride show good transmission in the $1480\,nm$ and $1580\,nm$ with a peak attenuation of signal occurring at about $1530\,nm$. This peak corresponds to the presence of $N-H$ bonds, and is diminished with proper annealing. These properties are important when making optical waveguides, but only represent one way in which optical signals are attenuated. Other mechanisms that can contribute to optical loss in waveguides include Raleigh scattering [35], which is caused by fluctuations in the refractive index; and irregularities at the interface between the core and cladding materials. Irregularities at the interface between the core and cladding are usually more pronounced on the sides of the waveguides that are defined by etching rather than on the surfaces defined by the deposition layers. The sidewalls of the waveguide tend to be rougher because they are defined through a lithographic process from a mask which has a certain inherent roughness, and the transfer of the pattern goes through exposure, development, and etching (all of which can contribute to sidewall roughness).

The primary interest here is the quantification of performance associ-

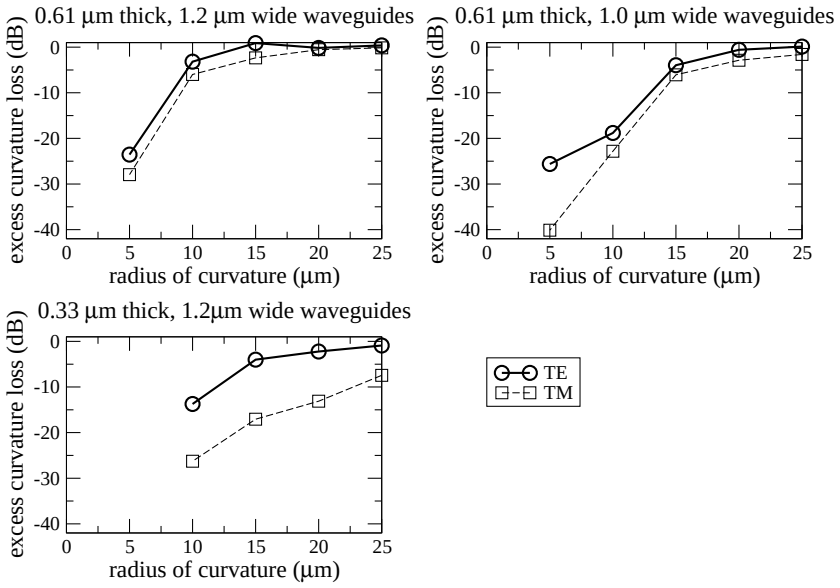

Figure 3.15: Waveguide bend loss measured for 24 right angle bends. Measurements shown represent a the excess insertion loss of the bent waveguides when compared to straight waveguides of similar length. The values should include pure bending loss and the transition loss caused by the modal difference between straight and curved waveguides. A linewidth reduction of $0.2 - 0.3\,\mu m$ was observed using an optical microscope.

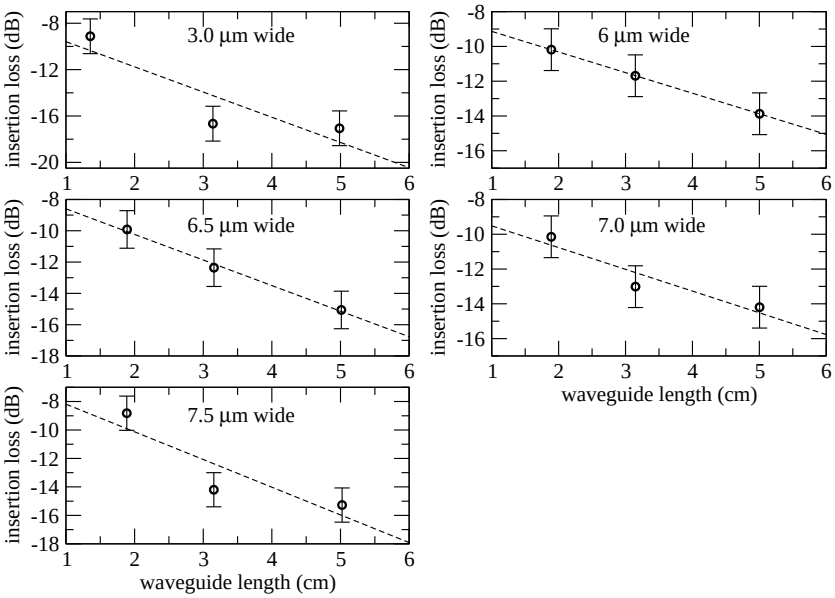

Figure 3.16: Propagation loss measurements using the "cut-back" method for waveguides fabricated with a $1.3\,\mu m$ thick film. Several waveguide widths are shown. The dimensions of the waveguides indicate they are multi-moded. The wavelength used for the measurements was $1550\,nm$.

ated with the waveguides and obtaining clues about the origin of loss in silicon rich silicon nitride optical waveguides. To this end multiple measurements were made. The typical process determining the optical loss of waveguides used the "cut-back" method. The "cut-back" method measures the insertion loss of an optical waveguide of a known length. The insertion loss is defined as the reduction in signal caused by inserting the waveguide between two fibers when compared to the signal transmitted through the fibers when they are coupled directly to each other. After recording the insertion loss, the waveguide is cleaved or diced (depending on the method that created the original facets of the sample) into unequal portions. The insertion loss of the remaining pieces is measured and recorded along with the lengths of the samples. The result is a record of insertion loss as a function of waveguide length. The reduction in signal associated with propagation loss is assumed to be proportional to the signal being transmitted (i.e. $dP = -\alpha P dx$ where P is the power, x is the waveguide length, and α is an attenuation constant taken to be real and positive for a medium displaying no gain) . The solution to this is an exponential expression, that, when represented in a semi-log plot, is becomes linear with a slope designated as $dB\,cm^{-1}$. The intercept of a the linear fit corresponds to the coupling loss of the waveguide, which can be thought of as the signal loss extrapolated to a waveguide of zero length.

An assumption of this method is that coupling between the waveguide and the fiber remains constant for a given waveguide that is being measured. This is not always a good assumption because small irregularities in the waveguide interface to high-index contrast waveguides can cause significant fluctuations in the coupled signal. In addition, the coupled signal is very sensitive to alignment and the signal coupled into the waveguide can have significant error introduced by small variations. The situation is not necessarily improved with automated alignment rather than human controlled alignment. The reason being that it is often the case that during the process of alignment, local minima can be encountered and physical contact between the waveguide and fiber can cause sudden variations in signal with the translation of the fiber with respect to the waveguide. Physical contact or near physical contact is necessary

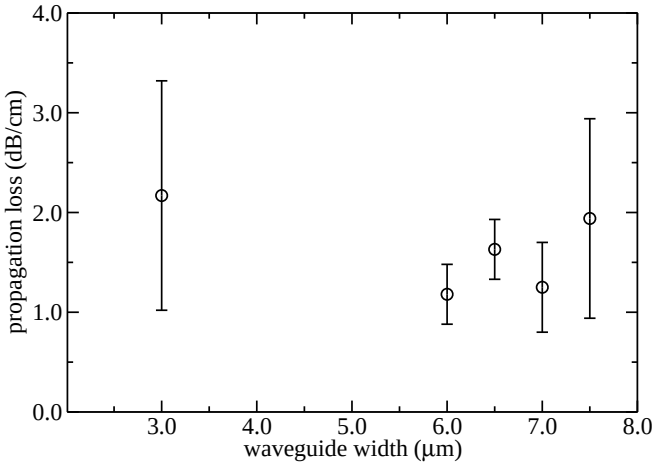

Figure 3.17: A summary of the propagation losses derived from figure 3.16.

to obtain sufficient coupling. Using a lensed fiber [47] is a possible solution to this problem that was not used during this research.

The equipment used for the measurements included a Melles Griot piezo-electric stages and controllers; high index contrast fiber having beam waist of $3\,\mu m$; index matching oil; polarization controllers; a tunable laser; and an optical spectrum analyzer.

Figure 3.16 shows cut-back measurements performed on a sample having waveguides of relatively large core dimensions. The thickness of the waveguides (i.e. the thickness of the silicon rich nitride film deposited to make the waveguides) was $1.3\,\mu m$. Several different waveguide widths, varying between $3\,\mu m$ and $7.5\,\mu m$ were measured. The wavelength used for the measurements was $1550\,nm$. These waveguide are well within the multimode regime and the propagation losses are generally not representative of losses in single mode waveguides. They do however represent what might be considered a best case scenario for optical loss since multimode waveguides tend to display lower attenuation.

The slopes of the lines in figure 3.16 are shown in figure 3.17 as a function of waveguide width. The results indicate that the propagation loss can generally be considered to lie between 1 and $2\,dB\,cm^{-1}$, though there are higher measurements of loss associated with the widest ($7.5\,\mu m$) and narrowest ($3\,\mu m$) waveguides. From these measurements there is not a clear variation of propagation loss with waveguide width. Losses for similar waveguide have been measured to be as low as $0.7\,dB\,cm^{-1}$ [27]. These measured losses did not distinguish between polarizations. The propagation loss of the waveguide generally above the propagation loss of the guided slab mode (figure 2.7). This is ideally expected, though it should be noted that variations in the efficiency with which light is coupled out of a slab mode might occur since the slab mode is only confined in one direction.

If the origins of optical loss in waveguides is scattering (either that arising from Raleigh scattering, or from side wall roughness) it is expected to have a wavelength dependence. Figure 3.18 shows an extreme case of wavelength dependent loss measured for the TE mode in a $0.33\,\mu m$ high $\times 1.2\,\mu m$ wide waveguide. The results show that the attenuation tends to decrease with the wavelength and agrees with the general behavior that might attributed to scattering. The slope of the fit line is $-5.4\,dB\,cm^{-1}\,\mu m^{-1}$[4]. This behavior is not generally seen though with more symmetric waveguides where the noise associated with the measurement generally exceeds any variation with wavelength in the wavelength range generally observed (between $1480\,nm$ and $1580\,nm$) with the available tunable laser source.

3.6 Effective Index: Grating

In the next chapter it will be shown that generally when looking at the response of optical filters like rings that have multiple resonances and relatively small spacings between the resonances (i.e. free spectral range), it is difficult to determine the effective index of the waveguide involved in the structure. Instead, the effective group index of a structure is de-

[4]This corresponds to a $\lambda^{-1.9}$ dependence.

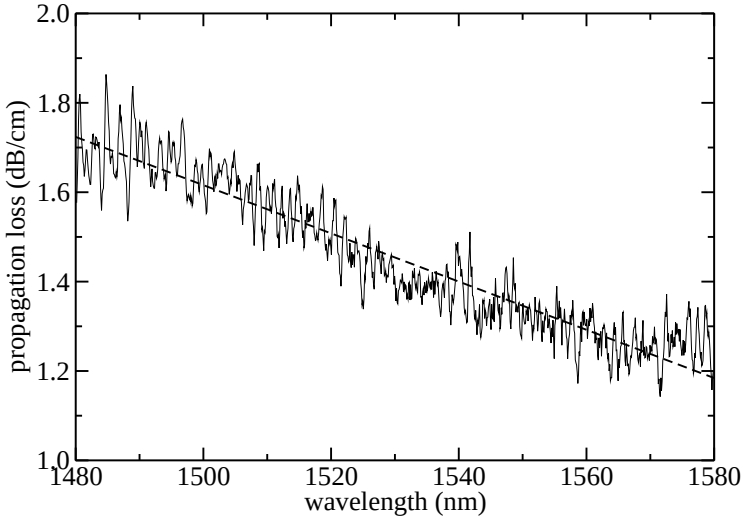

Figure 3.18: Measured propagation loss as a function of wavelength for a $0.33\,\mu m$ high waveguide with a width before linewidth reduction of $1.2\,\mu m$. The estimated linewidth reduction on this sample was $0.2 - 0.3\,\mu m$.

rived. An effective index can be derived from the effective group index by assuming simple waveguide geometries and likely variations, and determining what geometry corresponds to the effective group index. The effective index can then be determined assuming a similar geometry. This general method is however not direct and many factors can cause error. If the waveguide does not have the assumed structure (such as having a trapezoidal shape instead of a rectangular shape) or if the materials used have been altered during fabrication (e.g. diffusion could cause indistinct side walls or even alter the refractive index of the material), this method will inevitably yield the wrong result.

For this reason, a more direct measurement of the effective index was performed with UV written gratings. These gratings were written in a photosensitive cladding layer and the general method is covered in chapter 5.

3.7 Conclusion

This chapter has presented properties of high index waveguides from a fundamental basis, first concentrating on geometric effects on the nature of propagating modes, then demonstrating some of the capabilities of high-index contrast waveguides made with silicon rich silicon nitride cores.

Variation of waveguide geometry causes significant changes in propagating modes, but not as would be expected from SOI waveguides. Bending radii less than $25\,\mu m$ display low loss with a $1.2\,\mu m$ wide, $0.6\,\mu m$ thick, $1.2\,\mu m$ wide (before linewidth reduction) waveguide having losses indistinguishable from those of a straight waveguide when the bending radius is $20\,\mu m$ or more. The propagation losses are between $1\,dB\,cm^{-1}$ and $2\,dB\,cm^{-1}$ (though this can fluctuate significantly with processing).

The fabrication techniques have been proved to produce high quality waveguides while maintaining processing techniques that are applicable for larger scale production (when compared to e-beam lithography).

Chapter 4

Ring Resonators and Filters

4.1 Introduction

High-index contrast waveguides, beyond just increasing the packing density of integrated optical devices, allow for complex optical filters based on ring resonator structures. The fundamental concept of the ring resonator is not new. Ring resonators had already been proposed for optical waveguides as early as 1969 [3], if not before. What makes ring resonators so attractive is that they are simple in structure and function, and ideally non-reflective. Other structures can be, and are, used as optical resonators - for instance simple Fabry-Perot cavities and gratings, but these structures usually produce reflections. If a grating is used for an add drop filter, it is usually used in conjunction with an optical circulator [48] or a Mach-Zehnder interferometer [49] so reflections can be extracted. Under certain conditions cascaded optical resonators other than rings can be used for channel add-drop filters [50], but these are not as simple and arguably not as elegant as the ring resonator.

Not only can ring resonators be used as filters by themselves, but they can also be used as the basis for more complex optical filtering systems. Ring resonators are known as autoregressive (AR)[1] filters and when they are used in conjunction with moving average (MA) filters (e.g.

[1] Autoregressive means that the performance of the ring relies upon previous states. It is a feedback system.

Mach-Zehnder interferometers) they can be used to make flexible filtering systems. A system that uses both AR and MA filter components is known as an ARMA filter [13].

Ring resonators can be made with many different waveguides. Low-index contrast waveguides, like those relying on germanium doping of silica, can be used to make ring resonators. The problem is that if the bending radius is large the free spectral range tends to be small. High-index contrast waveguides, as has been shown, solve this problem and allow for tight bending radii (in the case of silicon rich silicon nitride, bending radii of less than $25\,\mu m$ are possible). This makes a large free spectral range (FSR), spanning several if not 10's of nanometers, possible. This offers flexibility for practical and complex filter design.

4.2 Free Spectral Range

The condition for resonance for an optical ring resonator is simple and without considering the details of the ring, an expression for the free spectral range (FSR) can be derived. The resonance condition of the ring can be defined as the situation in which the optical distance around the ring (defined as the product of the effective index of the waveguide and the physical length round the ring) equals an integer multiple of the of the vacuum wavelength:

$$n_{eff}(\lambda)L = N\lambda \tag{4.1}$$

Where n_{eff} is the effective index of the waveguide which is generally taken to be a function of wavelength; L is the physical length around the ring; N is an integer; and λ is the wavelength. Proceeding in a mathematically diligent way [2] and considering two resonances corresponding to $N = j$ and $N = j + 1$ where j is an integer, two resonant conditions can be expressed:

[2] a simpler method of deriving an expression for the FSR is available if equation 4.1 is differentiated w.r.t. λ and N.

$$j = \frac{n_{eff}(\lambda_1)L}{\lambda_1} \tag{4.2}$$

$$j+1 = \frac{n_{eff}(\lambda_2)L}{\lambda_2} \tag{4.3}$$

where λ_1 and λ_2 are two adjacent resonances in the wavelength domain. The spacing between these resonances is the free spectral range. Subtracting equation 4.2 from equation 4.3, the following is obtained:

$$1 = \frac{\lambda_1 n_{eff}(\lambda_2)L - \lambda_2 n_{eff}(\lambda_1)L}{\lambda_1\lambda_2} \tag{4.4}$$

If it is assumed that the effective index can accurately be expressed with a two term Taylor expansion about one of the resonances, $n_{eff}(\lambda) \approx n_{eff}(\lambda_1) + \frac{\partial n_{eff}}{\partial\lambda} \mid_{\lambda=\lambda_1} (\lambda - \lambda_1)$. Some algebraic manipulation leads to the equation:

$$\lambda_1\lambda_2 = \left(n(\lambda_1) - \lambda_1 \frac{\partial n_{eff}}{\partial\lambda} \mid_{\lambda=\lambda_1}\right)(\lambda_1 - \lambda_2)L \tag{4.5}$$

Where the term $\left(n(\lambda_1) - \lambda_1 \frac{\partial n_{eff}}{\partial\lambda} \mid_{\lambda=\lambda_1}\right)$ is effective group index, $n_g(\lambda_1)$, at λ_1. More manipulation yields:

$$\lambda_1 - \lambda_2 = \frac{\lambda_1\lambda_2}{n_g(\lambda_1)L} \tag{4.6}$$

The final step in obtaining an expression for the FSR is to assume that the spectral separation between the wavelengths, λ_1 and λ_2, is small when compared to the wavelengths themselves. This is equivalent to assuming that N is large.

$$\Delta\lambda = \lambda_1 - \lambda_2 \tag{4.7}$$

$$= \frac{\lambda_1^2 + \lambda_1\Delta\lambda}{n_g(\lambda_1)L} \tag{4.8}$$

$$= \frac{\lambda_1^2}{n_g(\lambda_1)L\left(1 - \frac{1}{N}\right)} \tag{4.9}$$

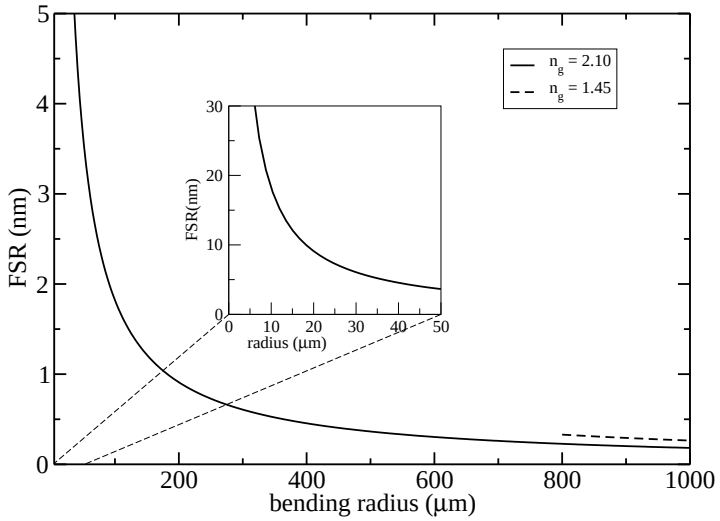

Figure 4.1: The FSR as a function of ring radius for a circular ring resonator. Two effective group indexes have been used to calculate the FSR: $n_g \approx 2.10$ which is typical of one of the high-index contrast devices studied; and $n_g \approx 1.45$ which is typical of a standard low-index contrast waveguide. The low index contrast waveguide is not capable of making bends in the sub-mm region and is shown to emphasize the role of the effective group index. The wavelength used for this calculation was 1550nm.

where the resonance relationship, equation 4.1, has been invoked. When the term N is assumed to be large, and the effective group index is assumed not to change significantly between the resonant wavelengths being considered. The FSR is then given by:

$$FSR = |\lambda_1 - \lambda_2| = \frac{\lambda^2}{n_g L} \tag{4.10}$$

Where λ is the approximate vacuum wavelength under consideration and n_g is the effective group index at this wavelength. The FSR is therefore inversely proportional to the length around the ring or, more succinctly, the optical group distance around the ring. A simple graph of the relationship between FSR and bending radius is in figure 4.1, and it shows that for typical values of the effective group index, that a bending radius of less than $50\,\mu m$ is required to obtain a FSR greater than $5\,nm$. This emphasizes the need for high-index contrast waveguides when making useful ring resonator based devices.

The free spectral range may also be written in terms of the frequency (f) by noting the relationship $f = \frac{c}{\lambda}$ and its derivative, $df = -\frac{c}{\lambda^2} d\lambda$:

$$FSR_{freq} = \frac{c}{n_g L} \tag{4.11}$$

4.3 Simple Ring Resonator Model

The next step necessary to describe ring resonators is modeling the response of a single straight waveguide coupled to a single ring resonator (shown in figure 4.2). This configuration can be used for a notch filter [51] or a dispersion compensating device [52]. These will be discussed later and for now the general response of the ring is considered. The first assumption that will be made is that the coupling between the waveguide and the ring is perfectly lossless and that the transfer matrix associated with it is given by:

$$\begin{pmatrix} A_o \\ B_o \end{pmatrix} = \begin{pmatrix} x & -i(1-x^2)^{1/2} \\ -i(1-x^2)^{1/2} & x \end{pmatrix} \begin{pmatrix} A_i \\ B_i \end{pmatrix} \tag{4.12}$$

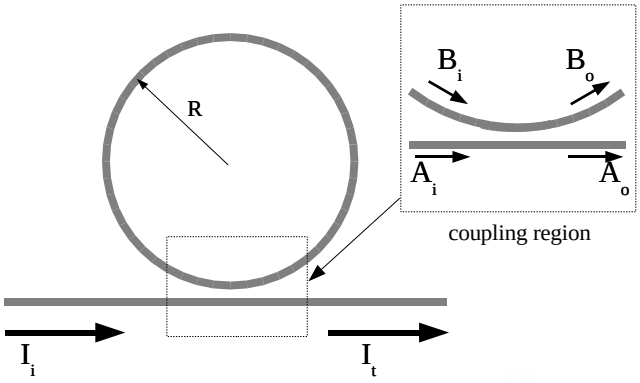

Figure 4.2: A schematic picture of a simple ring resonator coupled to one straight waveguide. An expanded view of the coupler region is given.

Where A_o, B_o, A_i, and B_i are the outputs and the inputs, respectively, of a directional coupler corresponding to the complex field amplitudes of the guided modes (shown int figure 4.2). The general relationship in equation 4.12 is obtained from coupled mode theory where x is a cosine term expressed as $cos(\kappa z)$, in which κ is a coupling constant and z is the length of the coupler [13]. For the purpose of clarity and simplicity of the model, the coupling is assumed to happen over an infinitesimal length when compared with the total length of the ring.

The general procedure for finding the transfer function of the ring is to sum all possible optical paths from the input, I_i, to the output, I_t. Straight transmission through the coupler is given by: $I_i x$. There is also a contribution of the light circulating once around the ring given by : $-i(1-x^2)^{1/2}e^{-\beta L}y(-i(1-x^2)^{1/2}$ or $-(1-x^2)ye^{-i\beta L}$ where L is the distance around the ring, β is the propagation constant associated with the waveguide and y is fractional transmission of field amplitude around the ring. Other terms corresponding to more circulations around the ring are also added to obtain an infinite sum:

$$\begin{aligned} I_t &= I_i\Big(x-(1-x^2)ye^{-i\beta L}-(1-x^2)xy^2e^{-i2\beta L}- \\ &\quad (1-x^2)x^2y^3e^{-i3\beta L}-\ldots) \qquad (4.13) \\ &= I_i\left(x-\frac{1-x^2}{x}\sum_{n=1}^{\infty}\left(xye^{-\beta L}\right)^n\right) \qquad (4.14) \end{aligned}$$

The summation shown is in the form of a geometric series. The constants, x and y, are both of a magnitude less than unity and therefore the sum is convergent [53]. The transmitted signal can then be written as[3]:

$$I_t = I_i(x-(1-x^2))\frac{ye^{-i\beta L}}{1-xye^{-i\beta L}} \qquad (4.15)$$

[3] noting that :

$$\sum_{n=1}^{\infty}\rho^n = \lim_{n\to\infty}\frac{\rho-\rho^{n+1}}{1-\rho}$$

$$= I_i \frac{x - ye^{-i\beta L}}{1 - xye^{-i\beta L}} \tag{4.16}$$

This is the complex, steady-state, response of a ring resonator and represents the phase and magnitude transmission of the fields in a waveguide that is coupled to a single resonator. The transmitted power can be extracted from this and is given by:

$$I_t^* I_t = I_i^* I_i \frac{x^2 + y^2 - 2xy\frac{e^{i\beta L} + e^{-i\beta L}}{2}}{1 - 2xy\frac{e^{i\beta L} + e^{-i\beta L}}{2} + x^2y^2} \tag{4.17}$$

$$= I_i^* I_i \frac{x^2 + y^2 - 2xy\cos(\beta L)}{1 + x^2y^2 - 2xy\cos(\beta L)} \tag{4.18}$$

$$= I_i^* I_i \left(1 - \frac{(x^2 - 1)(y^2 - 1)}{1 + x^2y^2 - \cos(\beta L)}\right) \tag{4.19}$$

Using the identity $\cos(\beta L) = 1 - 2\sin^2\left(\frac{\beta L}{2}\right)$ equation 4.19 can be re written as [36]:

$$I_t^* I_t = I_i^* I_i \left(1 - \frac{(x^2 - 1)(y^2 - 1)}{(1 - xy)^2 + 4xy\sin^2(\frac{\beta L}{2})}\right) \tag{4.20}$$

This equation should be consistent with the FSR we obtained from simple consideration of the resonant conditions, equation 4.10. To show this, β is rewritten in terms of the vacuum wavelength, λ, and the effective index, n_{eff}. Then n_{eff} is expanded with respect to the wavelength (and it is noted that whenever n_{eff} is referred to that it is generally a function of the wavelength).

$$\beta = \frac{2\pi}{\lambda} n_{eff} \approx \frac{2\pi}{\lambda}\left(n_{eff}|_{\lambda=\lambda_c} + \frac{\partial n_{eff}}{\partial \lambda}|_{\lambda=\lambda_c}(\lambda - \lambda_c)\right) \tag{4.21}$$

Where λ_c is the center wavelength about which the Taylor series is expanded. Multiplying through, the following equation is derived:

$$\beta \approx \left(n_{eff} - \frac{\partial n_{eff}}{\partial \lambda}|_{\lambda=\lambda_c}\lambda_c\right)\frac{2\pi}{\lambda} + 2\pi\frac{\partial n_{eff}}{\partial \lambda}|_{\lambda=\lambda_c} \quad (4.22)$$

$$\approx \frac{2\pi n_g}{\lambda} + \Phi \quad (4.23)$$

Where Φ is a constant given by $\Phi = 2\pi\frac{\partial n_{eff}}{\partial \lambda}|_{\lambda=\lambda_c}$.

Examining equations 4.23 and 4.20 and noting that a change in the trigonometric function[4] of π corresponds to moving to the next resonance, we can deduce the change in wavelength as:

$$d\left(\frac{\pi n_g L}{\lambda}\right) = -\frac{\pi n_g L}{\lambda^2}d\lambda = \pi \quad (4.24)$$

Which is what is expected for the FSR, namely, $FSR = |d\lambda| = \frac{\lambda^2}{n_g L}$. This is the same as equation 4.10.

4.3.1 Properties of Resonance

Resonant absorption in physical systems often have a Lorentzian profile[5] . The ring resonator is no different and the basic properties of can be gleaned from the equations presented above. For a more detailed look that is useful when dealing with experimental data, a model that corresponds to a Lorentzian for a single resonance will be described. This is an approximation that is valid for rings having resonances that are well separated[6]. First, the expression for the propagation constant given in equation 4.23 is inserted into equation 4.20. The normalized response of the ring, $T(\lambda) = \frac{I_t^* I_t}{I_i^* I_i}$, is considered to lighten the notation and consider the ring response more directly.

[4] note the trigonometric term is $\sin^2$.

[5] A driven, damped simple harmonic oscillator has a Lorentzian response and is used to describe a wide variety of physical phenomena – from idealized shock absorbers on a car to atomic absorption

[6] "well separated" resonances is a loosely defined term, but may be roughly thought of as the situation in which the full width half maximum of the amplitude transmission is small compared to the free spectral range: $FWHM << FSR$. In other words, resonances are well separated when the finesse is "high".

$$T(\lambda) = 1 - \frac{(x^2-1)(y^2-1)}{(1-xy)^2 + 4xy\sin^2(\frac{\pi n_g L}{\lambda} + \phi)} \tag{4.25}$$

Where $\phi = \Phi L$ is a constant and represents a shift in the wavelength of the resonances. To approximate an expression for a single isolated resonance, the trigonometric term is expanded about a resonant wavelength which corresponds to $\sin^2(\frac{\pi n_g L}{\lambda_{res}} + \phi) = 0$. Proceeding with this, $\sin^2(\frac{\pi n_g L}{\lambda} + \phi) \approx \frac{\pi^2 n_g^2 L^2}{\lambda_{res}^4}\Delta\lambda^2$. Where $\Delta\lambda = (\lambda - \lambda_{res})$. Substituting into equation 4.25 we get:

$$T(\lambda) \approx 1 - \frac{(x^2-1)(y^2-1)}{(1-xy)^2 + 4xy\frac{\pi^2 n_g^2 L^2}{\lambda_{res}^4}\Delta\lambda^2} \tag{4.26}$$

Around a resonant wavelength, λ_{res}, and for separated resonances. This second term in the equation is in the form of a Lorentzian and can be readily compared to the standard form in any number of mathematical reference books [54]. This form is of practical value because fitting individual peaks of recorded spectra, allows the free spectral range, FSR, to be derived. If the length around the ring, L, is known, then the effective group index is quickly extracted from equation 4.10. The fitting process that proceeds in this way is much friendlier and more likely successful than one that attempts to fit equation 4.25 directly. The reason for this is the positions of the resonances shift and the possibility of being "caught" in a local minima while executing a fitting routine when fitting equation 4.25 directly.

If equation 4.26 is compared to a standard form of the Lorentzian function [55], the full width at half maximum (FWHM) of the Lorentzian term in the single resonance expression for well separated resonances is given by:

$$FWHM = \frac{\lambda_{res}^2}{\pi n_g L}\frac{1-xy}{\sqrt{xy}} = FSR\frac{\pi n_g L}{\pi\sqrt{xy}} \tag{4.27}$$

As is shown, this is easily expressed in terms of the free spectral range (FSR) and immediately suggests that the finesse of the resonator

can be calculated. We define the finesse,F, of a resonator as $F = \frac{FSR}{FWHM}$. Following from equation 4.27, the finesse is [36]:

$$F = \frac{\pi\sqrt{xy}}{1-xy} \tag{4.28}$$

Some caution should be exercised when applying these formulas. Equation 4.27 was derived from a single resonance approximation and in the case that resonances are not well separated, the FWHM will inevitably deviate from the predicted value. For resonances that are not well separated, a strictly more appropriate expression can be derived:

$$FWHM_m = \frac{\sqrt{2}\lambda_{res}^2}{\pi n_g L}\frac{1-xy}{\sqrt{x^2y^2+1}} \tag{4.29}$$

Where the subscript m is used to denote that this is the expression of the width of the resonance half way between the maximum transmission and the minimum transmission. In the limit as $(xy-1)^2$ goes to zero, equation 4.29 approaches equation 4.27. Which in physical terms says that a high quality resonator approaches the Lorentzian approximation.

The maximum and minimum transmission of a waveguide coupled to a single ring resonator is also of interest. These can be extracted from equation 4.20 by setting the sinusoidal term to 0 (for the minimum) and 1 (for the maximum). Doing this we obtain [36]:

$$T_{min} = \frac{(x-y)^2}{(1-xy)^2} \tag{4.30}$$

$$T_{max} = \frac{(x+y)^2}{(1+xy)^2} \tag{4.31}$$

Where T_{min} is the minimum normalized transmission and T_{max} is the maximum normalized transmission. The immediate consequence of equation 4.30 is that T_{min} goes to zero when $x = y$. This means that an essential criterion for 100 % extinction of the transmitted signal is a balance between loss for signal propagating around the ring and coupling into (and out of) the ring.

An expression for the quality factor, Q, is also easily obtained:

$$Q = \frac{\lambda_{res}}{FWHM} = \frac{\pi n_g L}{\lambda_{res}} \frac{\sqrt{xy}}{1 - xy} \tag{4.32}$$

4.3.2 Positioning of Resonances

One design parameter that is essential for making practical optical filters is the spectral position of a ring's resonance. The calculation of this is straight forward given the resonant condition in equation 4.1, and how this relates to processing tolerances when making rings is also straight forward by differentiating the resonant condition. The change in the resonance as a function of effective refractive index and the length of the ring is of interest.

$$dn_{eff}(\lambda_i) + \frac{\partial n_{eff}}{\partial \lambda}|_{\lambda=\lambda_i} d\lambda = \frac{N}{L} d\lambda - \frac{N\lambda}{L^2} dL \tag{4.33}$$

Where λ_i is a fixed wavelength associated with the initial spectral position of resonance and $dn_{eff}(\lambda_i)$ is the change in effective index at the initial wavelength, λ_i. $dn_{eff}(\lambda_i)$ can be caused by thermal tuning or non-linear optical responses when waveguide are subjected to a strong electric field. With some algebraic manipulation and using equation 4.1 to remove the dependence on N, this becomes:

$$d\lambda = \frac{\lambda}{n_g} dn_{eff}(\lambda_i) + \frac{n_{eff}}{n_g L} dL \tag{4.34}$$

The implications of this equation are far reaching and fundamental to ring resonator devices. If identical ring resonators are used to make a filter and it is necessary that they share the same resonance, then a tolerance for the uniformity of the refractive index of a film is suggested from the acceptable variation in the effective index of the waveguide. It is also apparent that variations in the photolithography or etching process can have devastating effects - especially given the geometric sensitivity of the effective index of high-index contrast waveguides to cross-sectional geometry. A typical waveguide with a effective group index of approximately 2.0 ($n_g \approx 2.0$), and a resonant wavelength of 1550nm ($\lambda = 1550nm$) requires a variation of effective index of no more than about 1.3×10^{-3}

to maintain a give resonance within a $1nm$ range. A typical variation of effective refractive index for a $0.6\,\mu m$ thick high index waveguide as a function of waveguide width is about $3 \times 10^{-4} nm^{-1}$ for the TE polarization and $5 \times 10^{-4} nm^{-1}$ (see equations 3.16) for the TM polarization. This means that waveguide variation can be no more than about $5nm$ for the TE polarization ($3nm$ for the TM polarization) before having significant effects.

These are, of course, incredibly tight tolerances that have little chance of being achieved without significant improvements to fabrication technology. A line width reduction of between $0.2\,\mu m$ and $0.3\,\mu m$ for fabricating these waveguides may be admirable by some measures, but not in terms of the tolerances necessary for repeatable, finely tuned devices. The practical effect is that devices based on high-index contrast waveguides require some method of fine tuning the optical distance around the ring. The most obvious candidate is thermal control though others, such as those that rely on optical nonlinearities, are also potentially attractive.

The terms in equation 4.34 are useful in a number of situations beyond those associated with tolerances. If it assumed that the length around the ring is constant, as is generally the case for any given ring, the first term can be used to derive a simple expression relating wavelength shifts to shifts in the effective index:

$$\frac{\Delta\lambda}{\lambda} = \frac{\Delta n_{eff}}{n_g} \tag{4.35}$$

If a filter requires staggered resonances with multiple rings, the second term in equation 4.34 can give an indication of what variation in ring length is needed to give a desired wavelength shift. This might be useful in designing a multi-channel add-drop filter, but tolerances remain a nuisance.

4.4 Phase Response

To this point the emphasis has been on the amplitude response of a ring coupled to a waveguide. This is only part of the story. The response of the ring is generally complex and as such has both an amplitude response and

a phase response. The amplitude response provides useful functions that might be applied to wavelength selective filters, but the phase response can be critical in high speed systems where dispersion management is an important part of maintaining signal integrity [56].

Ring resonators are inherently dispersive. A high quality resonant cavity will, by definition, have a long decay time, so that the resonator has a certain memory and can cause delays of signal, especially at resonance. The group delay is obtained by the general amplitude response function in equation 4.16. We are generally concerned in the equivalent delay the phase response at a certain wavelength represents. Assuming the response function has the form:

$$I_t = A(\lambda)e^{i\phi} \tag{4.36}$$

Where $A(\lambda)$ is the amplitude response, and ϕ is the phase (or argument). Drawing an analogy with the exponential form, $e^{i\omega t}$, the equivalent time response can be derived:

$$\Delta t = \frac{\partial}{\partial\omega}\phi \tag{4.37}$$

$$= \frac{-\lambda^2}{2\pi c}\frac{\partial}{\partial\lambda}\phi \tag{4.38}$$

where Δt is the group delay, c is the speed of light in a vacuum, ω is the angular frequency, and the relationship $\omega = 2\pi\frac{c}{\lambda}$ has been used.

Applying this to equation 4.16, and noting that the derivative of the *arctangent* is given by: $\frac{\partial}{\partial x}\arctan(x) = \frac{1}{1+x^2}$, an expression for the group delay of a single ring coupled to a waveguide can be obtained.

One of the most interesting characteristics is that under ideal circumstances, when a single ring is coupled to a waveguide, and there is no loss in the ring (i.e. $y = 1$), the waveguide shows no amplitude modulation. This is expected from power conservation - with no attenuation, what goes in must come out. There can however be significant phase response, and group delay. In figure 4.3, the group delay of a lossless ring coupled to a single waveguide is shown. The group delay peaks on resonance, where the ring is a high quality resonator with a significant decay time.

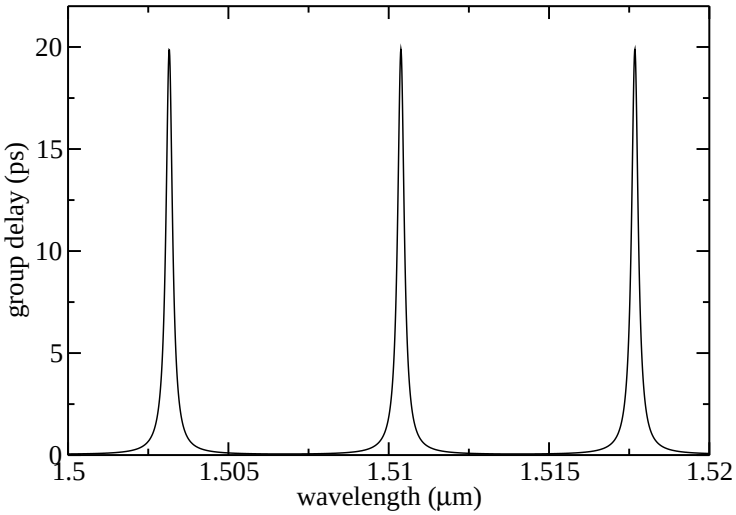

Figure 4.3: Calculated group delay for a signal transmitted on a waveguide coupled to a single ring resonator with the following parameters: $n_g = 2.0$, $x = 0.9$, $y = 1.0$, $raidus = 25\,\mu m$.

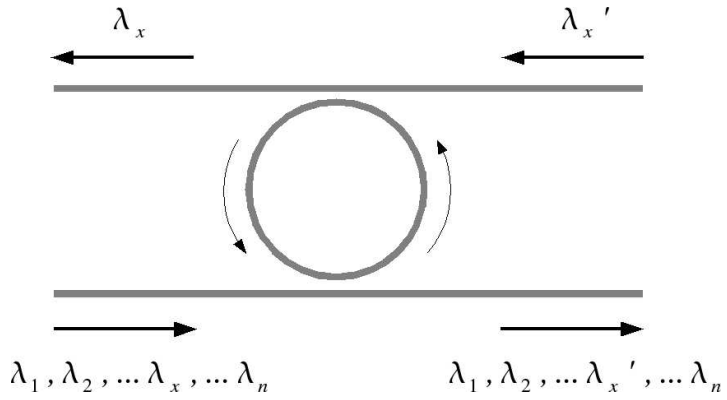

Figure 4.4: A simple schematic of a single ring add-drop filter

Using this general effect, cascaded rings can be used to make very flexible dispersion compensation filters [57]. In addition, high quality resonators can be cascaded on a waveguide to make the group delay very long and thus form "slow" waveguides [58]. This presents interesting possibilities for non-linear devices, but practical application generally requires extremely low-loss waveguides. This can be difficult to realize.

The phase responses of rings were not the focus of the studies in this thesis, they do however represent an important part of ring based filters.

4.5 Add-Drop Filter

The most simple ring-based filter that can be made to extract and re-route specific wavelengths is the single ring add-drop filter shown in figure 4.4. The basic configuration involves two waveguides, sometimes referred to as signal buses, coupled to a single ring. Resonance of the ring facilitates coupling between the waveguides, allowing for discrete wavelengths to be extracted.

The amplitude response of an add-drop filter can be derived by inspection of equation 4.25. It is noted that the definition of y refers to the "round-trip" amplitude loss of the field coupled into the ring. In the configuration shown for the add-drop filter, this can be represented in two

parts: loss associated with propagation around the ring as in the case of a single waveguide being coupled to the ring and "loss" associated with coupling into the second waveguide. For the simple add-drop filter, the y term can then be rewritten as a product of the ring loss, y and the transmission of the second coupler, x_2. The resulting equation for the transmission of one waveguide is:

$$T(\lambda) = 1 - \frac{(x^2-1)(y^2x_2^2-1)}{(1-xx_2y)^2 + 4xx_2y\sin^2(\frac{\pi n_g L}{\lambda_o} + \phi)} \tag{4.39}$$

where x describes the coupling of the waveguide to the ring, x_2 describes the coupling of the ring to the other waveguide, and y, as before, describes the ring loss caused by propagation around the ring. If y is set to 1, corresponding to a completely lossless ring, T_{min} can be zero if x and x_2 are equal. In other words, in the case of an ideal lossless ring, all the transmitted power at a wavelength of resonance can be extracted. Since there is no loss associated with the ring, this power must be passed to the second waveguide. It is in this case that a true "add-drop" filter can be realized because full power can be extracted, redirected, and replaced in one simple device. As a practical matter, this is very difficult to realize. A lossless ring is an idealization, and achieving exact balance of the couplings can be problematic. This is especially true with high-index contrast waveguides in which processing tolerances are tight and the coupling must be achieved in a short coupling length (a few to 10's of microns) to take advantage of the special properties that make high-index contrast waveguides useful.

An expression for the extracted signal that is coupled to another waveguide must derived in the non-ideal case. This can be done in much the same way as was demonstrated for the single ring - i.e. summing all the possible optical paths that can be taken between the input and output. Carrying through on this basic plan, the following expression is obtained:

$$D(\lambda) = \frac{(1-x^2)(1-x_2^2)y}{(1-yxx_2)^2 + 4yxx_2\sin^2(\frac{\pi n_g L}{\lambda} + \phi)} \tag{4.40}$$

Where $D(\lambda)$ is the normalized dropped signal as a function of wavelength. An example of the calculated response of a one-ring add-drop

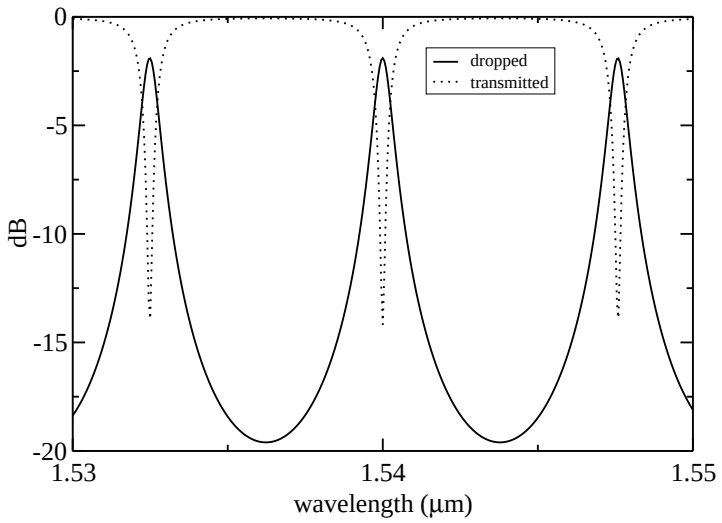

Figure 4.5: The calculated transmitted and dropped signals for a single ring add-drop filter. The values assumed for this graph were $x = 0.9$, $x_2 = 0.9$, $y = 0.95$, $n_g = 2.0$, and $L = 2\pi\,25\,\mu m$.

filter can be seen in figure 4.5.

Some useful quantities associated to be noted for the dropped signal $D(\lambda)$ are the maximum transmission, D_{max}:

$$D_{max} = \frac{(1-x^2)(1-x_2^2)y}{(1-xx_2y)^2} \tag{4.41}$$

and the full width half maximum value, D_{fwhm}:

$$D_{fwhm} = \frac{\lambda_{res}^2(1-xx_2y)}{\pi n_g L\sqrt{xx_2y}} \tag{4.42}$$

These expressions is instructive for the design of filters. If the equation for D_{max} (equation 4.41) is examined, it clearly indicates that when y is equal to unity and $x = x_2$, all of the power is coupled into the dropped signal at the resonant wavelength. Beyond this, if D_{max} is differentiated with respect to y, and it is again assumed that $x = x_2$, then the derivative of D_{max} with respect to y, when y is set to unity is given by:

$$\frac{d}{dy}D_{max} = \frac{(1+x^2)}{(1-x^2)} \tag{4.43}$$

What equation 4.43 indicates is that less sensitivity to ring loss in a simple add-drop filter is achieved by decreasing the value x. This corresponds to having a greater power fraction coupled in and out of the ring at the couplers. The result is intuitive and must be used with equation 4.42 when designing filters because as x decreases, the full width at half maximum tends to increase.

In the case of a single ring coupled to a single waveguide, the transmitted spectrum can be measured and fit to the x and y parameters. In that case, the parameters are symmetric and there is no experimental method to distinguish them from one another. This means that the results of fitting remain ambiguous. When measuring an add-drop filter, there are four possible measurements: the transmitted signals for each waveguide (i.e. the roles of the waveguides in figure 4.4 are reversed); and the dropped signals associated with the each waveguides. As a result, fitting of spectra can proceed and potentially give unambiguous measurements of the ring properties.

4.6 Coupling in Time

Dealing with the response of several rings coupled together can be cumbersome when attempting to sum all the possible optical paths as was done in the case of a single ring. One level of abstraction that is useful is considering the rings as resonators coupled in time. This section follows the conventions in reference [15] and relates them to the model discussed above.

We start by considering a single ring coupled to a single straight waveguide. First, the total energy of the resonator is defined as $|h(t)|^2$ and this is related to the power density, $|H(t)|^2$, in the ring by:

$$|h(t)|^2 = |H(t)|^2 \frac{L}{v_g} \tag{4.44}$$

Where L is the length around the ring and v_g is the group velocity. This assumes that the amplitude is constant around the ring. A quantity A_i is taken to be the amplitude of the incident guided mode in the straight waveguide, and A is the transmitted amplitude. It is assumed that the resonator has a known resonance frequency, ω_o and that there is a time constant, τ, that corresponds to the amplitude ($h(t)$) decay time of the ring. The time constant can be divided into constituent parts with the relationship:

$$\frac{1}{\tau} = \frac{1}{\tau_e} + \frac{1}{\tau_l} \tag{4.45}$$

where τ_e is the decay constant associated with power lost through the coupling to the straight waveguide, and τ_l is has its origin in the loss caused by propagation around the ring (e.g. bending loss, scattering loss, or material effects). Since we have assumed that we know the resonant wavelength, a differential equation for $h(t)$ can be written by inspection:

$$\frac{d}{dt}h(t) = (i\omega_o - \frac{1}{\tau})h(t) - i\mu A_i(t) \tag{4.46}$$

where μ is a coupling factor between the waveguide and the ring and $-i$ is chosen as a phase factor to make the analysis analogous to the previous analysis of ring resonators.

The output amplitude, $A(t)$, is given by:

$$A(t) = A_i(t) - i\mu h(t) \tag{4.47}$$

This assumes that the incident amplitude is not greatly affected by the loss it experiences from the power lost in to the coupler (i.e. x is close to 1). This assumption is reasonable for high-quality resonators.

The term μ is related to the decay constant τ_e. This is determined by considering a lossless ring ($\frac{1}{\tau_l} = 0$) with not driving amplitude $A(t)$. The solution to this, using equation 4.46, is given by:

$$h(t) = h_o e^{i\omega_o t - \frac{t}{\tau_e}} \tag{4.48}$$

where h_o defines the initial excitation of the resonator. The ring energy as a function of time is given by:

$$h^*(t)h(t) = |h_o|^2 e^{-2\frac{t}{\tau_e}} \tag{4.49}$$

This means the transmitted wave power, from equation 4.47, is given by:

$$|A(t)|^2 = \mu^2 |h(t)|^2 e^{-2\frac{t}{\tau_e}} = \mu^2 |h(t)|^2 \tag{4.50}$$

where $|A(t)|^2$, in this case, is the power leaving the ring and $|h(t)|^2$ is the bulk energy f the ring. From conservation of energy, it is known that:

$$\frac{d}{dt}|h(t)|^2 = -|A(t)|^2 = -\frac{2}{\tau_e}|h(t)|^2 \tag{4.51}$$

from this, it is apparent that $\mu^2 = \frac{2}{\tau_e}$. With this definition, the general solution of the resonator equation 4.46, can be derived (using an integrating factor):

$$h(t) = -i\sqrt{\frac{2}{\tau_e}} e^{(i\omega_o - \frac{1}{\tau})t} \int A_i(t) e^{-(i\omega_o - \frac{1}{\tau})t} dt + Ce^{(i\omega_o - \frac{1}{\tau})t} \tag{4.52}$$

where the first term represents the resonators response to a driving amplitude, $A_i(t)$, and the second term describes the decay of the ring

as a result of any initial excitation. C is a constant determined by the initial conditions. Assuming $C = 0$ (i.e. corresponding to there being no energy in the resonator apart from that stimulated by $A_i(t)$) and that $A_i(t) = Be^{i\omega t}$, we get the following expression for the resonator's frequency response:

$$h(t) = \frac{-i\sqrt{\frac{2}{\tau_e}}}{i\left(\omega - \omega_o\right) + \frac{1}{\tau}} A_t(t) \tag{4.53}$$

recalling equation 4.47:

$$\begin{aligned} A(t) &= A_i(t) - i\mu h(t) && (4.54)\\ &= \frac{i\left(\omega - \omega_o\right) + \frac{1}{\tau} - \frac{2}{\tau_e}}{i\left(\omega - \omega_o\right) + \frac{1}{\tau}} && (4.55) \end{aligned}$$

The power transmission of the waveguide coupled to the ring can then be determined:

$$A(t)^* A(t) = \frac{\left(\omega - \omega_o\right)^2 + \left(\frac{1}{\tau} - \frac{2}{\tau_e}\right)^2}{\left(\omega - \omega_o\right)^2 + \left(\frac{1}{\tau}\right)^2} A_i^*(t) A_i(t) \tag{4.56}$$

or:

$$\frac{|A|^2}{|A_i|^2} = 1 - \frac{\frac{4}{\tau_e \tau_l}}{\left(\omega - \omega_o\right)^2 - \left(\frac{1}{\tau_e} + \frac{1}{\tau_l}\right)^2} \tag{4.57}$$

This expression can be related to the expression derived for a single resonance of a ring (equation 4.26). To do this, we first equate the loss of the ring to the normalized parameter y by noting the following relationships:

$$\begin{aligned} \frac{2}{\tau} &= -\frac{\frac{d(h^* h)}{dt}}{h^* h} && (4.58)\\ y^2 &\approx 1 - \frac{\frac{d(h^* h)}{ds}\Delta s}{(h^* h)} && (4.59) \end{aligned}$$

Where Δs is set to the length of the ring and $ds/dt = c/n_g$.

$$\frac{1-y^2}{\Delta s}\frac{ds}{dt} \approx \frac{2}{\tau_l} \tag{4.60}$$

$$\frac{(1-y^2)c}{2\,n_g L} \approx \frac{1}{\tau_l} \tag{4.61}$$

in a similar way, x can be related to τ_e:

$$\frac{(1-x^2)c}{2\,n_g L} \approx \frac{1}{\tau_e} \tag{4.62}$$

where it is assumed that the resonator has a high quality. Substituting these relationships into equation 4.57, the following equation can be written:

$$\frac{|A|^2}{|A_i|^2} \approx 1 - \frac{(1-x^2)(1-y^2)}{4\pi^2 n_g^2 L^2 \left(\frac{1}{\lambda}-\frac{1}{\lambda_o}\right)^2 - \frac{1}{4}\left((1-x^2)+(1-y^2)\right)^2} \tag{4.63}$$

expanding about the denominator about λ_o, the following expression for a single resonance is obtained that should correspond to equation 4.26 for high quality resonators:

$$\frac{|A|^2}{|A_i|^2} = 1 - \frac{(1-x^2)(1-y^2)}{\frac{4\pi^2 n_g^2 L^2}{\lambda_o^4}\Delta\lambda^2 - \frac{1}{4}\left((1-x^2)+(1-y^2)\right)^2} \tag{4.64}$$

A graph of the single resonance expressions derived from spatial mode coupling (equation 4.26) and time mode coupling (equation 4.64) are shown in figure 4.6.

To obtain an expression for the dropped signal of a single ring resonator coupled to two waveguides, as shown in figure 4.5, the time constant τ in equation 4.45 is redefined as:

$$\frac{1}{\tau} = \frac{1}{\tau_e} + \frac{1}{\tau_l} + \frac{1}{\tau_d} \tag{4.65}$$

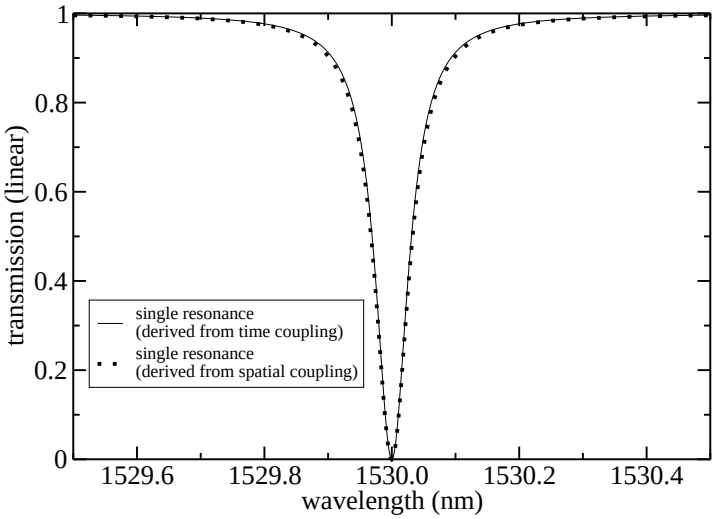

Figure 4.6: Equations 4.26 and 4.64 plotted together. The values chosen for the plot are: $n_g = 2.1$, $L = 178\,2\pi\,\mu m$, $\lambda_o = 1530\,nm$, and $x = y = 0.9$.

where τ_d is the time constant associated with coupling signal dropping waveguide. Similar to the relations in equations 4.62 and 4.61, the parameter x_2 can be related to the time constantτ_d with:

$$\frac{(1-x_2^2)c}{2\,n_g L} \approx \frac{1}{\tau_d} \tag{4.66}$$

4.6.1 Time Response

The amplitude response of a ring resonator has been presented in a steady state form (equation 4.53), where the assumption has been made that the excitation given by the driving waveguide is an infinite sinusoidal wave. The ring does however have a time constant, τ, associated with it. To examine the time dependence briefly and conveniently here, equation 4.46 is recalled, but this time it is assumed that the excitation (or signal in the initial waveguide) is on resonance and give by : $A_i = \Phi(t)e^{i\omega_o t}$. Where $\Phi(t)$ is a unit step function. Furthermore, the ring amplitude function is defined as: $h(t) = h_s(t)e^{i\omega_o t}$. Equation 4.46 can then be rewritten while dividing out the $e^{i\omega_o t}$ term (i.e. removing the high frequency component):

$$\frac{\partial}{\partial t}h_s(t) = -\frac{1}{\tau}h_s(t) - i\mu\Phi(t) \tag{4.67}$$

This equation can be readily solved using a Laplace transform to give:

$$h_s(t) = h_s(0)e^{-\frac{t}{\tau}} - i\mu\tau(1-e^{-\frac{t}{\tau}}) \tag{4.68}$$

The first term what is expected from a ring decaying that has no driving signal. The power associated with this term decays as $e^{-\frac{2t}{\tau}}$ [7]. The second term is the result of driving (resonant) signal. It also has a time constant, which emphasizes the point that resonators, in general, are frequency limited if the quality of the resonator is sufficiently high. The power associated with this term is given by: $h_s^* h_s = \mu^2\tau^2(1 - 2e^{-t/\tau} + e^{-2t/\tau})$.

[7]The quality (Q) of the ring can be derived noting that the power of a resonator decays as $e^{-\omega_o \frac{t}{Q}}$.

This is important because it shows that the ring requires time to yield the steady state response. This is because it is a feedback system.

4.7 Multiple Ring Filters

One of the advantages of viewing ring resonator filters with modes couple in time comes from the ability to simply represent multiple ring filters. This is done by describing multiple rings as a set of coupled first order differential equations. It has been shown that the solution to these equations can be written as a continued fraction [15]. The basic technique is used here to show the response of a two ring filter to be later related to a fabricated device, shown in figure 4.11. The set of differential equations can be used to describe two rings:

$$\frac{d}{dt}h_1 = (i\omega_1 - 1/\tau_1)h_1 - i\mu A_i - i\mu_1 h_2 \tag{4.69}$$

$$\frac{d}{dt}h_2 = (i\omega_2 - 1/\tau_2)h_2 - i\mu_1 h_1 \tag{4.70}$$

Where h_1 and h_2 define the bulk energies of the ring; ω_1 and ω_2 are the resonances of the individual rings; τ_1 and τ_2 are the time constants associated with the rings and generally follow the definition used in the single ring case; and μ_1 represents the coupling between the rings. It should be noted that the dimensions of μ_1 are (1/time) and therefore not the same as μ. To relate the value μ_1 to the normalized parameter for the coupler between the two rings, the power amplitude expression, equation 4.44, is used along with reciprocity of the coupler to obtain:

$$\mu_1 = \frac{c}{n_g}\left(\frac{1}{L_1 L_2}\right)^{1/2}(1-x^2)^{1/2} \tag{4.71}$$

Where it has been assumed that the group index of both rings are equal. If the driving frequency is assumed to be ω, and the lengths of the rings and couplers are assumed to be the same for both rings, the following expression for the dropped signal can be derived:

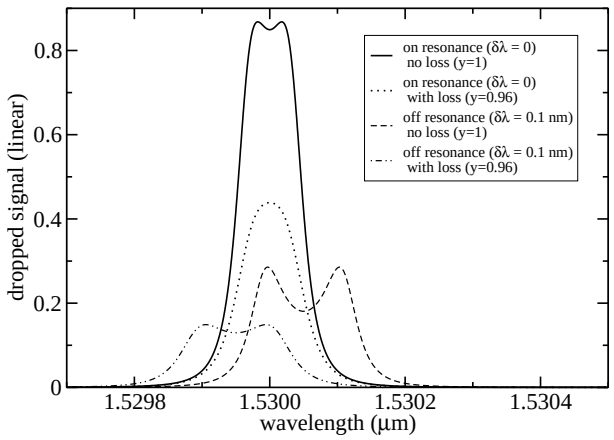

Figure 4.7: Shown are calculated spectra associated with a single resonance of a double ring resonator. The resonant wavelength is $1.530\,\mu m$. The parameters chosen and not noted in the graph are: $L = 100\,2\pi$, $x = x' = 0.90$, and $x_1 = 0.993$. The effects of loss and detuning are demonstrated.

$$D(\omega) = \frac{\mu'^2 \mu^2 \mu_1^2}{\left(\frac{\tau_1+\tau_2}{\tau_1\tau_2}\Delta\omega - \frac{\delta}{\tau_1}\right)^2 + \left(\mu_1^2 + 1/\left(\tau_1\tau_2\right) - \Delta\omega^2 + \delta\,\Delta\omega\right)^2} \tag{4.72}$$

where $\Delta\omega = (\omega_1 - \omega)$ and $\delta = \omega_2 - \omega_1$. δ is a detuning turn and can be used to model the Vernier effect [13] associated with two rings. The μ' term is defined by the coupling out of second ring to the output waveguide. Some example spectra can be seen in figure 4.7. Important aspects of this graph are that detuning can cause significant change in the spectral response and reduction of dropped signal. This is the essence of the Vernier effect. When the rings are detuned enough the signal passed approaches zero. It can also be seen that loss has, as expected, a significant impact on the strength (and shape) of the dropped spectrum.

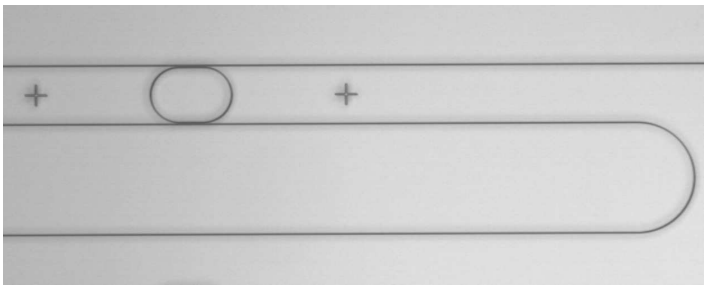

Figure 4.8: A picture of a single ring add-drop filter. The thickness of the waveguides used was $0.33\,\mu m$, the width of the waveguides was $1.2\,\mu m$. The radius of curvature was $25\,\mu m$.

4.8 Fabricated Devices

This section will show some of the filter devices made with silicon rich silicon nitride. The devices demonstrate the usefulness of the material platform for making high-index contrast based devices. Three basic devices are show-cased. The first is an add-drop filter similar to that modeled in figure 4.5. The second is a double ring filter. The third device is an ring device that pushes the limits of the curvature loss. High quality ring resonators were also designed and measured during this project [59].

4.8.1 Single Ring Channel Add-Drop Filter

A picture of a single ring add-drop filter is shown in figure 4.8. The film used to make this device was $0.33\,\mu m$[8] thick. The width of these waveguide were defined on the photolithogtaphic mask to be $1.2\,\mu m$. The linewidth reduction, measured with optical microscopy, was determined to be between $0.2\,\mu m$ and $0.3\,\mu m$. This measurement agreed with measurements made on similar samples during processing with a scanning electron microscope. The gap between waveguides in the coupling region, defined on the mask, were $0.4\,\mu m$. The corresponding center to center distance was designed to be $1.6\,\mu m$. The waveguides did not remain iso-

[8]The film was provided by Lambda Crossing

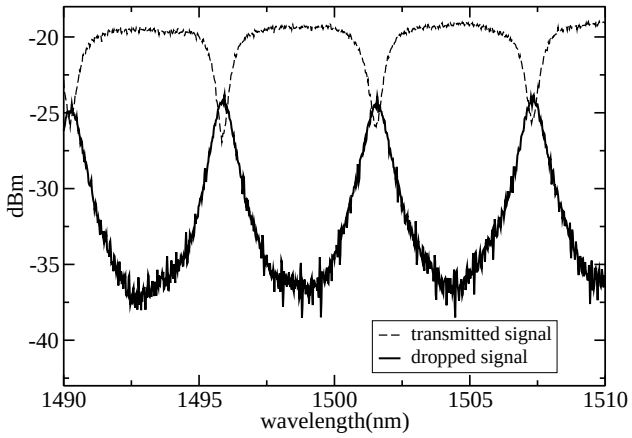

Figure 4.9: Transmission characteristic of a single ring add-drop filter. An extinction ratio of nearly $15\,dB$ is shown in the dropped signal (i.e. $D_{max} - D_{min}$).

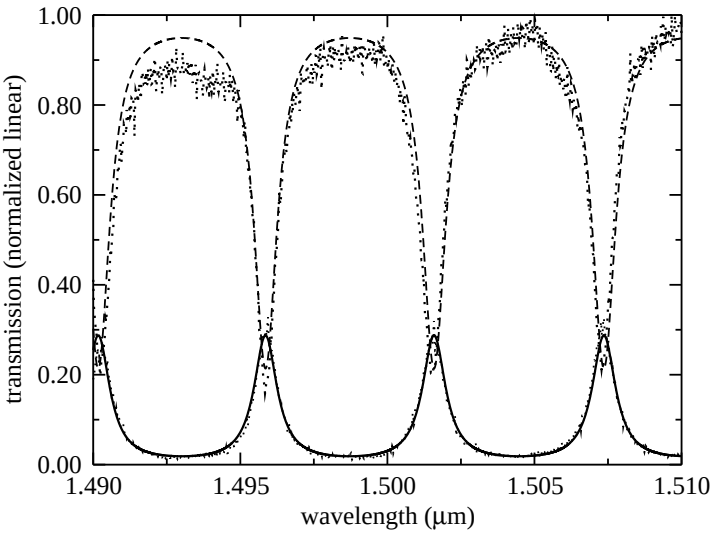

Figure 4.10: A linear plot of the graph shown in figure 4.9. A fit to the dropped signal is shown (solid line) and the parameters of this fit were used to plot the expected transmission spectrum (dashed line) on top of the transmission data.

lated during fabrication and showed a merging, similar to that seen in figure 2.5B. The device still displayed add-drop functionality - though for the TE polarization, but not as designed.

This device is particularly important because it shows that the material used to make low insertion loss waveguides (i.e. the waveguides were made from a $0.33\,\mu m$ thick film. See figure 3.10) can be used to make functioning filters. Reduced insertion loss is seen with much narrower waveguides than used for the filter, and practical applications could rely on tapering between narrow waveguide (giving a reduced loss at the interface to fibers) and wide waveguides (showing low curvature loss).

The measured power transmission of the device is shown in figure 4.9. Included on the graph is the transmitted signal, and the dropped signal. A fit to the dropped signal is shown in figure 4.10, along with a plot of the expected transmitted signal based on the parameters derived from the fit to the dropped signal. The agreement with the transmitted signal is good, though there is a slight shift in the resonance seen on at least one of the transmission dips. The reason for this is not known, but for the fitting process a constant effective group index was used to determine the period of the resonances. The effective group index is, however, not generally constant with varying wavelength and this could cause variations in the free spectral range associated with the spectrum.

The bending radius of the ring is $25\,\mu m$. The straight waveguide forming the coupler has a length of $21\,\mu m$. The measured FSR was $\approx 5.75\,nm$ $(767\,GHz)$ which corresponds to an effective group index of 1.97 at a wavelength of $1500\,nm$. The spectrum was normalized on a linear scale to the maximum of the transmitted signal. The normalized parameters supplied from the fit of the dropped signal were, $x = 0.870$, $x_2 = 0.0.867$ and $y = 0.787$. These parameters indicate that though the waveguides in the coupling region were merged, the structure maintained good symmetry with respect to the coupling ratios. The loss is higher than expected for the TE polarization in waveguides used (this is based on the data displayed in figure 3.15). The reason for this may be the sudden change in waveguide geometry in the coupling regions.

The full width at half maximum of the spectrum shown in figure 4.10 is $\approx 0.96\,nm$ $(128\,GHz)$. These values are not specifically useful in modern

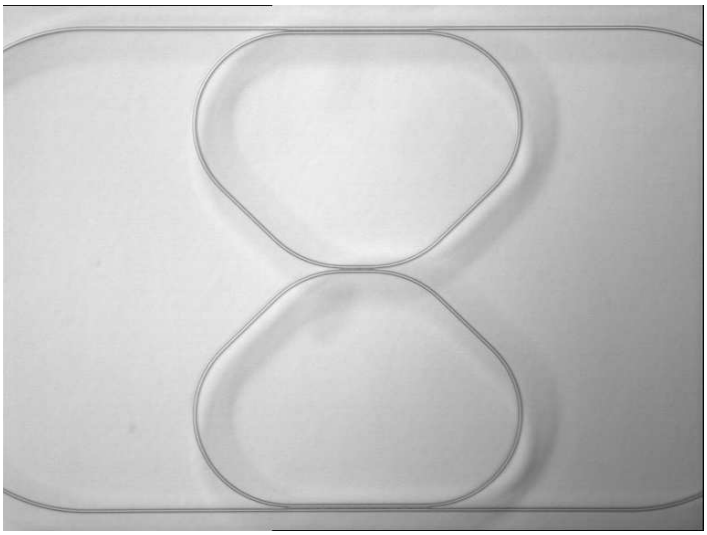

Figure 4.11: A double ring resonator filter made with $0.6\,\mu m$ thick, $1.0\,\mu m$ wide waveguides. The length of the coupling region between the rings and the straight waveguides is $50\,\mu m$. The length of the coupling region between the rings was $15\,\mu m$.

optical communications, and the shape of the channel selecting dropped spectrum is not ideal. With a single ring, the response is a Lorentzian - as seen. Higher order filters - utilizing more rings cascaded together can give a more useful response.

4.8.2 Double Ring Channel Add-Drop Filter

A double ring filter was designed, and fabricated with a $0.6\,\mu m$ thick silicon rich silicon nitride film. A picture of the device is given in figure 4.11. The lengths of the couplers of the two large rings to the waveguides are $50\,\mu m$. The length of the coupler between the rings is $15\,\mu m$. The total length of both rings is $340\,\mu m$. The width of the waveguides (on mask) are $1.0\,\mu m$ and the linewidth reduction for waveguides fabricated at the same was measure to be about $0.3\,\mu m$. The spectrum is shown in figure 4.12. The dropped signal shows a extinction ration of about $25\,dB$ and the full

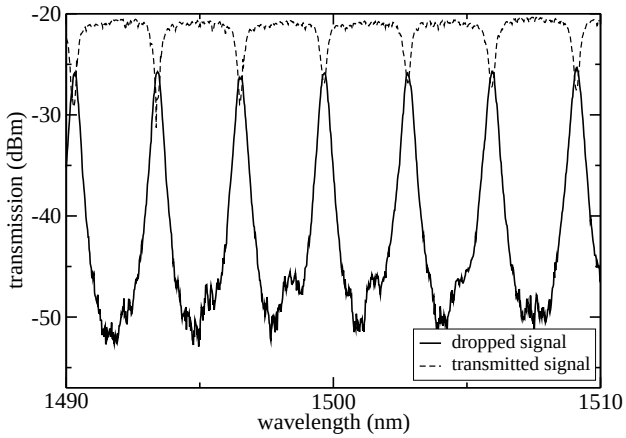

Figure 4.12: The frequency response spectrum of the double ring resonator filter. The TE-polarization added and dropped signals are shown.

width at half maximum of the resonant peaks is $0.32\,nm$ ($\approx 43\,GHz$ at a wavelength of $1500\,nm$) for the spectral range shown. The intended full width at half maximum was $0.2\,nm$ ($\approx 27\,GHz$ at $1500\,nm$). The FSR of the device at about $1500\,nm$ is $3.16\,nm$. This corresponds to an effective group index of 2.09, which is slightly lower than would be expected for this geometry (assuming the measurement of the line width reduction was accurate).

Fitting to the resonator represents problems because there are so many different parameters that can have an effect. Detuning, loss, and shifts in coupling of the 3 couplers making up the ring present a large parameter space to fit unambiguously. What the results clearly show is that the resonances of the rings are very close, indicting that the processing is good enough to yield low variation in effective optical distance ($n_{eff}L$). The ability to detune the resonances of the ring with, for instance, thermal control would allow the transmission of the dropped signal to be maximized and possibly improve performance.

Figure 4.13: Two rings with radii of $6\,\mu m$ and $8\,\mu m$. The thickness of the film used to make these resonators was $0.6\,\mu m$ and the waveguide width before linewidth reduction was $1.2\,\mu m$.

4.8.3 Micro-Resonators

Figure 4.13 shows two of the smallest micro-rings made with the silicon rich silicon nitride technology during this project. The radii of the rings shown are $6\,\mu m$ and $8\,\mu m$. The transmission spectrum for the smallest ring is shown in figure 4.14. The transmission of the TE mode has been fit with the theoretical transmission spectrum from equation 4.20. The normalized parameters x and y yield values of 0.45 and 0.37. Since the parameters are defined symmetrically, which number corresponds to the loss and which number corresponds to the coupling is ambiguous. what is clearly shown is that the resonator is lossy - as would be expected from the data shown in figure 3.15. The coupler is less that ideal with a coupling region made from two merged waveguides. This can cause loss of signal - effectively increasing ring loss.

The free spectral range of this device is greater than $30\,nm$ with an effective group index, derived from the fit, of 2.05. This value roughly agrees with other measurements of the effective group index.

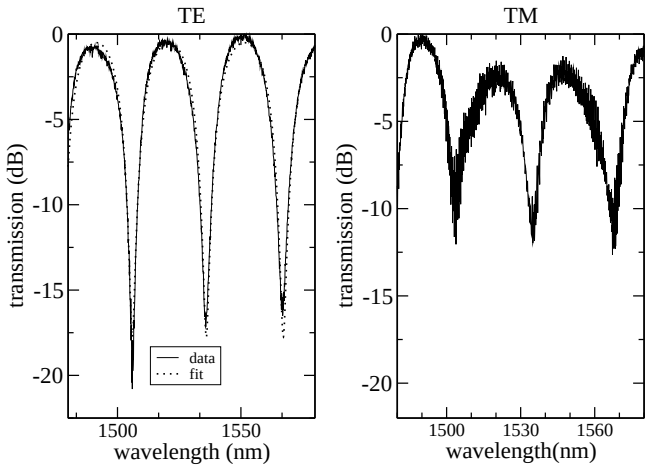

Figure 4.14: Transmission spectrum from the 6 μm radius ring shown in figure 4.13. Both polarization show significant resonance characteristics.

4.9 Conclusion

A basic model of ring resonator based devices has been presented. Using modes coupled in time allows for a simple set of differential equations to approximate the response of ring based devices. This is useful not only for multiple ring devices, but for examining the time evolution of ring based filters.

A number of devices have been demonstrated including a single ring add-drop filter, a double ring add-drop filter and micro-ring resonators.

Chapter 5

UV Engineered High-Index Contrast Devices

This chapter presents work done on the combination of high-index contrast waveguides and a germanium doped, UV-sensitive, silica cladding. The addition of the UV-sensitive layer makes novel hybrid devices possible because a permanent refractive index change can be induced in the cladding of the high-index contrast waveguides. At least two different methods of exploiting this UV-sensitive layer have been explored. The first of these involves directly writing waveguides in the photosensitive layer using a focused UV beam. Waveguides made with this method have been shown to have low insertion loss when coupled to standard optical fiber [60], and this opens the possibility of enhancing the coupling of high-index structures. The specific possibility explored here was the direct coupling between UV-written waveguides and high-index ring resonator structures. Though the efficiency of couping between ring resonators and UV-written waveguides is low because there is a large difference in index contrast, and thus propagation constants, it was believed that high-quality ring resonators could be used to overcome these difficulties and pass signals at specific wavelengths between UV-written waveguides and high-index waveguides.

A UV-sensitive cladding also makes it possible to use UV illumination and phase masks to write cladding-based gratings for high-index wave-

guides that may not readily display photosensitivity on their own. This makes an effective technique for directly measuring waveguide properties available. It is more direct than measurements based on ring resonator since though information gleaned from a ring resonator spectrum may include the effective group index, coupling to the ring and loss in the ring, it does not include direct measurement of the effective index. Modeling can be performed to correlate the effective group index with a waveguide geometry and then extract the effective index using a mode solver, but this approach requires assumptions about waveguide geometry and may not produce conclusive results. In addition to measuring the effective index directly, the introduction of a cladding based grating makes an extensive repertoire of grating based filter devices available.

5.1 UV Sensitivity

The UV sensitivity of germanium doped glass has been known since the late 1970's when a grating was accidentally made with a standing wave of UV light in a fiber [8, 61]. The mechanism of the sensitivity was not fully understood and there has been much debate on the specifics of the mechanisms involved. It is generally agreed that germanium related oxygen deficient centers (GODC) are involved [62], and at another level that UV radiation causes defects that increase absorption in the UV ($240\,nm$) and that this in turn raises the refractive index via the Kramers-Kronig relations [63, 64].

It has also been observed that subjecting a sample to high pressure hydrogen, thus causing diffusion of hydrogen into the germanium doped glass, increases the absorption of the sample during UV irradiation. This leads to an increased photo-sensitivity of the material - i.e. making the permanently induced index change of the sample greater for a given fluence of UV-radiation [65]. However, the O-H bonds that result from this loading and irradiation can also cause significant absorption near a wavelength of $1.39\,\mu m$ [10] and can cause poor transmission in the communication bands. The solution offered for this is to load the samples with deuterium (D_2) instead of hydrogen H_2. This shifts absorption away from the communications band but still provides the benefit of increased

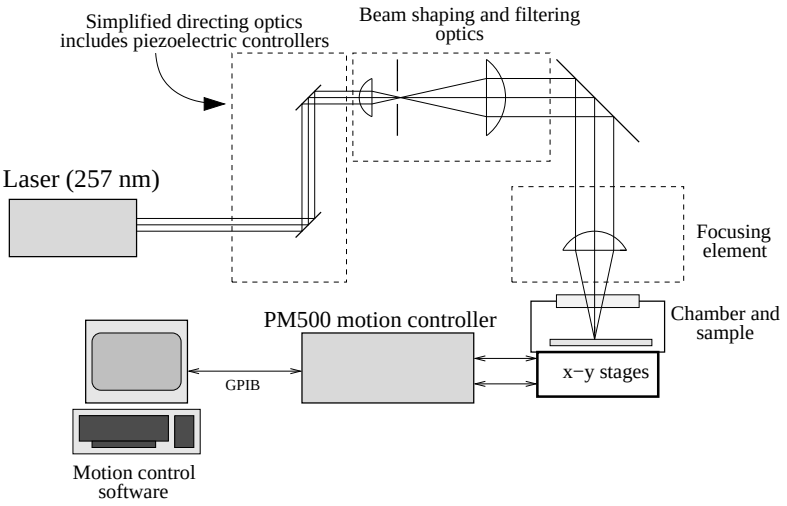

Figure 5.1: A digram of the set-up used for direct writing of UV-induced waveguides in germanium doped silica layers. The Laser used was a frequency double argon ion laser with a wavelength of $257\,nm$. The beam was focused to a $3\,\mu m$ spot for writing waveguides.

photo-sensitivity [66].

Gratings were the first devices made using the UV-sensitivity of germanium doped glass - first by standing waves in the fiber [61]; then by illumination of a fiber from the side using an interferometer to create a modulated index; and then by the use of phase masks [8], which have greatly simplified the process of making fiber gratings. Gratings in planar devices have been explored using the same basic mechanism exploited in fibers [67–69].

In addition to gratings, one of the areas that has exploited the UV sensitivity of germanium doped glass in integrated optics is the fabrication of directly written UV waveguides [25, 60]. These waveguides, which are used in this report to couple to high-index contrast structures, show good coupling to standard optical fiber, and low propagation loss [70]. They have also proved useful for making devices such as splitters [71], couplers [72, 73] and interferometer based variable optical attenuators (VOA's) [74].

5.2 Direct UV-writing Set-up

A high-level diagram of the direct UV-writing set-up is shown in figure 5.1, details of optical elements are omitted. More information on the UV writing setup can be found in other references that concentrate on the details of UV-writing techniques [66]. The main components are a laser source; beam shaping and focusing optics; a vacuum chamber that holds a sample during writing (protecting the sample from particulate contamination and moisture) ; and motion control hardware/software used to translate the sample under the focused beam while writing waveguides. The source is a frequency doubled argon ion laser. The wavelength emitted is $257\,nm$. The output power of the laser at this wavelength that was used was between 30 and 50 mW. The beam shaping optics ensured a well defined optical field with little astigmatism, that was focused to a $3\,\mu m$ spot (defined by the diameter of the spot at which the power density if reduced to $1/e^2$ of the peak value).

The sample was translated under the focused beam using PM500 stages with a positioning resolution of $0.1\,\mu m$. During writing, the PM500

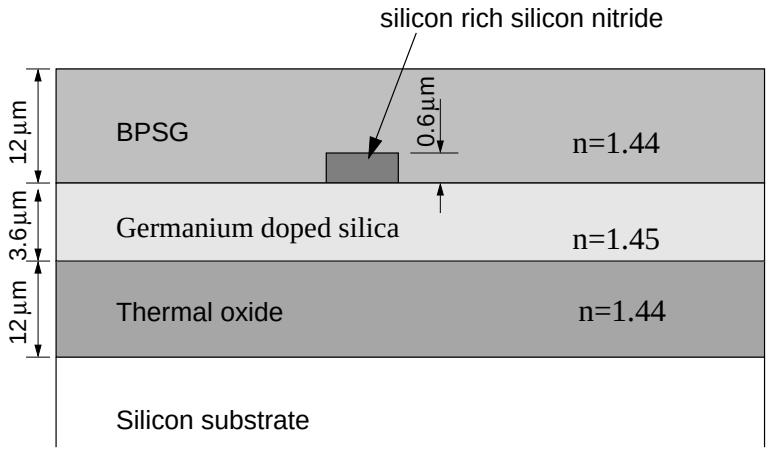

Figure 5.2: The configuration for the first generation hybrid devices combining high index waveguides and an a photosensitive, germanium doped layer.

was actively controlled using LabView software. This provided active feedback and good stability for writing.

5.3 Cleanroom Fabrication

Before writing UV-induced waveguides, samples were prepared in the cleanroom facilities at COM. These samples combined high-index contrast waveguides and a UV sensitive layer of germanium doped glass in which UV waveguides would be written. Two configurations were used. These can be seen in figures 5.2 and 5.3. Both configurations started with a thermal oxide layer grown on top of a silicon wafer. The thickness of this layer varied between $10\,\mu m$ and $12\,\mu m$.

For the first configuration, figure 5.2, a $3.5\,\mu m$ thick layer of germanium doped glass was deposited using plasma enhanced chemical vapor deposition (PECVD). The concentration of germanium was approximately 10%mole. The refractive index of this layer was measured using

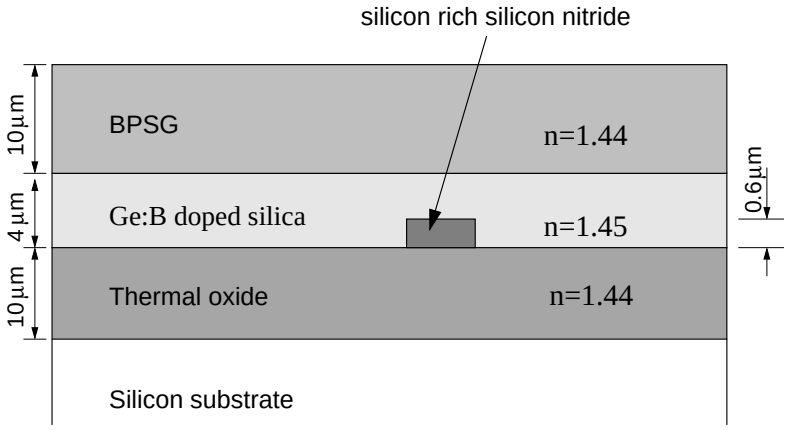

Figure 5.3: The configuration the for second generation hybrid devices combining high index waveguides and an a photosensitive, germanium doped layer. This photosensitive layer in this configuration also contains boron.

a prism coupler and a process standard (a wafer prepared simultaneously with the sample used to make the device) to be approximately 1.45. On top of this layer, silicon rich silicon nitride was depositied with LPCVD. Waveguides were defined using contact UV photolithography and reactive ion etching (RIE). After etching, a top cladding of borophosphosilicate glass was deposited using PECVD.

The second configuration, figure 5.3, is similar to the first in that it has a germanium doped UV sensitive layer, but but the thickness, and orientation of the photosensitive layer is different. The sample was prepared by depositing the silicon rich silicon nitride directly on the thermal oxide layer. After etching with RIE, a photosensitive layer of glass was deposited on top of the waveguides. Besides being deposited on top of the high-index contrast waveguides instead on the thermal oxide layer, it was doped with boron in addition to germanium, and the thickness of the layer was approximately $4\,\mu m$ instead of $3.5\,\mu m$. The boron doping was done to reduce the index difference between the non-exposed UV

sensitive layer and the thermal oxide layer. The purpose of this was to produce a homogeneous (in terms of refractive index) cladding for the UV-written waveguides. This general technique is commonly applied to UV-written waveguide devices at COM. The calibration, however, erred and the refractive index of the layer was only slightly lower than that of the photosensitive layer in the first sample. The concentration of germanium was similar to the first with 10%mole. The thickness of the photosensitive layer was $4\,\mu m$. After deposition of the photosensitive layer, a borophosphosilicate top cladding was deposited - similar to the first configuration.

5.4 Preparation for UV Writing

Before proceeding with UV writing, samples (both configurations) were placed in a high-pressure deuterium environment to increase the photosensitivity of the germanium doped layer [65]. Samples made with the first configuration were loaded at a pressure of $500\,bar$ for 2 weeks to yield an approximate D_2 concentration of 6%mole. Samples having the second configuration were loaded at a pressure of $500\,bar$ for 1 month to produce an approximate D_2 concentration of $6\,\%mole$ [1]. After loading the samples were stored in a refrigerator at $\approx -120^{\circ}C$ to prevent out diffusion of Deuterium before writing.

Several techniques were used for the alignment of UV-written waveguides to high-index contrast structures. The most effective method used a single, straight high-index contrast waveguide for alignment. The focused UV spot was translated over the high-index waveguide and a diffraction pattern marked the point at which the spot intersected the waveguide. The x and y coordinates were recorded, and the procedure was repeated at many different points along the waveguide. A line was fit to the data acquired. The UV-waveguides were written parallel to this waveguide (i.e. with the same slope) and the intercept was adjusted to intersect or come close to the desired high-index contrast structures. Though the procedure was only used for making straight UV-written

[1] The solubility of D_2 in silica is $116\,ppm$ [66]. Both samples were loaded until saturation.

waveguides that were parallel to the high-index contrast waveguides, a similar procedure using high-index contrast waveguide segments perpendicular to the first alignment waveguide could be used to define another reference line. The known intersection of two lines would yield sufficient information for making more complex UV-written structures aligned to high-index waveguides. The alignment procedure allowed for a high degree of accuracy and allowed for sub-micron alignment - approximately within $0.5\,\mu m$.

After alignment of the sample, free-standing UV-written waveguides were made with different translation speeds and laser powers. The writing process was visually monitored to ensure uniformity of the writing process and assess which translation speeds and laser powers were likely to produce the best waveguides. At times, in preparation of UV-writing, test samples were used on which only calibration waveguides were written. The UV-written waveguides on these samples were inspected under an optical microscope to ensure good waveguide quality.

5.5 Devices Made with First Configuration

5.5.1 Device One

The first device made combining directly UV-written waveguides and high-index contrast waveguides was composed of a free-standing high-index contrast ring resonator coupled to a UV-written waveguide. The diameter of the ring was $178\,\mu m$ and the width of the high-index waveguide was $1.4\,\mu m$ (estimated total width after processing). After alignment of the sample and calibration of the direct UV-writing set-up, a laser power of $45\,mW$ was used to write waveguides with a translation velocity of $100\,\mu m\,s^{-1}$. The approximate index change of the UV-written waveguides was estimated to be $n \approx 0.04$.

Measurements of a waveguide written to tangentially intersect (or nearly intersect) a $178\,\mu m$ diameter ring indicated resonance associated with the ring was weak, but clearly present for the TM polarization. A portion of the spectrum is shown in figure 5.4. A peak attenuation due to resonance shows only a 2.5% reduction in signal. The excess

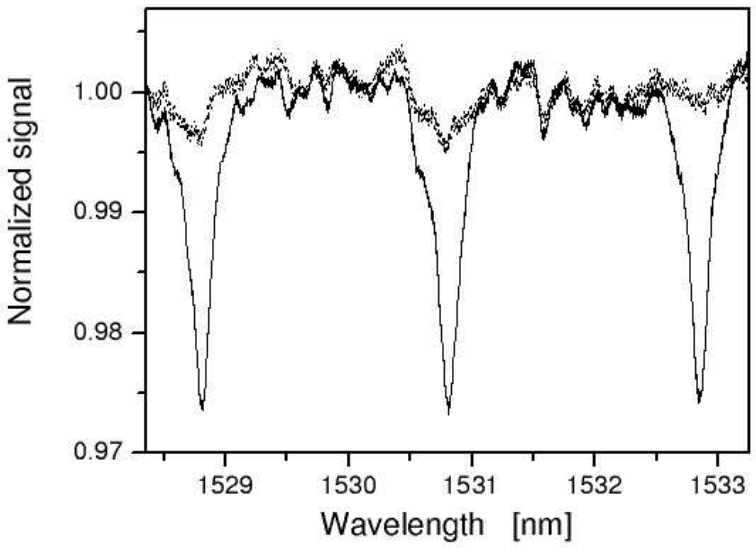

Figure 5.4: Response of the first high-index contrast ring resonator coupled to a directly UV-written waveguide. The solid line, showing resonance, is the TM polarization. The dotted line is the TE polarization. The radius of the ring was 89 μm (diameter=178 μm).

insertion loss caused by the introduction to of the ring when compared to similar UV-written waveguides on the same sample was $2.1\,dB$. The total insertion loss of the device, which was $2.4\,cm$ long, was $5.7\,dB$. Further optimization of the UV written waveguides can yield lower insertion losses [60].

The transmission spectrum of the single UV-written waveguide coupled to the silicon rich silicon nitride ring shows a FSR of $2.02\,nm$ which corresponds to an effective group index of $n_g = 2.07$ at a wavelength of $1530\,nm$. The full width at half maximum of the resonances were measured to be approximately $0.20\,nm$ ($\approx 25GHz$). Using these values, the finesse of the device was approximately ≈ 10.

It is unclear whether fits to the spectrum using the ring resonator model from equation 4.20 yield meaningful results. The coupling region is highly asymmetric, there is loss caused by the ring, and the UV-written waveguide only presents a small perturbation for a high-index contrast ring. The assumptions implicit in the description of the coupler in equation 4.12 is not applicable. There has been some attempt by other groups to explain the nature of the coupling [75].

Measurements of this device after fabrication revealed that the center to center distance between the UV-written waveguide and the ring waveguide was $\approx 3.4\,\mu m$. The width of the UV-written waveguide was approximately $4.6\,\mu m$.

Inspection of the sample under an optical microscope revealed no obvious damage of the ring caused by UV writing.

5.5.2 Device Two

The second ring resonator device was made with a slower scan speed of $83\,\mu m\,s^{-1}$ and a similar laser power, $45\,mW$, when compared to the first sample. The ring used was $218\,\mu m$ in diameter. The cross-sectional dimensions of the high-index waveguide remained the same. The response was a slightly greater attenuation due to ring resonance of 3.5% for a wavelength range similar to the that shown for the first device (figure 5.4). This may have been due to the increased modal confinement and effective index of the guided mode associated with the UV-written

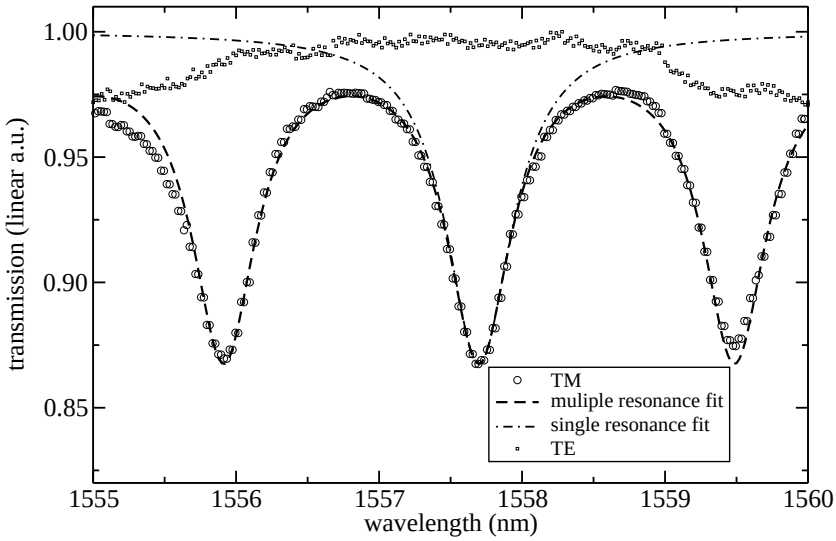

Figure 5.5: Resonant spectrum for the second device using a directly UV-written waveguide with a ring resonator. The diameter of the ring resonator was $218\,\mu m$. The cross-sectional dimensions of the high-index waveguide were approximately $0.6\,\mu m \times 1.4\,\mu m$.

waveguide causing a greater normalized projection onto the high index contrast waveguide. The size of the resonances dips were greater in different wavelength ranges. Figure 5.5. The figure is shown with both polarization. Again, only the TM polarization showed noticeable resonance with a resonant dip-size ($T_{max} - T_{min}$) that approached 10%. Also shown in the figure are the single resonance (equation 4.26) and full spectrum fit (equation 4.20). The interpretation of the normalized parameters in this situation remains unclear, but they are given here as a possible explanation of the response. The x and y parameters from the fit are 0.4 and 0.97. Since the parameters are symmetric, which value corresponds to the coupling and which one corresponds to the transmission around the ring remains ambiguous. It can, however, be speculated that the coupling is small because of the extreme mismatch in the propagation constants so that $x = 0.97$ and $y = 0.4$. If the model is trusted, the fraction of power coupled from one waveguide to the other is given by $(1 - x^2) \times 100 = 5.9\%$. The round trip ring loss is then approximately 84%. The expected loss for a $218\,\mu m$ diameter ring is lower (recall loss from figure 3.15). It remains possible that higher order modes have been coupled to since the $1.4\,\mu m$ wide waveguide that the ring is made of is well within the multi-mode regime (see figure 3.2). The lower effective index would explain relatively high coupling and the less confined mode would experience more loss when propagating around a bend. This remains speculative without direct measurement of the coupling and loss in the given waveguide. This was not possible with the given high-index structures on the mask used. The FSR of the device was $1.78 \pm 0.03\,nm$ yielding an effective group index of $n_g = 1.98$ assuming a wavelength of $1558\,nm$. The FWHM (full width at half maximum) of the resonances (by measurement or equation 4.29) was $0.46\,nm$. The Finesse of the device in the wavelength region shown in figure 5.5 was 3.9.

Extreme cases of UV induced damage to the high index waveguide was observed (figure 5.6). Direct exposure of the high-index waveguides obliterated the waveguides and must be considered a prime candidate for causing excess ring loss for configuration number 1. The damage was not seen with the first sample, which was prepared in parallel with the second sample. The decrease in scan speed may have caused a prolonged expo-

Figure 5.6: A picture of severe damage to the edge of a high-index contrast (silicon rich silicon nitride) waveguide caused by the focused UV-beam used to make the directly UV-written waveguides. Two UV-written waveguides are shown horizontally and one vertically.

sure that crossed a threshold of damage. It is also possible that though visible damage was not seen in sample one, it occurred and was not noticeable upon visual inspection. The mechanism causing damage may be thermal (i.e. localized heating caused by the absorption of UV radiation in the germanium doped silica), or it could have another, perhaps more direct, cause.

5.5.3 Trimming of Device One

An attempt was made to improve performance of the first device by use of long period gratings and subsequent UV exposures. Phase matching conditions for propagating modes in the high-index contrast and UV waveguides follow the relation [76]:

$$\Lambda_{grat} = \frac{\lambda}{n_{eff_1} - n_{eff_2}} \tag{5.1}$$

where Λ_{grat} is the period of the grating, n_{eff_1} and n_{eff_2} are the effective indexes of the waveguides. The intent of the experiment was to increase coupling of the TE polarization so that the device would display

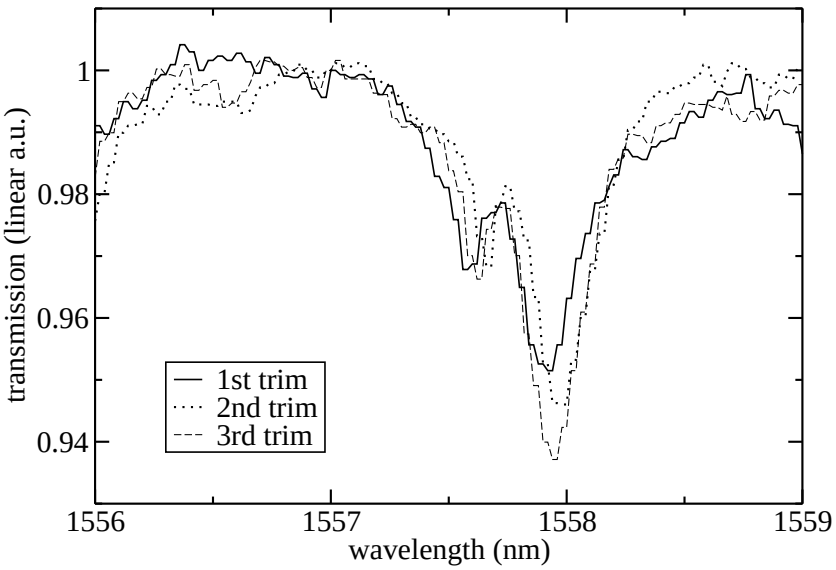

Figure 5.7: Spectra showing the effects of successive UV trimming of a UV waveguide coupled to a high-index contrast ring resonator (diameter $= 218\,\mu m$)

resonance for a polarization that was previously not displayed. The effective index of the TE polarization for a $0.6\,\mu m$ high, $1.4\,\mu m$ wide high index waveguide was calculated to be 1.83. The effective index of the UV-written waveguide was measured by writing a weak UV-grating with a phase mask having a period of $1057.09\,nm$ to have an effective index of ≈ 1.450. The effective index change induced by rescanning the waveguide with a focused UV spot was measured by tracking shifts in the reflected spectrum grating resonances. The shifts corresponded to an index change of $5.0 \pm 0.2 \times 10^{-4}$ for a $30\,\mu m\,s^{-1}$ scan speed and a $40\,mW$ beam power.

The corresponding period of the long period grating to assist the coupling between waveguides was $3.94\,\mu m$ - derived from equation 5.1.

Since the ring has a curvature of $178\,\mu m$ the length of the coupler is short. If it is assumed the coupler will be defined by a length through which the ring remains within one micron of its original position with respect to the UV-written waveguide, then the total length of the coupler is given from the Pythagorean theorem as $2(89^2 - 88^2)^{1/2} = 26.6\,\mu m$. This length mean that only about 6.8 grating periods will occur in the coupling region.

Long period gratings were written in the coupling region of the waveguide by scanning the focused UV beam at a velocity of $30\,\mu m\,s^{-1}$ with a power of $40\,mW$. The beam was chopped to produce the desired spatial frequency (i.e. $(30\,\mu m s^{-1})/(3.94\,\mu m) = 7.61 Hz$).

The transmission of the UV waveguide coupled to the ring is shown in figure 5.7. A resonance for the TE polarization was never observed. There was however a change in the resonance associated with the TM mode. Figure 5.7 shows a progression of trimmings. The first trimming was the result of a $3.9\,\mu m$ period grating written with a chopped beam. The second was the result of a retracing of the original waveguide without chopping. The third was again written with a $3.9\,\mu m$ chop period.

Though no noticeable grating effect is noticeable, there was a small deepening of the resonance and slight shifts in the resonance frequency. The shifts do not have a tendency in any particular direction, but may be the result of damage to the ring caused by UV irradiation. The deepening of transmission dips is speculated to come from an increase in the refractive index of the UV written waveguide.

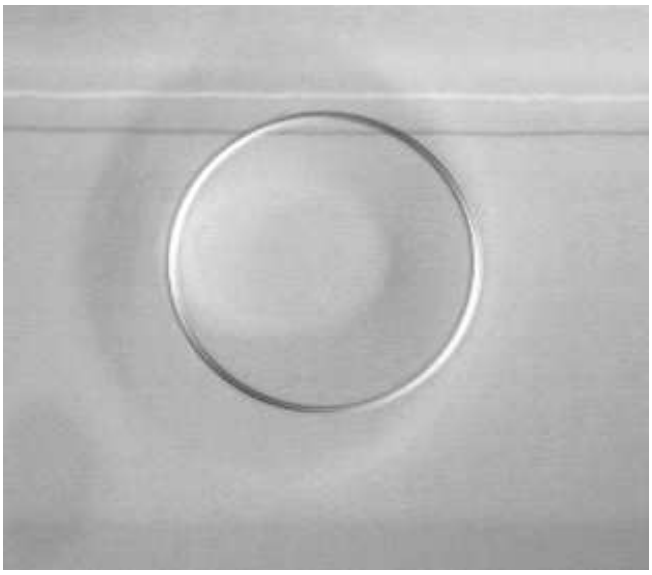

Figure 5.8: A $25\,\mu m$ radius high-index contrast ring resonator coupled to a directly UV-written waveguide. The second configuration(figure 5.3) was used to make this device.

5.6 Devices Made with Second Configuration

5.6.1 Ring Resonator - Configuration 2

The second configuration, see figure 5.3, was used to make a device similar to those covered in the last section. The ring used for the experiment had a $25\,\mu m$ radius and a waveguide width (on mask) of $1.0\,\mu m$. The linewidth reduction for this sample was measured to be between $0.3 \pm 0.1\,\mu m$. The UV waveguides were written with a beam power of $38\,mW$ and the translation velocity was $100\,\mu m s^{-1}$. It was intended that the germanium doped layer deposited over the high-index contrast waveguides would serve to protect the high-index contrast waveguides from UV damage during writing as well as provide a medium in which to write UV-written waveguides. Figure 5.8 shows a picture of this device. The normalized transmission of the UV waveguide coupled to the ring is shown in figure 5.9.

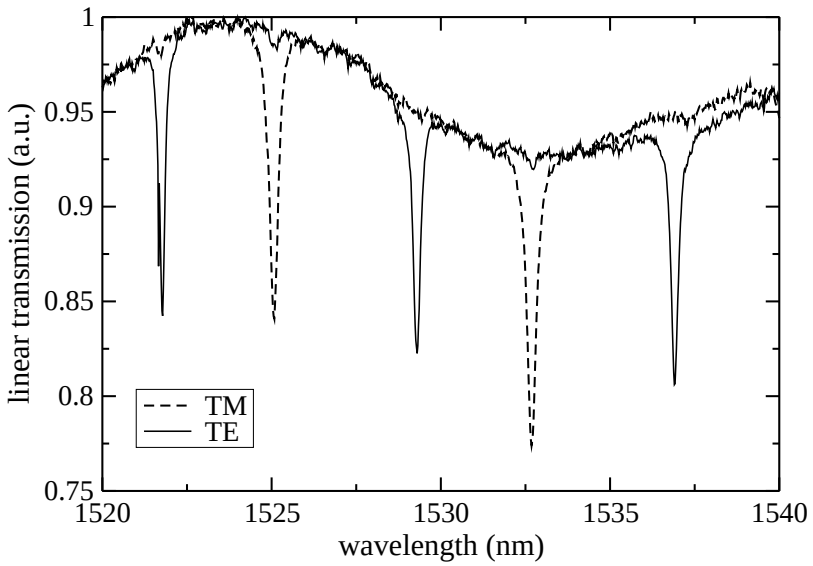

Figure 5.9: The transmission spectra of the UV-written waveguide coupled to the high-index ring shown in figure 5.8. Both polarizations show resonance and there is a sinusoidal modulation of the signal.

Several characteristics distinguish this device from the devices made with the first configuration. First, both polarizations clearly show resonance. Second, the dip-size is approximately 15 %. Third, there is a sinusoidal variation superimposed on top of the transmission spectrum. The third point is probably the easiest to explain. The UV-written waveguide is written directly on top of the high index waveguide, and the presence of the high-index waveguide can act as a significant perturbation for the propagating modes in the UV-written waveguide. The approximate period of the sinsoidal pattern is $18.7\,nm$. The size of a cavity, d, with a free spectral range of $\delta\lambda$ is given by:

$$d = \frac{\lambda^2}{2\,\delta\lambda\,n_{group}} \tag{5.2}$$

Where n_{group} is the effective group index of the propagating mode, and λ is the wavelength. Assuming a wavelength of $1.53\,\mu m$ and approximating the effective group index of the UV written waveguide with the effective index, $n_g \approx 1.45$, the size of the cavity is approximately $43\,\mu m$. Since the diameter of the ring is approximately $50\,\mu m$, the dimension suggests that the presence of the ring acts as a cavity where the propagating mode in the UV waveguide begins to alter before the actual intersection of the waveguides.

The free spectral range of the resonator for the TE and TM polarization is $7.56 \pm 0.03\,nm$ and $7.55 + / - 0.03\,nm$, respectively. The effective group index corresponding to this is $n_g = 1.97$. The near degeneracy of the free spectral range could be a sign that the waveguide is symmetric - though not necessarily (see figure 3.6). The effective index is however less than expected in this case. The effective group index calculated for a straight $0.6\,\mu m \times 0.6\,\mu m$ silicon rich nitride waveguide clad in silica is 2.13.

The full width at half maximum for the resonances - approximated directly from the graph - are $0.22\,nm$ for the TE mode and $0.29\,nm$ for the TM mode. The finesses of the the two polarizations are 34 and 26 for the TE and TM modes, respectively. The quality of the resonators are approximately 7000 and 5300 for the TE and TM modes, respectively. Though more work is needed for practical devices, one advantage of the

ring is the relative uniformity of the different polarization - if not in positioning of the peaks, at least in the presumed coupling to the ring.

5.6.2 UV-Grating

The combination of high-index waveguides and a photo-sensitive cladding means it is possible to make gratings in the photosensitive layer for use with the guided modes of the high-index waveguides. Though there have been reports of photosensivity in $SiON$ and Si_xN_y waveguides [77], attempts to write gratings directly in these waveguides have failed in the efforts at COM. Gratings are, however, desired because they are useful tools for the analysis of propagating modes in waveguides and for the construction of complex optical filters.

With sample in the second configuration, figure 5.3, a $930.8\,nm$ period phase mask was used with a pulsed excimer (KrF) laser ($248\,nm$) to write a grating across several high-index contrast waveguides of varying widths. The single pulse fluence of the laser was measured to be $112\,mJ\,cm^{-2}$. Two attempts were made at writing a grating. The first was with 10^4 pulses and the transmission of the high-index waveguides showed no obvious grating effect. The second attempt used 10^5 pulses and showed a strong grating effect for two different waveguide widths in the wavelength range ($\approx 1450 - 1580\,nm$) observed. After UV-writing a preliminary assessment of waveguide transmission, the samples were placed on an $80^\circ\,C$ hotplate and heated for 24 hours to facilitate the out diffusion of deuterium. Spectra taken at this point from the sample displaying clear grating behavior are shown in the top frames of figures 5.10 and 5.11. The width of the waveguides measured in the figures 5.10 and 5.11 are $1.2\,\mu m$ and $1.0\,\mu m$, respectively. These widths are quoted from the values on the photolithographic mask.

The grating effect is strong in the transmission spectrum and show extinction ratios that exceed $20\,dB$. The wavelengths at which the transmission dips, or grating resonance, occur are indicators of the effective index at that wavelength. The relationship between grating period and reflected wavelength is:

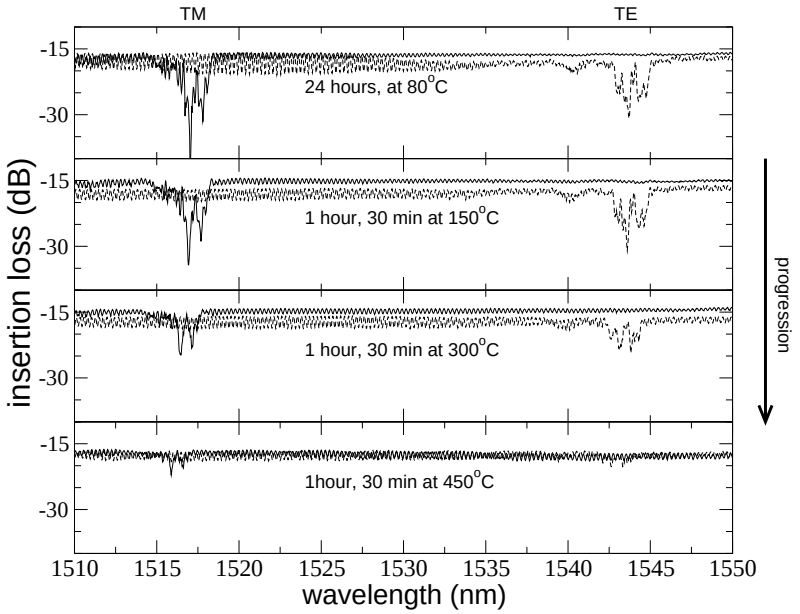

Figure 5.10: Transmission spectra of $1.2\,\mu m$ wide (on mask), $0.6\,\mu m$ thick silicon rich silicon nitride waveguides showing the effects of a grating written in a germanium doped silica cladding layer. The physical configuration of the device is shown in figure 5.3. The separation between the resonances is the result, at least partially, of geometrically induced birefringence. Heating of the sample causes a significant reduction in grating strength. The progression spectra measured after successive annealing follows from top to bottom.

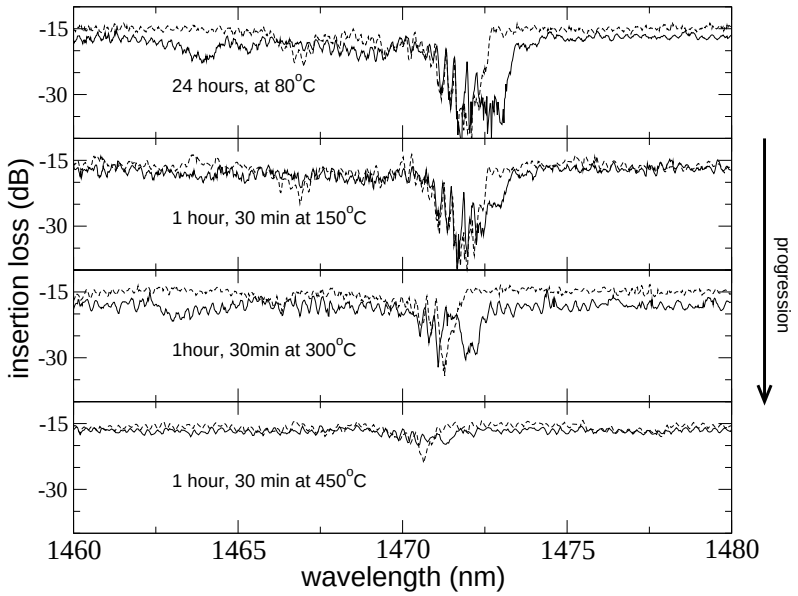

Figure 5.11: Transmission spectra of 1.0 μm wide (on mask), 0.6 μm thick silicon rich silicon nitride waveguides showing the effects of a grating written in a germanium doped silica cladding layer. The physical configuration of the device is shown in figure 5.3. This should be compared to figure 5.10 to see the effects of geometrically induced birefringence. Heating of the sample causes a significant reduction in grating strength. The progression spectra measured after successive annealing follows from top to bottom.

$$n_{eff} = \frac{\lambda}{2\,\Lambda_{grat}} \tag{5.3}$$

$$= \frac{\lambda}{\Lambda_{phase}} \tag{5.4}$$

where λ is the wavelength of resonance, n_{eff} is the effective index, Λ_{grat} is the period of the grating written, and Λ_{phase} is the period of the phase mask used to make the grating. The effective index is generally a function of wavelength and the grating period, Λ_{grat}, is half the period of the phase mask, Λ_{phase} [78]. Using this relationship and the wavelengths of peak attenuation for the waveguides the effective indexes can be derived. The effective index for both polarizations of the $1.0\,\mu m$ wide waveguide was calculated to be 1.581 and the effective index for the TE and TM polarizations of the $1.2\,\mu m$ wide waveguide were calculated to be 1.659 and 1.630. The near degeneracy of the the effective index for both polarizations of the $1.0\,\mu m$ waveguide suggests there is a symmetry (see figure 3.4) with respect to a 90° rotation of the waveguide cross-section. The slightly higher cladding index, caused by the germanium doping, only introduces a small perturbation of the situation shown in figure 3.4. If it is assumed that degeneracy with respect to polarization is a sign of symmetry, then the linewidth reduction of the waveguide is $0.4\,\mu m$. This value is close to the value expected from linewidth reduction measurements performed on similar samples and is well within the range of samples as a whole. The wider waveguide, $1.2\,\mu m$ shows a large separation between the polarizations, and if the variation of the effective index with wavelength is momentarily ignored, the change in effective index with waveguide width can be approximated:

$$\frac{\partial \Delta n_{eff}}{\partial w} = \frac{1.659 - 1.630}{0.2\,\mu m} = 0.15\,\mu m^{-1} \tag{5.5}$$

This is slightly lower than that expected from the slope of the birefringence taken at the point of symmetry, equation 3.16, but when the birefringence calculated for a wavelength of $1500\,nm$ is plotted against the data, see figure 5.12, an explanation for this becomes clear. The birefringence has a concavity that reduces the slope between the two points.

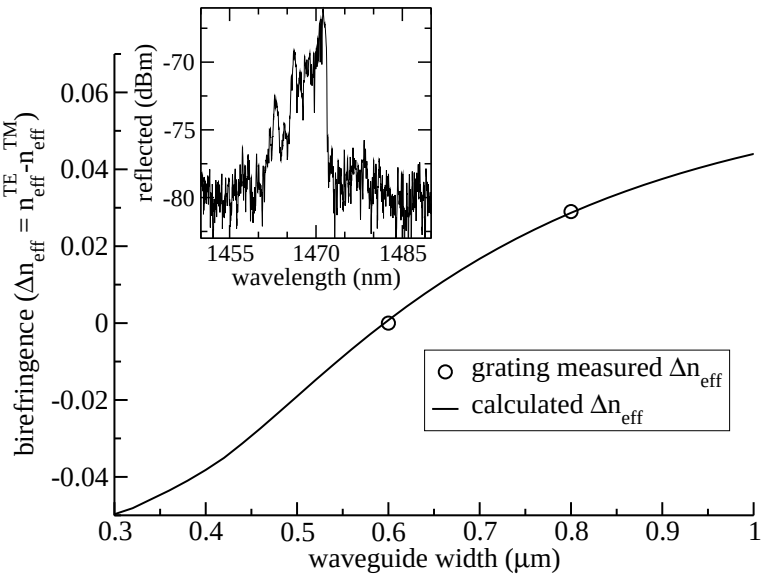

Figure 5.12: *Main graph:* The calculated birefringence plotted against the measured birefringence assuming that near degeneracy of the resonant wavelength for the $1.0\,\mu m$ wide (on mask) waveguide is an indication of cross-sectional geometric symmetry. *Inset graph:* the reflected spectrum of the $1.0\,\mu m$ wide waveguide.

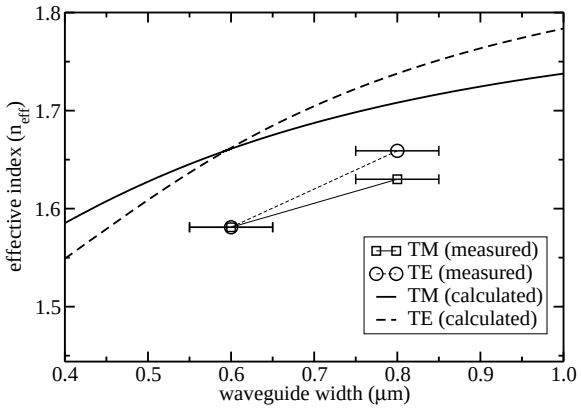

Figure 5.13: The calculated (at $1500\,nm$) effective index of the high index contrast waveguides plotted against the grating-measured effective indexes.

Inspection of figure 5.12 suggests that there is good agreement between calculated values and measured values. This is true in terms of the birefringence, but it is not true in terms of the values of the effective indexes. The effective indexes measured are lower than those calculated using the mode solvers - as was done in figure 3.4. The reason for this is not known, but it is a clear indication that the profile of the refractive index is not what is expected given the index measurements of the Si_xN_y film. Misalignment of the grating could result in a slight perturbation of the effective index, but a misalignment would result in an effectively longer grating period and the effective index is inversely proportional to the grating period (see equation 5.4). The calculated values and the measured values of the effective index are shown in figure 5.13.

Several observations imply that the grating was written in the cladding and not the waveguides themselves. First, the grating is clearly visible in the cladding when viewed through a microscope. This is shown in figure 5.14. The period of the grating visible in this picture is, however, twice what is expected. This phenomenon has been seen before [78].

To test the properties of the grating, the sample was heated on a hotplate at $150^\circ C$ for 1 hour and 30 minutes. After heating, the insertion loss of the waveguides were remeasured. This was repeated twice with an increased temperature of $300^\circ C$ and then $450^\circ C$. The results of the measurements are shown in figures 5.10 and 5.11 in succession from top to bottom. The grating experiences a dramatic reduction, all but vanishing after being heated at $450^\circ C$.

It is known from previous work that UV induced index changes in nitrogen doped silica glass are stable when heated to $450^\circ C$ [79]. This strongly suggests, along with the image of the grating in the cladding region, that the grating is in the germanium doped silica, which is known not to be stable at similar temperatures [80].

Another feature of interest is that as the gratings were weakened there is a steady shift of the resonance to shorter wavelengths. The reason for this is likely due to the reduction in the average effective index as the grating is weakened. This is also an indication that the grating is in the germanium doped region because the index changes reported in SiON and SiN have been negative [77,79], which would correspond to shifts to longer wavelengths as the gratings weakened (i.e. if as the gratings weakened the average effective index of the waveguides increased, then the shift would be to longer wavelengths). The average wavelength change, measured from the data displayed in figure 5.10, was $-1.2 \pm 0.1\, nm$. The average index change can be calculated by following equation 4.34, written in an abbreviated form for this situation:

$$\frac{\Delta n_{eff}}{n_g} = \frac{\Delta \lambda}{\lambda} \tag{5.6}$$

where n_{eff} is the effective index, n_g is the effective group index, $\Delta\lambda$ is the shift in wavelength, and λ is the wavelength. Following this calculation, assuming a wavelength of $1530\, nm$, and using a calculated value for the effective group index of 2.17 that assumes a linewidth reduction of $0.4\, \mu m$, the shift in the effective index is $n_{eff} = -1.7 \pm 0.2 \times 10^{-3}$. Again, it is noted that there is a negative shift in the effective index as the grating weakens.

A reflected spectrum from the grating was also measured. This is

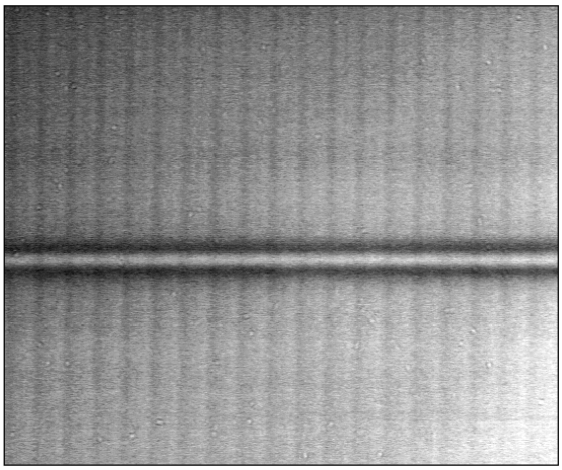

Figure 5.14: A picture of the cladding based UV-written grating for a high index waveguide. This is a strong indication that the grating is contained in the cladding layer.

shown in figure 5.12. The strength and definition of the reflected spectrum is not high, but the measurement of reflected spectra with high-index contrast waveguides that can have significant reflections at the interface to fibers can be problematic. What the spectrum shows is that there is actually a reflected signal, and there is a possibility this can be useful for practical devices. Finally, the shapes of the transmission spectra are somewhat erratic. This may be because the the effective index is highly sensitive to waveguide geometry (see equation 5.5) and small variations of waveguide dimensions may lead to a "smearing" of the resonance. More investigation is needed to determine if high quality gratings can be made using this technique.

5.7 Conclusion

The combination of a UV sensitive cladding region and high-index waveguides offers some possibilities for making hybrid devices. The direct coupling to high-index rings from UV-written waveguides has been demonstrated, but it is unclear whether this can lead to practical devices. Grating assisted coupling, or other methods to satisfy phase matching conditions, can be used to enhance performance, but attempts at doing so have not shown convincing success. One reason for this may be a difference in the expected and measured effective index demonstrated with the UV-written grating (see figure 5.13).

The UV-written grating may be used to characterize particular waveguides, giving an accurate measurement of the modal propagation characteristic that can then be used for phase matching. The grating can be easily removed by heating and should prove a useful tool for future research involving high-index waveguides. Directly UV-written waveguides can subsequently be written on the sample following reloading with D_2.

One area that is of special interest for future studies of the combination of UV waveguides and high-index waveguides is the use of high-index tapers to facilitate coupling. This is of particular interest for the $0.33\,\mu m$ thick silicon rich silicon nitride waveguides that displayed significantly lowered insertion losses when coupled to optical fiber.

Chapter 6

Non-linearities

The functionality of optical circuits that rely on a linear electric susceptibility is limited. In order to have all-optical switches, light must somehow interact with light and this means that the response of an optical circuit can't simply be a linear superposition of the inputs. Materials generally display some level of optical non-linearity, but since these nonlinear responses are often small compared to the linear response, exploitation of the nonlinearities usually require strong electric fields. Optical waveguides confine the light so that the electric field remains strong over a prolonged transmission length given a moderate input power, and this means that noticeable nonlinear effects are more easily achieved [36].

In this project, an attempt was made at quantifying the nonlinearities in silicon rich silicon nitride waveguides. The high modal confinement and the ability to make optical resonators opens the possibility of using small optical nonlinearities for optical switching. No functional nonlinear device was made, but measurements of the nonlinearities and the implications of these are assessed.

6.1 Nonlinearities

6.1.1 Basic

The polarization of a material is defined (following the scalar approximation and the conventions in reference [16]) as [1] :

$$\mathcal{P} = \epsilon_o \chi E + 2dE^2 + 4\chi^{(3)} E^3 \tag{6.1}$$

The electric field(E) and the electric displacement field (D) are related to each other with the relationship:

$$\begin{aligned} D &= \epsilon_o(E + \mathcal{P}) && (6.2)\\ &= \epsilon_o \left(E + \chi E + \frac{2d}{\epsilon_o} E^2 + \frac{4\chi^{(3)}}{\epsilon_o} E^3 + \cdots \right) && (6.3) \end{aligned}$$

where ϵ_o is the permittivity of free space. The silicon rich silicon nitride used to make the high-index waveguides is an amorphous material, as confirmed with X-ray diffraction measurements [29]. Amorphous materials display centrosymmetry (inversion symmetry) , having no directional preference. Therefore, the second order nonlinearity vanishes, $d = 0$ [81]. The first non-negligible nonlinear term is the third order susceptibility, $\chi^{(3)}$.

Measurements examined the change of effective refractive index of the ring resonator as a function of an applied D.C. electric field by tracking shifts of the resonant wavelengths as the applied electric field was changed. The electric field present can be expressed as $E = E_o + E_\omega$ [2], where E_o is the magnitude D.C. field, and E_ω is the amplitude of the electric field of the guided mode - varying at frequency ω. The polarization is given by:

[1] The nonlinear electric susceptibilities can more generally be written as a tensorial sum: $\mathcal{P}_i = \epsilon_o(\chi_{ij}E_j + \chi^{(2)'}_{ijk}E_jE_k + \chi^{(3)'}_{ijkl}E_jE_kE_l + \cdots)$, where a different definition for the susceptibilities ($\chi(2)'$ and $\chi(3)'$) has been used and is emphasized by primes labeling the χ terms.

[2] For simplicity the harmonic dependence of the E_ω field is not explicitly written.

$$\begin{aligned}
\mathcal{P} &= \epsilon_o \chi E + 4\chi^{(3)}(E_o + E_\omega)^3 && (6.4)\\
&= \epsilon_o \left(\chi E + 4\frac{\chi^{(3)}}{\epsilon_o} \left(E_o^3 + 3E_o^2 E_\omega + 3E_o E_\omega^2 + E_\omega^3 \right) \right) && (6.5)\\
&\approx \epsilon_o \left(\chi E_o + 4\frac{\chi^{(3)}}{\epsilon_o} E_o^3 \right) + \epsilon_o \left(\chi + 12\frac{\chi^{(3)}}{\epsilon_o} E_o^2 \right) E_\omega && (6.6)
\end{aligned}$$

where it has been assumed that magnitude of the fields in the guided mode are small with respect to the applied D.C. field, and that we are only interested guided modes with an angular frequency ω, so that only the linear term with respect to E_ω was kept. For the optical field, the second term defines the relative permittivity, ϵ_r, as function of the applied D.C. field. The refractive index is given by:

$$\begin{aligned}
n &= \sqrt{\epsilon_r} && (6.7)\\
&= \sqrt{(1+\chi) + 12\frac{\chi^{(3)}}{\epsilon_o} E_o^2} && (6.8)
\end{aligned}$$

Assuming that $\chi^{(3)}$ is small, this can be expanded in a Maclaurin series to give:

$$n = n_o + \frac{6E_o^2}{n_o \epsilon_o} \chi^{(3)} \qquad (6.9)$$

where it has been assumed that the change in the refractive index introduced by that application of the D.C. electric field is small compared to the value of the refractive index, $n_o = \sqrt{1+\chi}$. This basic expression is sometimes written in different forms:

$$\begin{aligned}
n &= n_o + \frac{1}{2} n_2^{DC} E_o^2 && (6.10)\\
&= n_o - \frac{1}{2} s n_o^3 E_o^2 && (6.11)
\end{aligned}$$

where $n_2^{DC} = \frac{12}{n_o \epsilon_o}\chi^{(3)}$ and $s = -\frac{12}{\epsilon_o n_o^4}\chi^{(3)}$. The term s is referred to as the Kerr coefficient and the change in the refractive index as a function of the applied field, E_o, is known as the D.C. Kerr effect.

A similar procedure can be used to derive the optical Kerr effect that happened when the intensity of the guided mode produces electric fields strong enough to cause a shift in the refractive index of the guiding medium. The derivation of this assumed the electric field is of the form $E = E_\omega \cos(\omega t)$. Where the time dependence of the electric field has been explicitly written. In a similar fashion as before, the polarization can be written:

$$\begin{aligned} \mathcal{P} &= \epsilon_o \chi E_\omega + 4\chi^{(3)} E_\omega^3 \cos^3(\omega t) && (6.12) \\ &= \epsilon_o \chi E_\omega + 3\chi^{(3)} E_\omega^3 \cos(\omega t) + \chi^{(3)} E_\omega^3 \cos(3\omega t) && (6.13) \end{aligned}$$

The efficiency with which the third, $3\omega t$, term is generated is generally low, and if the first two terms are considered, an expression for the refractive index can be derived:

$$\begin{aligned} n &= n_o + \frac{3}{2}\frac{\chi^{(3)}}{\epsilon_o n_o}|E_\omega|^2 && (6.14) \\ &= n_o - \frac{1}{8} s n_o^3 |E_\omega|^2 && (6.15) \end{aligned}$$

where the nonlinear terms have been assumed to be small compared to the initial refractive index and a Maclaurin series has been used. It should be noted that though s is used to provide some reference point when comparing it to equation 6.11, this does not exclude the possibility that s is a function of frequency. Equation 6.14 can also be written as:

$$n = n_o + \frac{n_2}{2}|E_\omega|^2 \qquad (6.16)$$

where

$$n_2 = \frac{6\chi^{(3)}}{\epsilon_o n_o} \qquad (6.17)$$

6.1.2 Resonance Shift

The resonance of a ring should change wavelength as the effective index of the ring resonator, and thus the resonant condition (equation 4.1), changes. The amount by which the resonance changes is given by equation 4.34. It must be emphasized that the change of index that is of interest is the change that occurs at a particular wavelength. The relationship for the shift in wavelength to the shift in effective index is given by:

$$\frac{\Delta n_{eff}}{n_g} = \frac{\Delta \lambda}{\lambda} \tag{6.18}$$

where Δn_{eff} is the change in the effective index at a given (and fixed) wavelength, n_g is the effective group index, λ is the wavelength of interest (e.g. the wavelength of the initial resonance), and $\Delta\lambda$ is the change in resonant wavelength caused by the application of the D.C. electric field.

6.2 Measurement

6.2.1 Method

The transmission of a straight silicon rich silicon nitride waveguide coupled to three ring resonators, each displaying one unique resonance within its FSR, was measured using an ANDO optical spectrum analyzer (OSA) synchronized with a tunable laser source (TLS) as illustrated in figure 6.1. On the top cladding, silver based conductive paint was used as an electrode for applying an electric field across one of the ring resonators. A high voltage power supply was connected to this electrode and the electrical ground was attached to the bottom side of the chip, directly to the silicon substrate on which the device was made. Polarization was adjusted to maximize the depth of the transmission dips corresponding to the resonant modes of the rings. A diagram of the set-up can be seen in figure 6.1, as can a characteristic cross section of the SRN waveguides.

Transmission spectra were gathered for selected resonances. Resonances of two of the three rings are shown in 6.2. A third resonance is

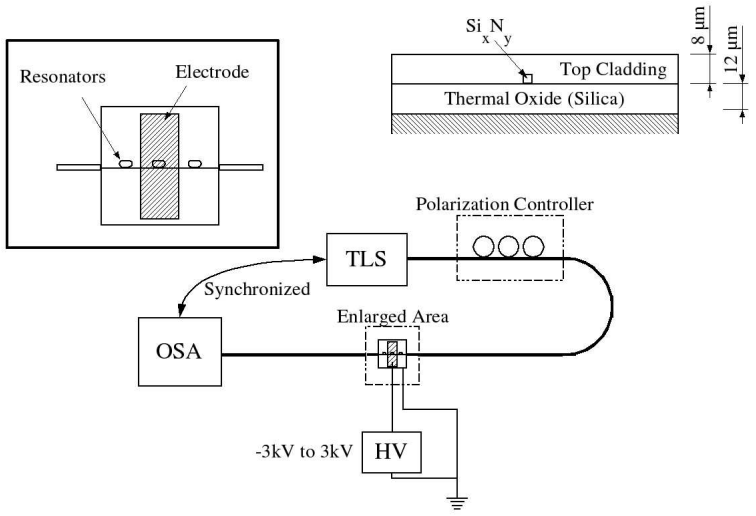

Figure 6.1: A high-level digram showing the set-up used for the measurement of the D.C. Kerr effect. An enlarged picture showing the placement of the electrodes and the rings is given, and the cross-section of the device is also shown with dimensions.

not shown and lies outside of the $1\,nm$ wavelength range displayed. Resonances for different rings were easily distinguishable because the free spectral range of the resonators was large enough (¿ 2nm) to exclude the possibility that resonances in a given wavelength range were from the same resonator. Spectra of the resonances were taken for each voltage applied to the electrodes. The applied voltage ranged from $-2512\,V$ to $2012\,V$. Each spectrum was systematically normalized and fit to Lorentzians corresponding to the resonances (transmission dips) of the rings. The relative positions of the peaks were extracted from the fits.

The relationship between effective refractive index shift of the ring and the shift in the resonance peak is given by equation 6.18. The first non-vanishing, nonlinear term was assumed to correspond to the Kerr effect described by equation 6.11.

The electric field was taken to be the applied voltage divided by the

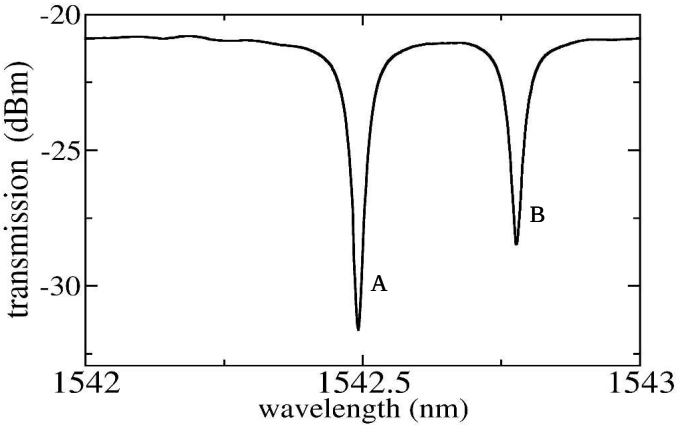

Figure 6.2: A typical transmission spectrum of the straight waveguide coupled to rings used for the measurement of non-linearities. Resonance dip B moved with the application of an electric field. Resonance dip A remained stationary. The difference in the position of these peaks were used to determine wavelength shifts. A third resonance, also stationary with the application of an electric field, is not shown and lies outside of the spectral range displayed.

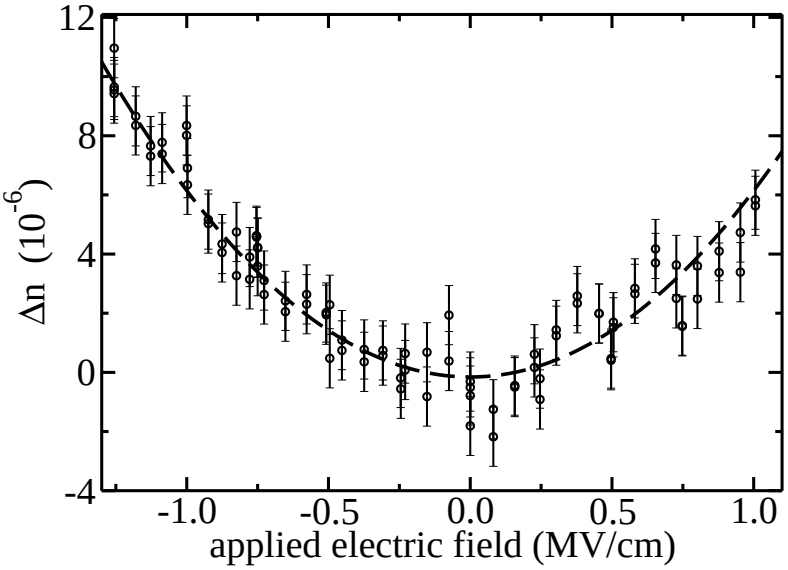

Figure 6.3: The change in effective index as a function of the applied electric field.

sum of the thicknesses of the thermal oxide and top cladding layers - though the variation in permittivity makes the electric field distribution more complex. Since shifts in the resonances correspond to shifts in the waveguide's effective index and not the change of the material's index directly, the model above serves as a guideline for defining an effective Kerr coefficient.

6.2.2 Results

To calculate the Kerr coefficient, some values must be derived. The first is the effective group index which is easily extracted from the free spectral range of the resonators (see equation 4.10). The free spectral range was found to be $2.101 \pm 0.002\,nm$ which, for the rings measured, corresponds to an effective group index of 2.07. The second value needed is the effective refractive index of the waveguides. To obtain this, the effective group index of a silicon rich silicon nitride waveguide was calculated numerically (assuming a rectangular geometry) for a narrow range of waveguide widths. The effective refractive index was then calculated for the waveguide width at which the effective group index corresponded to that obtained from the FSR.

Using equation 6.18, shifts in the wavelength of resonance can be used to calculate the change in effective index due to the application of an electric field. The results are shown in figure 6.3. The magnitude of the maximum wavelength shift observed was on the order of $10\,pm$.

A parabola fit to the data, shown in figure 6.3, yields a Kerr coefficient of $s = -3.0 \pm 0.1 \times 10^{-22} m^2 V^{-2}$. This value reflects the variation in the effective refractive index as a function of an applied DC voltage for one polarization. The polarization measured was assumed to be TE. Since high index contrast fibers were used to reduce coupling loss to the silicon rich silicon nitride waveguides, the polarization launched into the waveguides could not be guaranteed (subsequent measurements with a standardized sample have, however, confirmed it was the TE polarization). Both polarizations were not measured because peaks must be sharp and the resonances corresponding to different rings must be well separated. Since high-index contrast coupling structures are inherently birefringent,

the optimum coupling required for sharp peaks at both polarizations was not achieved.

6.3 Applications

Optical bistability is mentioned here because of it's significance for the creation of optical memory, its relevance to nonlinearities and the possibility of exploiting non-linearities in optical resonators. The basic behavior of optical bistability can be derived from taking the differential equations describing ring resonator modes coupled in time and adding a nonlinear term in the definition of the refractive index. To define the nonlinear change in the refractive index, it is noted that:

$$\frac{\Delta n}{n_g} = -\frac{\Delta \omega}{\omega} \tag{6.19}$$

This follows directly from equation 6.18 with the definition of the angular frequency, $\omega = 2\pi c/\lambda$. To simplify analysis, equation 4.46 is manipulated assuming that the bulk ring mode amplitude, $h(t)$, and the driving signal, $A_i(t)$, can be expressed as:

$$h(t) = h_s(t)e^{i\omega t} \tag{6.20}$$

$$A_i = Ae^{i\omega t} \tag{6.21}$$

where A is the driving amplitude, and $h_s(t)$ is the ring energy in the time domain with the driving frequency divided out. The resulting differential equation is:

$$\frac{\partial}{\partial t}h_s = i(\omega_o + \Delta\omega - \omega)h_s - \frac{1}{\tau}h_s - i\mu A \tag{6.22}$$

where $\Delta\omega$ is the change in the resonant frequency which is proportional to the energy in the ring, h^*h. To derive this, the power density is recalled from equation 4.44. Furthermore, the power density is related to the amplitude of the electric field. To do this, an expression of the power carried in the core the waveguide is [36]:

$$\alpha |H|^2 = \frac{1}{2} \int_{core} \boldsymbol{E} \times \boldsymbol{H} dx\, dy = \frac{\beta}{2\mu_o \omega} \int_{core} E^2 dx\, dy \tag{6.23}$$

Where $|H|^2$ is the power carried in the waveguide, α is defined as the fraction of the guided power carried in the core, β is the propagation constant of the mode, μ_o is the permeability of free space, ω is the angular frequency, and the integral is taken over the core of a waveguide that is aligned with an optical axis parallel to the z-axis. For simplicity, the average electric field is considered for a waveguide with a core area of a. This gives the relationship:

$$|E|^2 = \frac{2\alpha\mu_o\omega}{\beta a} |H|^2 \tag{6.24}$$

$$= \frac{2\alpha\mu_o\omega v_g}{L\beta a} |h|^2 \tag{6.25}$$

Where L is the length around the ring, and v_g is the group velocity. This expression can be used with equations 6.16 and 6.19 to give an estimate for $\Delta\omega$ as a function of $|h|^2$. Noting the relationships: $v_g = c/n_g$, $\omega = 2\pi c/\lambda$, $\beta = n_{eff} 2\pi/\lambda$ and $c^2 = 1/(\epsilon_o \mu_o)$, equation 6.25 can be rewritten:

$$|E|^2 = \frac{2\alpha}{\epsilon_o a n_g n_{eff} L} |h|^2 \tag{6.26}$$

Equilibrium can be found by setting the time derivative of $h_s(t)$ to zero and calculating the energy of the resonator:

$$\frac{h_s^* h_s}{A^* A} = \frac{\mu^2}{(\omega_o + \Delta\omega - \omega)^2 + 1/\tau^2} \tag{6.27}$$

Which is a transcendental equation since, after some algebraic manipulation:

$$\Delta\omega = \frac{1}{4} s \frac{n_o^2 \alpha \omega_o}{\epsilon_o a n_g^2 L} |h|^2 \tag{6.28}$$

This gives the basic tools with which (bi)stability can be explored. Basic techniques for this are covered in references [16, 36]. The coupling of modes in time can also be used to analyze multiple ring structures in a similar fashion, though multiple ring structures may display chaotic behavior.

6.4 Conclusion

Nonlinear behavior is essential for making active optical components such as all-optical switches and optical memory. The future (or perhaps versatility) of any optical processing platform probably relies upon its ability to use these effects with low optical power. High-index contrast waveguides provide high optical confinement, and make optical nonlinearities more easily exploitable.

The DC Kerr effect has been measured by tracking shifts in the resonant wavelengths of a ring resonator. This is the beginning of a more detailed study moving toward useful optical devices. The advantages of the method used include simplicity and direct measurement of nonlinear device behavior. The disadvantages include the inability to separate out other possible causes for resonant shifts such as electrostriction [82].

Chapter 7

Conclusion

The ability of high-index contrast waveguides to make tight, low-loss bends increases the achievable packing density of integrated optical components, and can be used to make ring resonators with large free spectral ranges. This is a major improvement for the conceptual simplicity of channel selecting filters and possibility of making large scale, highly-integrated optical filters. There are, however, major obstacles. There are extreme polarization effects that indicate that for all but the most simple components, the polarizations will likely need to be split, processed in parallel and recombined if significant signal losses are to be avoided. More than this, the tolerances for device fabrication are so tight that any commercially viable processing technique is daunting in terms of expected device yield.

Some aspects of the material processing have been discussed - most notably the annealing of LPCVD deposited silicon rich silicon nitride to reduce material-based loss, and the lithographic limitations of the processing used. The fundamental properties of high-index contrast waveguiding and ring resonators have been explained. Again, the polarization not only displays extreme geometrically induced effects on the effective index of the modes, but also on bend loss and coupling. Since ring resonators rely upon these properties to define their optical responses, the basis of polarization problems has been described.

One of the possibilities explored during this project was the combina-

tion of UV-sensitive material and high-index contrast waveguides. The benefits of this include the incorporation of two types of waveguides onto a monolithic device with minimal additional cleanroom work, and the ability to use the UV-sensitivity for making other devices such as gratings. It may also be useful for trimming the performance of high-index contrast devices.

Coupling has been demonstrated between high-index rings and UV-written waveguides. The benefits of this direct approach for coupling remain unclear, but the relative uniformity of the resonant responses for the different polarization when using "configuration 2" (see figure 5.3) warrant more investigation for practical devices. Even if the resonances are not coincident, they are similar enough in width and free spectral range to hint at polarization independent function.

One major obstacle for any amorphous, glass-based material platform is nonlinear optical functionality that might lead to optical switching. The obvious candidate for providing this functionality is the Kerr effect. High-index contrast waveguides provide high optical confinement (and thus high electric fields) which makes exploitation of these effects easier than with low-index contrast waveguides. Still, the effects are generally too small to exploit in low power devices. Material development will probably be the key, but it should be noted that other possibilities remain. The electric field of the guided mode at the boundary of a high-index contrast waveguide can be high because of dicontinuities in the component of the electric field that is perpendicular to the interface. This high field outside the core means that cladding high-index waveguides with optically nonlinear material (e.g. some polymers) could be promising.

In the end, the vision is that silicon rich silicon nitride waveguides will be the basis of a widely accepted and commercially viable platform for integrated optics. Silicon rich silicon nitride chips (such as those shown in figure 7.1) could be distributed throughout the global communications network. The eventual reality is probably far from this. There are many competing planar technologies such as photonic bandgap (PBG) devices or SOI waveguides that also offer impressive benefits. These do, however, have significant disadvantages when compared to silicon rich silicon nitride. One of the disadvantages involves processing tolerances. The

tolerances for silicon rich silicon nitride waveguides are tight, no doubt, but the tolerances for SOI waveguides are much higher. The structure of classical high-index contrast waveguides are also much simpler than photonic bandgap waveguides and simplicity in some sense is related to robustness and practical applications.

I believe my major contributions to the advancement of the technology has included the demonstration of functional single layer silicon rich silicon nitride components. This includes measurement of bending losses and demonstration of a decreased insertion loss associated with particular waveguide geometries (notably the $0.33\,\mu m$ thick silicon rich silicon nitride waveguides). The approach for making optical filters has also been successful given the processing constraints. Beyond this, I have shown successful monolithic integration of directly UV-written waveguides and high index waveguides. Many avenues remain to be explored here, but number of possibilities beyond direct coupling to ring resonators have been suggested. The recent development of the UV-written cladding grating also offers a tool for directly measuring high-index waveguide properties that was previously available and I think greatly simplifies evaluation of device performance, as well as raising important questions about how well we know the structures being measured. I have also done work on optical nonlinearities by using the spectral properties of ring resonators to measure the D.C. Kerr effect. This field is of course broad and interesting in itself.

7.1 Future Research

The first problem that must be addressed is polarization dependence. The extreme geometric effects actually allow for a great amount of control over polarization behavior. The challenge is to make polarization control a broad-band effect. An example of a broad band polarization rotator is an asymmetric waveguide core, twisted in an adiabatic helical shape (figure 7.2) until a 90° rotation is achieved. The extreme birefringence means there is little coupling between the modes (because of phase mismatch). The disadvantage is, of course, that this is not easily made with planar technology. There has, however, been work on approximating

Figure 7.1: A photograph of high-index silicon rich silicon nitride devices diced into chips from a 4-inch wafer. Each chip is $15\,mm \times 8\,mm$.

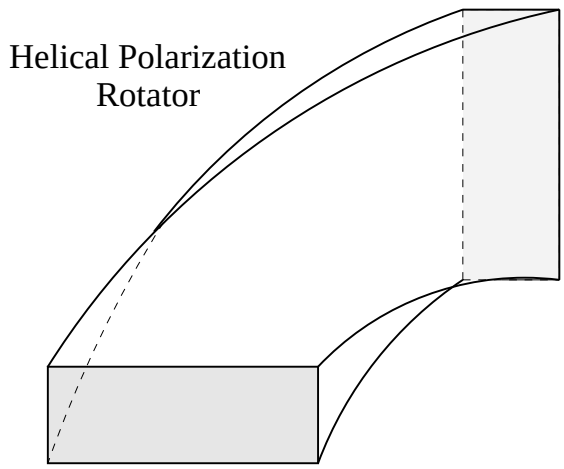

Figure 7.2: A conceptual helical waveguide polarization converter.

this with discrete multi-layer structures [83], this general work extends beyond polarization rotators to include polarization splitters. These devices are promising because of the conceptual simplicity and broad-band behavior of these devices.

Other areas of research must include making the devices active, producing standardized procedures for the interface to optical fiber (e.g. inverted tapers), and improving process repeatability/device yield. Improving device yield may require a re-examination of processing techniques and exploring alternative lithographic processes such as Nano-imprint Lithography (NIL). Beyond this, there should be a focus on testing these devices in practical network situations.

Ultimately, a full integrated optical platform is envisioned such as that shown in figure 7.3.

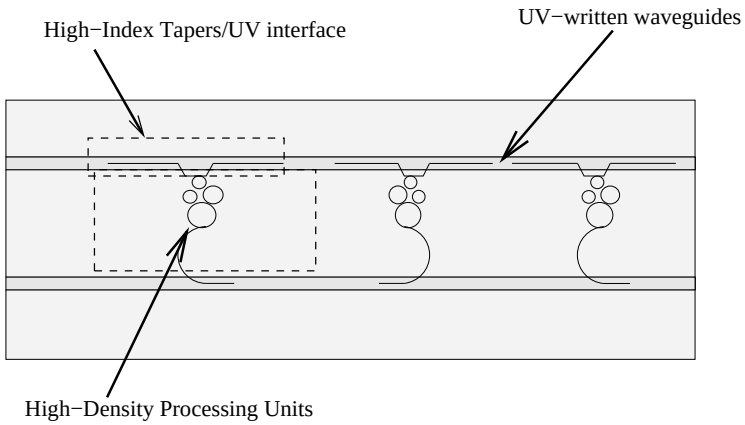

Figure 7.3: A possible high-level view of a high-index contrast platform. The high-density optical processing could have several subunits with inputs and outputs being from directly written UV waveguides. The functionality of the high-density optical waveguides would have to include polarization and dispersion compensation devices.

Appendix A

Wave Equation

Starting with equation 3.4 and taking the curl of both sides:

$$\boldsymbol{\nabla} \times \boldsymbol{\nabla} \times \boldsymbol{E} + \frac{\partial}{\partial t} \boldsymbol{\nabla} \times \boldsymbol{B} = 0 \tag{A.1}$$

applying the constitutive relationship $\boldsymbol{B} = \mu \boldsymbol{H}$:

$$\boldsymbol{\nabla} \times \boldsymbol{\nabla} \times \boldsymbol{E} + \frac{\partial}{\partial t} (\boldsymbol{\nabla} \mu \times \boldsymbol{H}) + \frac{\partial}{\partial t} (\mu \boldsymbol{\nabla} \times \boldsymbol{H}) = 0 \tag{A.2}$$

noting that $\boldsymbol{\nabla} \times \boldsymbol{H} = \frac{\partial}{\partial t} \boldsymbol{D}$, $\boldsymbol{D} = \epsilon \boldsymbol{E}$; assuming that μ and ϵ are not functions of time; and assuming that μ is constant throughout the material under consideration:

$$\boldsymbol{\nabla} \times \boldsymbol{\nabla} \times \boldsymbol{E} + \mu \epsilon \frac{\partial^2}{\partial t^2} \boldsymbol{E} = 0 \tag{A.3}$$

Now, using the vector identity $\boldsymbol{\nabla} \times \boldsymbol{\nabla} \times \boldsymbol{E} = -\boldsymbol{\nabla}^2 \boldsymbol{E} + \boldsymbol{\nabla} (\boldsymbol{\nabla} \cdot \boldsymbol{E})$:

$$\boldsymbol{\nabla}^2 \boldsymbol{E} - \mu \epsilon \frac{\partial^2}{\partial t^2} \boldsymbol{E} - \boldsymbol{\nabla} (\boldsymbol{\nabla} \cdot \boldsymbol{E}) = 0 \tag{A.4}$$

noting again that $\boldsymbol{D} = \epsilon \boldsymbol{E}$:

$$\boldsymbol{\nabla}^2 \boldsymbol{E} - \mu \epsilon \frac{\partial^2}{\partial t^2} \boldsymbol{E} - \boldsymbol{\nabla} (\boldsymbol{D} \cdot \boldsymbol{\nabla} \frac{1}{\epsilon} + \frac{1}{\epsilon} \boldsymbol{\nabla} \cdot \boldsymbol{D}) = 0 \tag{A.5}$$

recalling Gauss' law, $\boldsymbol{\nabla} \cdot \boldsymbol{D} = 0$, the last term on the left hand side vanishes. Also, noting that $\boldsymbol{\nabla}(\ln \frac{1}{\epsilon}) = \epsilon \boldsymbol{\nabla}(\frac{1}{\epsilon})$:

$$\boldsymbol{\nabla}^2 \boldsymbol{E} - \mu\epsilon \frac{\partial^2}{\partial t^2} \boldsymbol{E} - \boldsymbol{\nabla}(\boldsymbol{E} \cdot \boldsymbol{\nabla} \ln \frac{1}{\epsilon}) = 0 \tag{A.6}$$

noting further that $\epsilon = \epsilon_o \epsilon_r$ and that $\epsilon_r = n^2$:

$$\boldsymbol{\nabla}^2 \boldsymbol{E} - \mu\epsilon \frac{\partial^2}{\partial t^2} \boldsymbol{E} - \boldsymbol{\nabla}(\boldsymbol{E} \cdot \boldsymbol{\nabla}(\ln \frac{1}{\epsilon_o} + \ln \frac{1}{n^2})) = 0 \tag{A.7}$$

$$\boldsymbol{\nabla}^2 \boldsymbol{E} - \mu\epsilon \frac{\partial^2}{\partial t^2} \boldsymbol{E} - 2\boldsymbol{\nabla}(\boldsymbol{E} \cdot \boldsymbol{\nabla}(\ln \frac{1}{n})) = 0 \tag{A.8}$$

finally:

$$\boldsymbol{\nabla}^2 \boldsymbol{E} - \mu\epsilon \frac{\partial^2}{\partial t^2} \boldsymbol{E} = -2\boldsymbol{\nabla}(\boldsymbol{E} \cdot \boldsymbol{\nabla}(\ln n)) \tag{A.9}$$

Appendix B

Bending

In cylindrical coordinates, the Laplacian operator can be written as:

$$\boldsymbol{\nabla}^2 = \frac{1}{r}\frac{\partial}{\partial r} + \frac{\partial^2}{\partial r^2} + \frac{1}{r^2}\frac{\partial^2}{\partial \phi^2} + \frac{\partial^2}{\partial y^2} \tag{B.1}$$

A local reference frame can be defined centered on the waveguide with the definitions:

$$r = r_b + x \tag{B.2}$$

$$\phi = \frac{z}{r_b} \tag{B.3}$$

The Laplacian then becomes:

$$\boldsymbol{\nabla}^2 = \frac{1}{r_b + x}\frac{\partial}{\partial x} + \frac{\partial^2}{\partial x^2} + \frac{\partial^2}{\partial y^2} + \frac{r_b^2}{(r_b + x)^2}\frac{\partial^2}{\partial z^2} \tag{B.4}$$

The Helmholtz equation associated with the wave equation for the waveguide can be written as:

$$\left(\boldsymbol{\nabla}^2 + \kappa^2\right) E = 0 \tag{B.5}$$

$$\left(\frac{1}{r_b + x}\frac{\partial}{\partial x} + \frac{\partial^2}{\partial x^2} + \frac{\partial^2}{\partial y^2} + \frac{r_b^2}{(r_b + x)^2}\frac{\partial^2}{\partial z^2} + \kappa^2\right) E = 0 \tag{B.6}$$

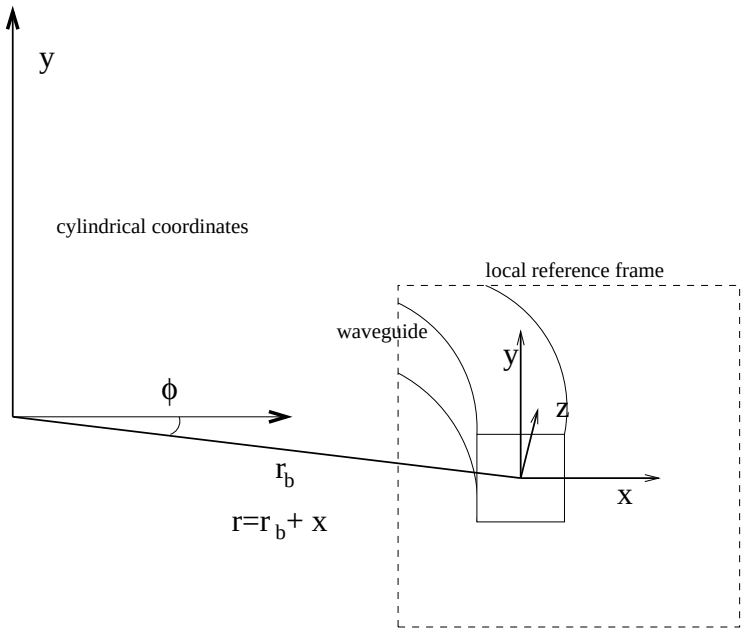

Figure B.1: The local coordinates used for tranforming the Laplacian for curved waveguides.

A further substitution for the E is made, assuming the form:

$$E = g(x)E_o e^{-i\beta z} \tag{B.7}$$

Plugging this form into equation B.6, the following expression is obtained:

$$\left(\frac{\partial^2}{\partial y^2} - \frac{r_b^2}{(r_b+x)^2}\beta^2 + \kappa^2\right) g\,E_o + g''\,E_o + 2g'\,E_o' + g\,E_o'' + \frac{1}{r_b+x}g'E_o + \frac{1}{r_b+x}gE_o' = 0 \tag{B.8}$$

to determine $g = g(x)$, the terms containing E_o' are required to vanish, i.e.:

$$2g' = -\frac{1}{r_b+x}g \tag{B.9}$$

this is easily solved by integration:

$$\frac{1}{g}dg = \frac{-1}{2\,(r_b+x)}dx \tag{B.10}$$

Which yields:

$$g = (r_b+x)^{-1/2} \tag{B.11}$$

where constants associated with integration have been chosen to equal zero. Plugging this result back into equation B.8, the following expression is obtained:

$$g\left(\frac{\partial^2}{\partial x^2} + \frac{\partial^2}{\partial y^2}\right) E_o - g\frac{r_b^2}{(r_b+x)^2}\beta^2 E_o + \kappa^2 E_o + \frac{1}{4}g^5 E_o = 0 \tag{B.12}$$

Equation B.12 can be divided by g and if the radius is large compared to wavelength and waveguide dimensions, the terms containing g^4 may be ignored for he first approximation. This yields:

$$\left(\frac{\partial^2}{\partial x^2} + \frac{\partial^2}{\partial y^2} + k_o^2 n^2\right) E_o = \frac{r_b^2}{(r_b+x)^2}\beta^2 E_o \tag{B.13}$$

where κ has been replaced with $k_o n$, where k_o is the free space propagation constant and n is the refractive index profile. The right had side of the equation can be expanded about $x = 0$ in to yield (to the linear term):

$$\frac{r_b^2}{(r_b + x)^2}\beta^2 \approx \beta^2 - \beta^2 \frac{2}{r_b} x \tag{B.14}$$

Plugging this back into equation B.13, the following is obtained:

$$\left(\frac{\partial^2}{\partial x^2} + \frac{\partial^2}{\partial y^2} + k_o^2 \left(n^2 + \frac{2}{r_b} x n_{eff}^2\right)\right) E_o = \beta^2 E_o \tag{B.15}$$

At this point, the effective index is usually approximated by the index of the core. This is roughly valid low index contrast waveguides because there is only a very small range of possible effective indexes a propagating mode can have (between the core and cladding index). The same can be done for high index waveguides while noting that it represents a worst case scenario because the core index can be significantly larger than the effective index. This corresponds to a larger perturbation on the mode of a straight waveguide.

Appendix C

Additional Spectrum

One of the emphasized point in the body of the thesis was that there can be a significant difference in the properties of guided modes in high-index contrast waveguides having different polarizations. As further reference, an example spectrum of a ring is shown here. The free spectral range for the different polarizations differ slightly. This causes a coincidence of resonances at $\approx 1520\,nm$, and a divergence for longer and shorter wavelengths. This is typical behavior.

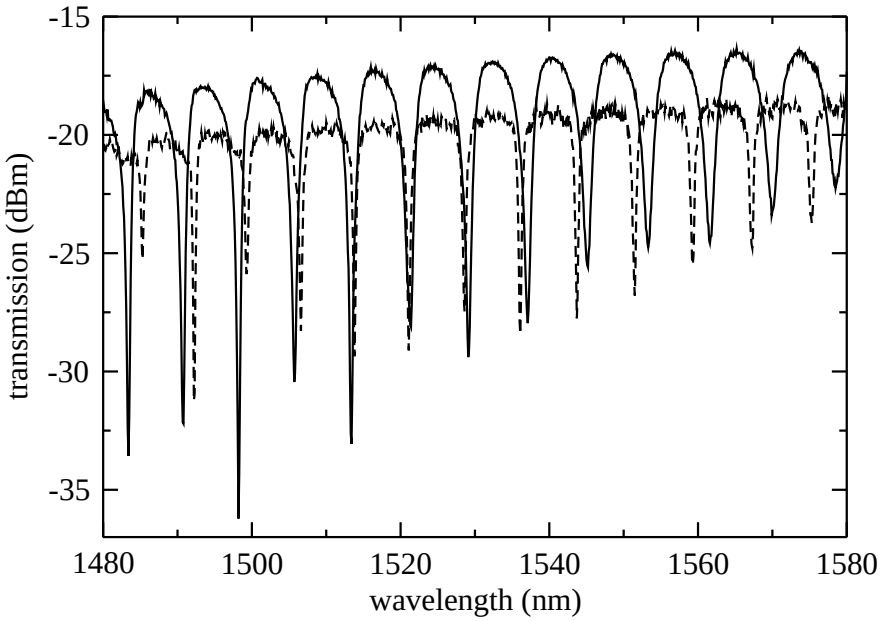

Figure C.1: Transmission spectrum of two polarizations from a $25\,\mu m$ radius ring. The waveguide is $0.33\,\mu m$ thick and $1.0\,\mu m$ wide (as defined on the mask). The different polarizations have different free spectral ranges.

Bibliography

[1] S. E. Miller, "Integrated optics: an introduction," *Bell System Technical Journal*, July-August 1969.

[2] E. A. J. Marcatili, "Dielectric rectangular waveguide and directional coupler for integrated optics," *Bell System Technical Journal*, pp. 2071–2102, September 1969.

[3] E. A. J. Marcatili, "Bends in optical dielectric waveguides," *Bell System Technical Journal*, pp. 2103–2132, September 1969.

[4] L. Eldada, "Advances in telecom and datacom optical components," *Optical Engineering*, vol. 40, pp. 1165–78, July 2001.

[5] D. Blumenthal, J. Bowers, L. Rau, H.-F. Chou, S. Rangarajan, W. Wang, and K. Poulsen, "Optical signal processing for optical packet switching networks," *IEEE Communications Magazine*, vol. 41, no. 2, 2003.

[6] M. Dhodhi, S. Tariq, and K. Saleh, "Bottlenecks in next generation dwdm-based optical networks," *Computer Communications*, vol. 24, no. 17, 2001.

[7] T. Miya, "Silica-based planar lightwave circuits: passive and thermally active devices," *IEEE J. on Selected Topics in Quant. Electron.*, vol. 6, no. 1, pp. 38 –45, 2000.

[8] K. Hill and G. Meltz, "Fiber bragg grating technology fundamentals and overview," *Journal of Lightwave Technology*, vol. 15, no. 8, pp. 1263–76, 1997.

[9] E. Desurvire, J. Simpson, and P. Becker, "High-gain erbium-doped traveling-wave fiber amplifier," *Optics Letters*, vol. 12, no. 11, 1987.

[10] G. P. Agrawal, *Fiber Optic Communication Systems*. John Wiley & Sons, Inc., 2nd ed., 1997.

[11] L. Lixia, G. Nordin, J. English, and J. Jiang, "Small-area bends and beamsplitters for low-index-contrast waveguides," *Optics Express*, vol. 11, no. 3, 2003.

[12] G. P. Nordin, J. Jiang, S. Kim, and J. Cai, "Micro-genetic algorithm-based design of combined conventional waveguide and photonic crystal devices," *Proceedings of SPIE - The International Society for Optical Engineering*, vol. 5000, 2003.

[13] C. K. Madsen and J. H. Zhao, *Optical Filter Design and Ananlysis*. John Wiley & Sons, Inc., 1999.

[14] K. K. Lee, D. R. L., L. Kimberling, J. Shin, and F. Cerrina, "Farbication of ultralow-loss Si/SiO_2 waveguides by roughness reduction," *Optics Letters*, vol. 26, no. 23, 2001.

[15] B. E. Little, S. T. Chu, H. A. Haus, J. Foresi, and J.-P. Laine, "Microring resonator channel dropping filters," *J. of Lightwave Technol.*, vol. 15, no. 6, 1997.

[16] B. E. A. Saleh and M. C. Teich, *Fundamentals of Photonics*. John Wiley & Sons, Inc., 1991.

[17] E. Cortesi, F. Namavar, and R. Soref, "Novel silicon-on-insulator structures for silicon waveguides," *IEEE SOS/SOI Technology Conference*, 1989.

[18] B. Little, J. Foresi, G. Steinmeyer, E. Thoen, S. Chu, H. Haus, E. Ippen, L. Kimerling, and W. Greene, "Ultra-compact $Si - SiO_2$ microring resonator optical channel dropping filters," *IEEE Photonics Technology Letters*, vol. 10, no. 4, pp. 549 –551, 1998.

[19] M. Lawrence, "Lithium niobate integrated optics," *Reports on Progress in Physics*, vol. 56, no. 3, pp. 363–429, 1993.

[20] D. Rabus, M. Hamacher, and H. Heidrich, "Active and passive microring resonator filter applications in gainasp/inp," in *International Conference on Indium Phosphide and Related Materials (IPRM)*, vol. 13, pp. 477–480, 2001.

[21] K. de Ridder, R.M.and Warhoff, A. Driessen, P. Lambeck, and H. Albers, "Silicon oxynitride planar waveguiding structures for application in optical communication," *EEE Journal on Selected Topics in Quantum Electronics*, vol. 4, no. 6, pp. 930 –937, 1998.

[22] B. Booth, "Low loss channel waveguides in polymers," *Journal of Lightwave Technology*, vol. 7, no. 10, pp. 1445 –1453, 1989.

[23] R. Ramaswamy and R. Srivastava, "Ion-exchanged glass waveguides: a review," *Journal of Lightwave Technology*, vol. 6, no. 6, 1988.

[24] V. Red'ko, A. Tomov, L. Shteingart, G. Kukankov, and A. Mal'ko, "Buried planar waveguides formed by proton bombardment of quartz glass," *Zhurnal Tekhnicheskoi Fiziki*, 1991.

[25] M. Svalgaard, C. Poulsen, A. Bjarklev, and O. Poulsen, "Direct uv writing of buried singlemode channel waveguides in ge-doped silica films," *Electronics Letters*, vol. 30, no. 17, pp. 1401 –1403, 1994.

[26] H. Mertens, "Silicon rich nitride (srn) for optical waveguide applications," Master's thesis, technische universiteit eindhoven, 2002.

[27] K. N. Andersen, P. C. Nielsen, and W. Svendsen, "Silicon rich nitride thin films and waveguides," in *IPR technical digest*, 2002.

[28] M.-C. Cheng, C.-P. Chang, W.-S. Huang, and R.-S. Huang, "Ultralow-stress silicon-rich nitride films for microstructure fabrication," *Sensors and Materials*, vol. 11, no. 6, pp. 349–58, 1999.

[29] K. N. Andersen, "personal correspondance.." Measurements performed by K.N. Andersen.

[30] H. Mertens, W. E. Svendsen, K. Andersen, and H. T. Philipp, "Optical loss analysis of silicon rich nitride waveguides," in *Danish Physical Society Annual meeting, abstract no. FF70P*, 2002.

[31] F. Tan, D. Klunder, H. Kelderman, H. Hoekstra, and A. Driessen, "High finesse vertically coupled waveguide-microring resonators based on si/sub 3/n/sub 4/-sio/sub 2/ technology," *Proceedings of 2002 IEEE/LEOS Workshop on Fibre and Optical Passive Components*, 2002.

[32] T. Barwicz, M. A. Popovic, P. T. Rakich, M. R. Watts, H. A. Haus, E. P. Ippen, and H. I. Smith, "Microring-resonator-based add-drop filters in sin: Fabrication and analysis," *Optics Express*, vol. 12, no. 7, 2004.

[33] F. Ladouceur and J. D. Love, *Silica-based Buried Channel Waveguides and Devices*. Chapman & Hill, 1996.

[34] M. Born and E. Wolf, *Principles of Optics: Electromagnetic Theory of Propagation, Interference and Diffraction of Light*. Cambridge University Press, 1999.

[35] J. D. Jackson, *Classical Electrodynamics*. John Wiley and Sons, 3 ed., 1998.

[36] K. Okamoto, *Fundamentals of Optical Waveguides*. San Diego: Academic Press, 2000.

[37] M. Lohmeyer, "Vectorial wave-matching mode analysis of integrated optical devices," *Optical and Quantum Electronics*, vol. 30, pp. 385–396, May 1998.

[38] A. Melloni, F. Carniel, R. Costa, and M. Martinelli, "Determination of bend mode characteristics in dielectric waveguides," *Journal of Lightwave Technology*, vol. 19, no. 4, pp. 571 –577, 2001.

[39] H. Fukuda, T. Tsuchizawa, K. Yamada, T. Watanabe, M. Takahashi, J. Takahashi, and S. Itabashi, "Silicon wire waveguides and their application for microphotonic devices," *IPR 2004 proceedings*, 2004.

[40] V. R. Almeida, R. R. Panepucci, and M. Lipson, "Nanotaper for compact mode conversion," *Optics Letters*, vol. 28, no. 15, pp. 1302–1304, 2003.

[41] R. Syms and J. Cozens, *Optical Guided Waves and Devices*. McGraw-Hill, 1992.

[42] A. W. Snyder and D. L. Love, *Optical Waveguide Theory*. Chapman & Hall, 1983.

[43] P. Reinhold, "The method of lines for the analysis of dielectric waveguide bends," *J. of Lightwave Tech.*, 1996.

[44] W. J. Song and B. Ahn, "Bending loss analysis of te and tm polarized fields in planar lightwave circuits," *IEEE International Symposium on Circuits and Systems, 2002. ISCAS 2002*, 2002.

[45] *OlympiOs Integrated Optics Software Manual*, 5.0 ed.

[46] K. S. Chiang, "Performance of the effective-index method for the analysis of dielectric waveguides," *Optics Letters*, vol. 16, no. 10, pp. 714–716, 1991.

[47] F. Abd Rahman, K. Takahashi, and C. Hean Teik, "A scheme to improve the coupling efficiency and working distance between laser diode and single mode fiber," *Optics Communications*, 2002.

[48] J. Hübner, D. Zauner, and M. Kristensen, "Low cross talk planar multichannel add-drop multiplexer based on sampled bragg gratings," *OFC '98 Optical Fiber Communication Conference OSA Technical Digest Series. Vol.2*, 1998.

[49] C. David, D. Wiesmann, R. Germann, F. Horst, B. Offrein, R. Beyeler, H. Salemink, and G. Bona, "Apodised bragg gratings in planar waveguides for add-drop filters," *Microelectronic Engineering*, 2001.

[50] C. Manolatou, M. J. Khan, S. Fan, V. P. R., H. A. Haus, and Joannopoulos, "Coupling of modes analysis of resonant channel

add-drop filters," *IEEE Journal of Qunatum Electronics*, vol. 35, pp. 1322–1331, September 1999.

[51] J. Hryniewicz, P. Absil, B. Little, R. Wilson, L. Joneckis, and P.-T. Ho, "Microring resonator notch filters," *CLEO 2000*, vol. 39, 2000.

[52] C. K. Madsen and G. Lenz, "Optical all-pass filters for phase response design with applications for dispersion compensation," *IEEE Photon. Technol. Lett.*, vol. 10, no. 7, 1998.

[53] G. B. Arfken and H. J. Weber, *Mathematical methods for physicists*. Academic Press, 4th ed., 1995.

[54] M. Abramowitz and I. A. Stegun, *Handbook of Mathematical Functions With Formulas, Graphs and Mathematical Tables*. John Wiley & Sons Inc, 1993.

[55] E. W. Weisstein, "treasure-troves of science."

[56] G. Lenz, B. Eggleton, C. Giles, C. Madsen, and R. Slusher, "Dispersive properties of optical filters for wdm systems," *IEEE Journal of Quantum Electronics*, vol. 34, no. 8, 1998.

[57] H. Takahashi, P. Carlsson, K. Nishimura, and M. Usami, "+/- 1350 ps/nm tuning demonstration of tunable chromatic dispersion compensator based on silica waveguide ring resonator with symmetric mzi coupler," *IPR 2003*, pp. IMC4–1, 2003.

[58] J. E. Heebner and R. W. Boyd, "'slow' and 'fast' light in resonator-coupled waveguides," *Journal of Modern Optics*, vol. 49, no. 14, 2002.

[59] K. N. Andersen, W. E. Svendsen, R. K. Sandberg, H. T. Philipp, and J. Hübner, "Silicon rich nitride micro-resonators," in *ECIO*, 2003.

[60] D. Zauner, K. Kulstad, J. Rathje, and M. Svalgaard, "Directly uv-written silica-on-silicon planar waveguides with low insertion loss," *Electron. Lett.*, vol. 34, no. 16, 1998.

[61] K. Hill, Y. Fujii, D. Johnson, and B. Kawasaki, "Photosensitivity in optical fiber waveguides: Application to reflection filter fabrication," *Applied Physics Letters*, vol. 32, pp. 647–649, 1978.

[62] E. Dianov, V. Mashinsky, V. Neustruev, O. Sazhin, V. Brazhkin, and V. Sidorov, "Optical absorption and luminescence of germanium oxygen-deficient centers in densified germanosilicate glass," *Optics Letters*, vol. 22, no. 14, 1997.

[63] D. Williams, S. Davey, R. Kashyap, J. Armitage, and B. Ainslie, "Direct observation of uv induced bleaching of 240 nm absorption band in photosensitive germanosilicate glass fibres," *Electronics Letters*, vol. 28, no. 4, 1992.

[64] D. Hand and P. Russell, "Photoinduced refractive-index changes in germanosilicate fibers," *Optics Letters*, vol. 15, no. 2, 1990.

[65] P. J. Lemaire, R. M. Atkins, V. Mizrahi, and W. A. Reed, "High pressure H_2 loading as a technique for acheiving ultrahigh uv photosensitivity and thermal sensisitivity in GeO_2 doped optical fibres," *Electron. Lett.*, vol. 29, no. 13, 1993.

[66] M. Svalgaard, *Ultraviolet light induced refractive index structures in germanosilica*. PhD thesis, Technical University of Denmark (MIC), 1997.

[67] Y. Hibino, T. Kominato, and Y. Ohmori, "Optical frequency tuning by laser-irradiation in silica-based march-zehnder-type multi/demultiplexers," *IEEE Photonics Technology Letters*, vol. 3, no. 7, 1991.

[68] D. Moss, J. Canning, M. Faith, P. Leech, P. Kemeny, C. Poulsen, and O. Leistiko, "Ultra-strong uv written gratings in pecvd grown ge doped silica waveguides with no hydrogen loading," *LEOS 96., IEEE*, vol. 2, pp. 34–35, 1996.

[69] D. Moss, M. Ibsen, F. Ouellette, P. Leech, M. Faith, P. Kemeny, O. Leistiko, and C. Poulsen, "Photo-induced planar germanosilicate

waveguides," in *Proceedings of the 19th Australian Conference on Optical Fibre (ACOFT '94)*, 1994.

[70] M. Svalgaard and M. Kristensen, "Directly uv written silica-on-silicon planar waveguides with low loss," *Electronics Letters*, vol. 33, no. 10, 1997.

[71] J. Hübner, C. Poulsen, J. Pedersen, M. Poulsen, T. Feuchter, and M. Kristensen, "*UV*-written y-splitter in *Ge*-doped silica," *SPIE*, vol. 2695, pp. 98–105, 1996.

[72] G. Maxwell and B. Ainslie, "Demonstration of a directly written directional coupler using uv-induced photosensitivity in a planar silica waveguide," *Electronics Letters*, 1995.

[73] K. Faerch and M. Svalgaard, "Symmetrical waveguide devices fabricated by direct uv writing," *IEEE Photonics Technology Letters*, vol. 14, no. 2, 2002.

[74] M. Svalgaard, K. Faerch, and L.-U. Andersen, "Variable optical attenuator fabricated by direct uv writing," *Journal of Lightwave Technology*, vol. 21, no. 9, 2003.

[75] A. Stump, J. Kunde, U. Gubler, A.-C. Pliska-LaDuff, and C. Bosshard, "A microring structure for practical devices." http://owtnm.fjfi.cvut.cz/files/Abstracts/39-Stump.pdf.

[76] R. Alferness, T. Koch, L. Buhl, F. Storz, F. Heismann, and M. Martyak, "Grating-assisted ingaasp/inp vertical codirectional coupler filter," *Applied Physics Letters*, vol. 55, no. 19, pp. 2011–13, 1989.

[77] H. Haeiwa, T. Naganawa, and Y. Kokubun, "Wide range center wavelength trimming of vertically coupled microring resonator filter by direct uv irradiation to sin ring core," *IEEE Photonics Technology Letters*, vol. 16, no. 1, pp. 135–137, 2004.

[78] J. Canning and S. Fleming, "Grating structures with phase mask period in silica-on-silicon planar waveguides," *Optics Communications*, vol. 171, no. 4-6, 1999.

[79] D. Wiesmann, J. Hübner, R. Germann, I. Massarek, H. Salemink, G. Bona, M. Kristensen, and H. Jackel, "Large uv-induced negative index changes in germanium-free nitrogen-doped planar sio/sub 2/ waveguides," *Electronics Letters*, vol. 34, no. 4, pp. 364–366, 1998.

[80] G. Meltz and W. Morey, "Bragg grating formation and germanosilicate fiber photosensitivity," *Proceedings of the SPIE*, vol. 1516, pp. 185–99, 1992.

[81] P. N. Butcher and D. Cotter, *The Elements of Nonlinear Optics*. Cambridge University Press, 1990.

[82] H. F. Kay, "Electrostriction," *Reports on Progress in Physics*, vol. 18, no. 1, pp. 230–250, 1955.

[83] M. R. Watts, G. Gorni, M. Cherchi, and H. A. Haus, "Polarization splitting and rotating through adiabatic transitions," *IPR 2004*, 2004.